

**A MODEL DEVELOPMENT AND COMPARISON STUDY
ON THE MICROWAVE REMOTE SENSING OF SNOW
MEDIUM USING A COUPLED FINITE ELEMENT
METHOD AND METHOD OF MOMENT, AND THE
RELAXED HIERARCHICAL EQUIVALENT SOURCE
ALGORITHM**

HAMSALEKHA A/P A KUMARESAN

MASTER OF ENGINEERING SCIENCE

**LEE KONG CHIAN FACULTY OF ENGINEERING AND
SCIENCE
UNIVERSITI TUNKU ABDUL RAHMAN
JULY 2022**

**A MODEL DEVELOPMENT AND COMPARISON STUDY ON THE
MICROWAVE REMOTE SENSING OF SNOW MEDIUM USING A
COUPLED FINITE ELEMENT METHOD AND METHOD OF
MOMENT, AND THE RELAXED HIERARCHICAL EQUIVALENT
SOURCE ALGORITHM**

By

HAMSALEKHA A/P A KUMARESAN

A dissertation submitted to the Department of Electrical and Electronics
Engineering,
Lee Kong Chian Faculty of Engineering and Science,
Universiti Tunku Abdul Rahman,
in partial fulfillment of the requirements for the degree of
Master of Engineering Science in July 2022

ABSTRACT

A MODEL DEVELOPMENT AND COMPARISON STUDY ON THE MICROWAVE REMOTE SENSING OF SNOW MEDIUM USING A COUPLED FINITE ELEMENT METHOD AND METHOD OF MOMENT, AND THE RELAXED HIERARCHICAL EQUIVALENT SOURCE ALGORITHM

Hamsalekha a/p A Kumaresan

Active microwave remote sensing is essential to analyze the condition of the earth's terrain by investigating the return of microwaves from the mentioned environment. The forward model is crucial to compute the backscattering return of the earth terrain under investigation, allowing comparison with the satellite data as it can be utilized in the inverse model to retrieve other earth terrain parameters. Radiative transfer equation is applied in the active remote sensing to calculate the backscattering coefficient for the theoretical model of the earth topographies such as vegetation, soil, snow medium and other earth terrains. Computational Electromagnetics Method (CEM) is vital to construct a more detailed shape of the scatterers and offer a better knowledge of the interaction between microwave radiation and the medium by considering the coherent effect of the dense snow medium. In this study, the second-order radiative transfer equation is incorporated with the theoretical model of the snow medium. The investigation is done by integrating two computational techniques, which are the coupled Finite Element Method (FEM) and Method of Moment (MoM) and the Relaxed Hierarchical Equivalent Source Algorithm (RHESA). These CEM generated electric and magnetic fields will be

incorporated with the Dense Medium Phase Amplitude Correction Theory (DM-PACT). These theoretical models consist of six shapes of scatterers which characterize the ice particles in the snow medium. These mentioned shapes are sphere, cylinder, peanut, hexagonal column, droxtal and ellipsoid. These techniques are used to study the effect of the various incident angles, layer thickness and frequencies of the backscattering mechanism. In previous investigations, little work has been carried out on the second-order radiative transfer equation on various shapes of ice scatterers by incorporating DM-PACT and Integral Equation Method (IEM) in snow medium. In this research, two different CEM techniques are incorporated into six different shapes of ice scatterers by incorporating DM-PACT and IEM, and the accuracy of the CEM techniques is studied. Through analysis, it is found that the discrepancy of the backscattering coefficient generated by coupled FEM/MoM with Mie theoretical result is higher than the discrepancy between RHESA and Mie theoretical result, especially at higher frequency and layer thickness of snow medium. The number of unknowns and the order of basis functions vary between these two CEM techniques, and these factors affect the accuracy of the results. The accuracy of the backscattering coefficient results generated by CEM techniques will be further justified by comparing them with the ground truth measurements. Through this research, a suitable CEM technique can be chosen for future investigation for other earth terrains such as soil, vegetation and different terrains.

ACKNOWLEDGEMENT

Thank you to everyone who has given their assistance and guidance in my study and completion of this dissertation. Prof Ewe Hong Tat and Dr Gobi Vetharatnam, my main and co-supervisors, for their direction, patience, support, and counsel during the research's progress, I would like to convey my heartfelt and genuine gratitude.

In addition, I'd want to convey my love and appreciation to my wonderful mother, Mrs P. Savithiri, for her unwavering moral support and encouragement in helping me throughout my Masters degree. I would not be here today if it weren't for her affection and supportive comments. I'd also want to thank my father, Mr A. Kumaresan, for his constant moral support and guidance during this project.

Furthermore, I appreciate my friends' help with this research. I do also want to apologise to everyone for any misunderstandings that may have occurred during this study.

Finally, my sincere gratitude to the Asian Office of Aerospace R&D (AOARD) for the funding of this research.

APPROVAL SHEET

This dissertation/thesis entitled “A MODEL DEVELOPMENT AND COMPARISON STUDY ON THE MICROWAVE REMOTE SENSING OF SNOW MEDIUM USING A COUPLED FINITE ELEMENT METHOD AND METHOD OF MOMENT, AND THE RELAXED HIERARCHICAL EQUIVALENT SOURCE ALGORITHM” was prepared by HAMSALEKHA A/P A KUMARESAN and submitted as partial fulfillment of the requirements for the degree of Master of Engineering Science at Universiti Tunku Abdul Rahman.

Approved by:



(Prof. Ir. Dr Ewe Hong Tat)

Date: ...4/7/2022.....

Supervisor

Department of Electrical and Electronics Engineering
Lee Kong Chian Faculty of Engineering and Science
Universiti Tunku Abdul Rahman



(Dr. Gobi Vetharatnam)

Date: ...4/7/2022.....

Co-supervisor

Department of Electrical and Electronics Engineering
Lee Kong Chian Faculty of Engineering and Science
Universiti Tunku Abdul Rahman

LEE KONG CHIAN FACULTY OF ENGINEERING AND SCIENCE

UNIVERSITI TUNKU ABDUL RAHMAN

Date: 4/7/2022

SUBMISSION OF DISSERTATION

It is hereby certified that **HAMSALEKHA A/P A KUMARESAN** (ID No: **19UEM05587**) has completed this dissertation entitled "**A MODEL DEVELOPMENT AND COMPARISON STUDY ON THE MICROWAVE REMOTE SENSING OF SNOW MEDIUM USING A COUPLED FINITE ELEMENT METHOD AND METHOD OF MOMENT, AND THE RELAXED HIERARCHICAL EQUIVALENT SOURCE ALGORITHM**" under the supervision of Prof. Ir. Dr. Ewe Hong Tat (Supervisor) from the Department of Electrical and Electronics Engineering, Lee Kong Chian Faculty of Engineering and Science , and Dr. Gobi Vetharatnam (Co-Supervisor) from the Department of Electrical and Electronics Engineering, Lee Kong Chian Faculty of Engineering and Science

I understand that University will upload softcopy of my final year project / dissertation/ thesis* in pdf format into UTAR Institutional Repository, which may be made accessible to UTAR community and public.

Yours truly,



(Hamsalekha a/p A Kumaresan)

DECLARATION

I (HAMSALEKHA A/P A KUMARESAN) hereby declare that the dissertation is based on my original work except for quotations and citations which have been duly acknowledged. I also declare that it has not been previously or concurrently submitted for any other degree at UTAR or other institutions.

Name: Hamsalekha a/p A Kumaresan

Date: July 2022

TABLE OF CONTENTS

	Page
ABSTRACT	ii
ACKNOWLEDGEMENTS	iv
APPROVAL SHEET	v
SUBMISSION OF DISSERTATION	vi
DECLARATION	vii
LIST OF TABLES	xi
LIST OF FIGURES	xii
LIST OF ABBREVIATIONS	xvi
CHAPTER	
1 INTRODUCTION	1
1.1 Background of the Research	1
1.2 Problem Statement	6
1.3 Objective of the Research	7
1.4 Outline of the Dissertation	8
2 LITERATURE REVIEW AND MODEL DEVELOPMENT SECOND-ORDER RT EQUATION USING CEM TECHNIQUES	10
2.1 RT Equation	10
2.2 Second-Order RT Equation for Snow Medium	12
2.2.1 Surface Scattering	19
2.2.2 Surface-Volume Scattering	21
2.2.3 Volume Scattering	22
2.3 Application of CEM Technique in RT Equation of Microwave Remote Sensing	24
2.4 Model Development on Second-Order RT Equation Using CEM Techniques	27
2.5 Summary	34
3 DEVELOPMENT OF RT MODEL WITH COUPLED FEM/MoM	36
3.1 FEM	36
3.2 MoM	39
3.3 Comparison between FEM and MoM	41
3.4 Coupled FEM/MoM	42
3.5 Formulation of Coupled FEM/MoM	45
3.6 Methodology of Coupled FEM/MoM in RT Equation	49

3.7	Summary	52
4	DEVELOPMENT OF RT MODEL WITH RHESA	53
4.1	Equivalent Principle Algorithm	54
4.1.1	Formulation of EPA	55
4.2	RHESA	57
4.2.1	Spherical Equivalence Surface	57
4.2.2	Formulation of RHESA	58
4.2.3	Methodology of RHESA in RT Equation	61
4.3	Summary	65
5	THEORETICAL ANALYSIS OF RT-COUPLED FEM/MOM AND RHESA	66
5.1	Introduction	66
5.2	Effect of Various Incident Angles on Backscattering Coefficient in FEKO and RHESA Simulation	67
5.3	Effect of Various Frequencies on Backscattering Coefficient in FEKO and RHESA Simulation	77
5.4	Effect of Various Layer Thickness on Backscattering Coefficient in FEKO and RHESA Simulation	78
5.5	Effect of Various Volume Fractions on Backscattering Coefficient in FEKO and RHESA simulation	81
5.6	Summary	83
6	COMPARISON OF CEM THEORETICAL MODEL WITH WITH GROUND TRUTH MEASUREMENT	85
6.1	Introduction	85
6.2	Comparison of CEM Techniques Generated Backscattering Coefficient of Snow Medium with CLPX Data at L-Band Frequency	85
6.3	Comparison of CEM Techniques Generated Backscattering Coefficient of Snow Medium with RADARSAT Data at C-Band Frequency	87
6.4	Comparison of CEM Techniques Generated Backscattering Coefficient of Snow Medium with CLPX Data at Ku-Band Frequency	89
6.5	Summary	94
7	CONCLUSION	96
7.1	Conclusion of the Research	96
7.2	Advantages and Limitations of the CEM Approaches	99
7.3	Future Improvement	103
8	REFERENCES	105
9	APPENDIX A	116
10	APPENDIX B	117

LIST OF TABLES

Table		Page
2.1	List of shapes of ice scatterers and the dimension of the geometries	30
3.1	The steps of FEM and MoM applied in the electromagnetic problem.	42
5.1	Theoretical model parameter for snow medium	67
7.1	Summary of the advantages and limitations of coupled FEM/MoM computation in FEKO software	102
9.2	Summary of the advantages and limitations of RHESA computation	103

LIST OF FIGURES

Figures		Page
2.1	Physical configuration of snow medium	12
2.2	Incident wave for the geometry of a single spherical scatterer	16
2.3	From left to right: Top and ground surface scattering	19
2.4	From left to right: Volume to surface 2 scattering and surface 2 to volume scattering	21
2.5	From left to right: (Up, down down), (up,up, down) and direct volume scattering	22
2.6	The flow chart of theoretical modelling of the snow ice scatterer	34
3.1	The nodal value and the interpolation function of the field variable	37
3.2	Various numerical approach applications based on the complexity and electrical size in FEKO software (Altair Engineering Inc, 2015).	44
3.3	Illustration of the system that consists of the dielectric region and open region	45
3.4	The configuration of the radiation and scattering mechanism (Silvester and Ferrari, 1996)	46
3.5	Example of the far field simulation for phase matrix of spherical scatterer from FEKO software.	50
3.6	Flow chart of RT-Coupled FEM/MoM of the theoretical model of snow medium	51

4.1	Huygens' principle: The tangential component of the field on the surface	54
4.2	The major three steps in equivalence principle operator: From left to right: Outside-in propagation, current solver and inside-out propagation	55
4.3	Demonstration of child and parent groups with spherical equivalence surfaces	58
4.4	The three steps of RHESA's far-field computation	59
4.6	Flow chart of RT-RHESA theoretical model of snow medium	64
5.1	Comparison of Mie theoretical result with FEKO and RHESA simulated results of six shapes of scatterers of snow medium at 0.1m layer thickness and 5.0 GHz frequency for (a, b) VV polarization, (c, d) HH polarization and (e, f) VH polarization for various incident angles.	69
5.2	Comparison of Mie theoretical result with FEKO and RHESA simulated results of six shapes of scatterers of snow medium at 0.5m layer thickness and 5.0 GHz frequency for (a, b) VV polarization, (c, d) HH polarization and (e, f) VH polarization for various incident angles.	70
5.3	Comparison of Mie theoretical result with FEKO and RHESA simulated results of six shapes of scatterers of snow medium at 0.1m layer thickness and 15.5 GHz frequency for (a, b) VV polarization, (c, d) HH polarization and (e, f) VH polarization for various incident angles.	73
5.4	Comparison of Mie theoretical result with FEKO and RHESA simulated results of six shapes of scatterers of snow medium at 0.5 m layer thickness and 15.5 GHz frequency for (a, b) VV polarization, (c, d) HH polarization and (e, f) VH polarization for various incident angles.	76
5.5	Comparison of Mie theoretical result with FEKO and RHESA simulated results of six shapes of scatterers of snow medium at 0.1 m layer thickness and 20-degree incident angle for (a, b) VV	78

	polarization, (c, d) HH polarization and (e, f) VH polarization for various frequencies.	
5.6	Comparison of Mie theoretical result with FEKO and RHESA simulated results of six shapes of scatterers of snow medium at 15.5GHz frequency and 20-degree incident angle for (a, b) VV polarization, (c, d) HH polarization and (e, f) VH polarization for various layer thickness of snow medium.	79
5.7	Comparison of Mie theoretical result with FEKO and RHESA simulated results of six shapes of scatterers of snow medium at 15.5GHz frequency and 20-degree incident angle for (a, b) VV polarization, (c, d) HH polarization and (e, f) VH polarization for various volume fraction of snow medium.	83
6.1	Comparison of VV backscattering coefficient of six shapes of ice scatterers produced by CEM methods (a) coupled FEM/MoM and (b) RHESA with CLPX data dated 21/2/2003 at L-Band frequency	87
6.2	Comparison of HH backscattering coefficient of six shapes of ice scatterers produced by CEM methods (a) coupled FEM/MoM and (b) RHESA with RADARSAT data at C-Band frequency	88
6.3	Comparison of VV backscattering coefficient of six shapes of ice scatterers produced by CEM methods (a) coupled FEM/MoM and (b) RHESA and HH backscattering coefficient (c) coupled FEM/MoM and (d) RHESA with CLPX data dated 21/2/2003 at Ku-Band frequency	92
6.4	Comparison of VV backscattering coefficient of six shapes of ice scatterers produced by CEM methods (a) coupled FEM/MoM and (b) RHESA and HH backscattering coefficient (c) coupled FEM/MoM and (d) RHESA with CLPX data dated 23/2/2003 at Ku-Band frequency	93
6.5	Comparison of VV backscattering coefficient of six shapes of ice scatterers produced by CEM methods (a) coupled FEM/MoM and (b) RHESA and HH backscattering coefficient (c) coupled FEM/MoM and (d) RHESA with CLPX data dated 24/2/2003 at Ku-Band frequency	94

LIST OF ABBREVIATIONS

BVP	Boundary Value Problem
CEM	Computational Electromagnetic
CG-FFT	Conjugate Gradient- Fast Fourier Transform
CLPX	Cold Land Processes Field Experiment
DDA	Discrete Dipole Approximation
DDM	Domain Decomposition Method
DE	Differential Equation
DISORT	Discrete Ordinates Radiative Transfer
DMPACT	Dense Medium Phase and Amplitude Correction Theory
DMRT	Dense Medium Radiative Transfer
EFIE	Electric Field Integral Equation
EM	Electromagnetic
EPA	Equivalent Principle Algorithm
ES	Equivalent Surface
FDTD	Finite Difference Time Domain
FEM	Finite Element Method
FM	Fast Multipole Algorithm
GMM	Generalized Multiparticle Mie
IE	Integral Equation
IEM	Integral Equation Method
IOP	Intensive Observation Periods
KM	Kirchhoff Model

LSOS	Local Scale Observation Site
MFIE	Magnetic Field Integral Equation
MLDMA	Multilevel Matrix Decomposition Algorithm
MLFMA	Multilevel Fast Multipole Algorithm
MoM	Method of Moment
PDE	Partial Differential Equation
QCA	Quasi-Crystalline Approximation
QCA-CP	Quasi-Crystalline Approximation-Coherent Potential
RHESA	Relaxed Hierarchical Equivalent Source Algorithm
RMS	Root Mean Square
RT	Radiative Transfer
SPM	Small Perturbation Model
SWE	Snow Water Equivalent
VIE	Volume Integral Equation

CHAPTER 1

INTRODUCTION

1.1 Background of the Research

Microwave radiometry and radiative transfer are associated with each other to study the propagation of the wave in both homogeneous and inhomogeneous mediums. Each type of media has a different mechanism of wave propagation where the mechanism refers to emission, reflection, scattering and the list goes on (Mätzler, 2006) and this theory is widely implemented in remote sensing, astrophysics, climate modelling and other fields as well (Lessig and L.Castro, 2013).

Microwave remote sensing has a great advantage in the field of remote sensing research. It has the capability to penetrate clouds, moistures, dry soils, and sand. There are two types of microwave remote sensing which are active and passive remote sensing. In active remote sensing, the radiation is provided by the active imagers. In passive remote sensing, the thermal emission is observed through the radiation of the natural light wave such as sunlight, infrared rays and other rays. (Woodhouse, 2017).

In the recent development of microwave remote sensing, CEM plays a crucial role, especially in the theoretical modelling of the scatterers. In electromagnetics, Maxwell's equation is the essential equation to solve many problems in remote sensors, optics and the list goes on. However, analytical Maxwell's equation is only capable to solve simpler cases such as plane waves that are scattered from a sphere. As the geometrical structure of the scatterers become complicated, the equations become complex, and they require numerical approaches to compute the current and EM fields.

To compute the current and EM fields of the scatterers from a specific earth terrain, a suitable scattering mechanism need to be identified. There are various scattering mechanisms in the wave propagation such as Rayleigh, Raman, and Mie scattering. Rayleigh scattering is also known as elastic scattering by the air molecules. In Rayleigh scattering, the size of the scatterers is smaller than the wavelength of the radiation, thus the scatterers will receive a uniform distribution of electromagnetic field (Piazza and Degiorgio, 2005). Unfortunately, the application of Rayleigh scattering theory does not take into account the coherent effect of the wave interaction among the scatterers. (Tsang et al., 2007).

Mie scattering is an interaction of light with the scatterers where their dimension is comparable to the wavelength of the incident wave. This method has a greater advantage compared to the Rayleigh scattering as the coherent effect of the wave scattering is considered (Platt, Pfeilsticker and Vollmer, 2007). Therefore, the Mie scattering approach is much more effective to be

used for the radiative transfer computation for dense mediums such as snow and sea ice medium.

In the Mie computation, various scattering mechanisms need to be considered for the snow and sea ice medium. Examples of scattering mechanisms are surface scattering, volume scattering and both surface-volume scattering. To compute the coherent effect of the scattered wave involving these mechanisms, various approximations and corrections were involved in the radiative transfer equation to calculate the coherent effect of the scatterers in the dense medium. For example, QCA focuses on field theory, and it computes the effect of coherent scattering with the position of the scatterers (West, Gibbs, Tsang and Fung, 1994).

There is another concept that considers the near field effect of the scatterers which is known as the DM-PACT where the amplitude and phase correction factors are multiplied with the Stokes matrix to compute the radiative transfer equation (Ewe and Chuah, 1998). The incorporation of such corrections was earlier done for Mie phase matrix computation for spherical scatterers in the dense snow and sea ice medium. However, various shapes are being developed for the snow scatterers as the Mie phase matrix computation is for spherical scatterers and cannot be merely implemented to represent scatterers of various shapes in the computation of the backscattering coefficient. Therefore, a suitable CEM technique is needed to incorporate the Stokes matrix of various shapes of scatterers with DM-

PACT to take into account the effect of the scattering of the adjacent scatterers (Lum, Fu, Ewe and Jiang, 2017).

Multiple types of CEM techniques were used to compute the radiative transfer equation for various shapes of scatterers. The CEM technique mainly consists of two different types of numerical computations which are integral equations (IE) and partial differential equation (PDE) (Chew et al., 1997). For example, through Method of Moment (MoM), the integral equation is discretized whereas the Finite Difference Time Domain (FDTD) and Finite Element Method (FEM) are used to discretize the differential equation. Each numerical approach has its own advantages and drawbacks, hence lots of research work were done to improvise the numerical approach by combining more than one numerical method in CEM to increase the computational speed and decrease memory requirement.

For example, MoM is known as a unifying principle for a basic mathematical technique to reduce functional equations to matrix equations (Harrington, 2000). The Multilevel Matrix Decomposition Algorithm (MLMDA) disintegrates the MoM matrix into numerous blocks which describe the interaction between distant scatterers. (Song, Cai-Cheng Lu and Weng Cho Chew, 1997). MoM and MLMDA are CEM methods where it can be used to develop and solve Maxwell's equation and Laplace's equations. Due to the slow speed of MoM computation for large and complex problems, MLMDA and Multilevel Fast Multipole Algorithm (MLFMA) are used to

increase the speed of dense matrix equation calculation. It is because MLFMA decreases the complexity of the problem and memory requirement.

FEM is a numerical approach to compute boundary value problems (BVP) as it divides the domain into smaller subdomains which are known as finite elements (Polycarpou, 2006). FEM approach is suitable for dielectric scatterers and is also used for simple geometrical structures of scatterers. However, FEM involves higher computational time to compute complex boundaries as it requires time-domain computation (Rylander, Ingelström and Bondeson, 2013). FEM approach for a 3-dimension structure confronts vector parasites where it may result in incorrect solutions (Sumithra and Thiripurasundari, 2017).

Therefore, suitable CEM techniques which hybridize more than one numerical approach are needed to incorporate with the radiative transfer equations to increase the accuracy of the results and thus can be applied for various electromagnetic problems for numerous earth terrain. An appropriate hybridized numerical solution not only increases the precision of the result but can also reduce the memory requirement and increase the computational capacity. Furthermore, this approach has the tendency on handling more complex geometries.

1.2 Problem Statement

Research on snow medium is crucial to study the impact of global warming on snowfall. For example, in Japan, snow cover is the main water reserve despite the massive snowfall which could lead to disaster. Unfortunately, due to the increase in the air temperature, the depth of the snow medium decreases drastically (Hara, Yoshikane, Kawase and Kimura, 2008). Thus, lots of information are required to carry the investigation on various aspect of snow medium to uncover the problem that we are facing today which is global warming. However, due to the low number of remote sensing results, there are some constraints to conduct the ecological studies on snow data (Niittynen and Luoto, 2017). Therefore, computational electromagnetics application on remote sensing is essential to create a forward model of radiative transfer equation to obtain the results of backscattering coefficient for snow and sea ice medium. These mentioned results are important to retrieve various snow parameters such as snow permittivity, snow water equivalent (SWE) and the list goes on. For example, SWE is important to determine the effect of the environmental temperature and moisture on the snow accumulation. (Durand, Molotch and Margulis, 2008). It is because as the environmental temperature increases, the atmospheric moisture decreases, thus causes reduction in snowfall. (Hara, Yoshikane, Kawase and Kimura, 2008)

However, a suitable theoretical model for snow medium is needed to study the interactions of the electromagnetic wave with the scatterer to obtain the accurate result of the backscattering coefficient. Two major aspects of the

theoretical model are considered in this research to create a good theoretical model for better accuracy of the backscattering coefficient data. The first aspect is the geometrical representation of the ice scatterer of snow medium. Conventionally, the scatterers of snow medium are assumed to be spherical. However, due to the development of remote sensing and computational electromagnetic research, different ice scatterers' shapes are being explored in snow medium.

The second aspect of the research is the type of computational electromagnetic technique that is being used to justify the accuracy of the data. In this research, two types of hybridized CEM method are applied to validate the precision of the backscattering coefficient result of snow medium. The two CEM techniques are coupled FEM/MoM and RHESA. The backscattering coefficient results of these two CEM techniques will be compared and analysed as each CEM technique has a different way of numerical approach and they may affect the accuracy of the result.

1.3 Objective of the research

The objectives of the research are:

- i. To investigate and configure suitable geometrical representation of the ice scatterers of snow medium.

- ii. To develop a theoretical model based on RT theory with the coupled FEM and MoM techniques for both spherical and non-spherical shaped ice scatterers of snow medium.
- iii. To adapt RHESA in the developed RT theoretical model for improved physical model configuration and scattering analysis.
- iv. To validate the improved Radiative Transfer (RT) model by comparing backscattering coefficient results with the ground truth data of the satellite data.

1.4 Outline of the Dissertation

Chapter Two of the dissertation consists of a literature review and model development on second-order RT equation using CEM techniques. This literature review covers the concept of radiative transfer and its equations which consist of zeroth, first and second-order scattering. The model development is presented for both spherical and non-spherical-shaped scatterers. The formula of the geometrical representation of non-spherical shapes of ice scatterers is included in this chapter. Besides, some of the numerical approaches of CEM are explained in this chapter.

In the third chapter of the dissertation, the formulation of the coupled FEM/MoM in the RT equation is focused on where concepts and equations of FEM and MoM are explained separately. Then, the advantages of coupled FEM/MoM are elaborated. Finally, the application of the coupled FEM/MoM in RT equations is described in this chapter. In the fourth chapter of the

dissertation, the formulation of RHESA in the RT equation will be explained. This chapter covers the EPA and DDM and further focuses on RHESA.

In the fifth chapter, the backscattering coefficient of snow medium with various parameters is generated using two CEM techniques. These results are compared with each other and further compared with Mie theoretical results to study the accuracy of the CEM techniques and the suitability of shapes of the scatterers for snow medium.

In Chapter Six, the comparison of the theoretical data with the ground truth measurement is presented to validate the accuracy of the theoretical results for different shapes of ice scatterers of snow medium. Finally, the research is concluded in Chapter Seven. Additionally, the limitations that were encountered in this research are described in the dissertation, along with some suggestions for the development of the study.

CHAPTER 2

LITERATURE REVIEW AND MODEL DEVELOPMENT ON SECOND-ORDER RT EQUATION USING CEM TECHNIQUES

2.1 RT Equation

According to Subrahmanyam Chandrasekhar, the radiative transfer (RT) equation represents various radiation processes in a medium such as absorption, emission and as well as scattering process (Chandrasekhar, 1989). RT equation was applied in the study of the effect of the multiple scattering through a foggy atmosphere. Schuster defined the atmosphere as “foggy” as the molecules of a homogeneous material can scatter and spread to all bodies (Marzano, 2014; Schuster, 1905). Tsang explained that the wave propagation is different for a random and deterministic medium where the phase and amplitude need to be computed in respect of probability densities and statistical averages for the random medium (Ishimaru, 2005). Through the knowledge of the RT equation, it can be applied to various fields especially in active remote sensing for numerous earth terrain. A forward theoretical model is developed for countless earth terrain and the RT equation is used to compute the backscattering coefficient of the topography. The results of the backscattering coefficient of snow medium can be used to retrieve some

important parameters such as depth of the snow, density, SWE and other information (Zhu et al., 2018).

A conventional RT theory was applied to compute the backscattering return for earth terrain by assuming that the scatterers are independent of each other. Shin et al. studied the scattering of spherical scatterers that are embedded in a homogeneous medium and layered by the homogeneous half-space by implementing the Rayleigh scattering model in the second-order RT equation. The backscattering cross-sections per unit area were computed by using both numerical and iterative methods.

A radiative wave equation was used to compute the backscattering return from the dense medium as the assumption of sparse medium is not applicable. Thus, the radiative wave equation was computed based on the QCA by incorporating it with coherent potential (CP) (Tsang and Ishimaru, 1987). The reason QCA-CP is implemented in the radiative wave theory is that the energy is conserved better than in the conventional radiative transfer equation. Thus, the former can also be called dense medium radiative transfer (DMRT). There are several advantages of DMRT over the conventional sparse radiative transfer equation. The scattering by neighbouring particles is considered and the intensities of the multiple scattering are taken into account. Furthermore, the energy has conserved in this mentioned DMRT equation (Wen, Tsang, Winebrenner and Ishimaru, 1990).

To improve the accuracy of the result, a phase matrix that comprises both phase and amplitude corrections were used to compute the scattering

coefficient of the scatterers embedded in the electrically dense medium. The phase correction is based on the antenna array concept where the total electric field of the electrically dense medium is equal to the sum of the scattered electric field of the scatterers with the incorporation of the array phase correction factor (Fung, Tsuatja, Bredow and Chuah, 1995). The phase correction factor was further developed for non-spherical scatterers such as ellipsoid and disk-shaped scatterers to calculate the backscattering coefficient of the vegetation medium. In this case, three types of corrections were considered to increase the accuracy of the result which are the amplitude, array phase and Fresnel correction (Ewe and Chuah, 2000).

2.2 Second-Order RT Equation for Snow Medium

The incorporation of mentioned corrections was done for Mie phase matrix computation for spherical scatterers in the dense snow and sea ice medium.

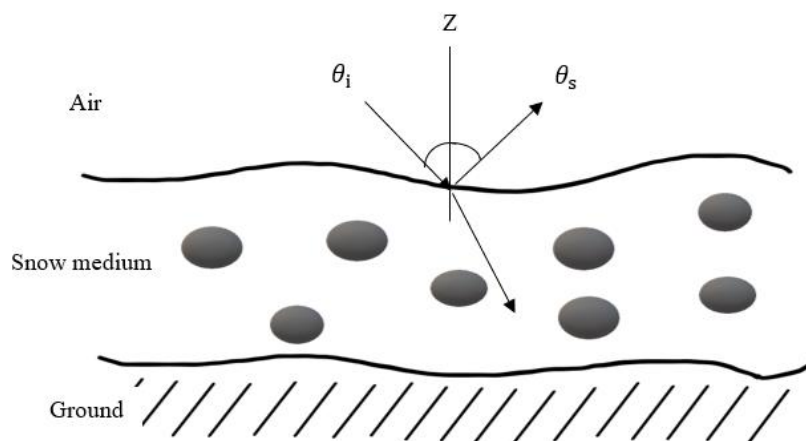


Figure 2.1 Physical configuration of snow medium

θ_i and θ_s represent the incident and scattered angles respectively. Z represents the vertical axis of the medium.

The second-order radiative transfer equation is written as in equation 2.1.

$$\cos \theta \frac{d\bar{I}}{dz} = -\bar{\kappa}_e \bar{I} + \int \bar{P}\bar{I} d\Omega \quad (2.1)$$

where \bar{I} is the Stokes matrix that represents the intensity of the wave, \bar{P} and $\bar{\kappa}_e$ represents the phase and extinction matrix correspondingly (Ewe and Chuah, 2000).

The phase matrix, \bar{P} can be described as shown in equation 2.2.

$$\bar{P}(\theta, \varnothing; \theta', \varnothing) = \langle |\Psi|^2 \rangle_n \cdot \bar{S} = \begin{bmatrix} P_{vv} & P_{vh} \\ P_{hv} & P_{hh} \end{bmatrix} \quad (2.2)$$

$\langle |\Psi|^2 \rangle_n$ is an effective number density for the dense medium and \bar{S} is the Stokes matrix of a single scatterer. P_{pq} represents the phase matrix and the subscripts v and h denote vertical and horizontal polarizations. The phase matrix, \bar{P} links the Stokes parameters of incident and scattered rays in the random medium. The Stokes matrix, \bar{S} can be expressed as (Chuah, Tjuatja, Fung and Bredow, 1996). θ and \varnothing are the polar and azimuth angles which are based on Gaussian quadrature points.

$$\bar{S} = \frac{d^2\eta}{|E_o|^2} \text{Re} \begin{bmatrix} (E_v^S H_h^{S*})_{v-inc} & (E_v^S H_h^{S*})_{h-inc} \\ -(E_h^S H_v^{S*})_{v-inc} & -(E_h^S H_v^{S*})_{h-inc} \end{bmatrix} \quad (2.3)$$

where d is an expression for the average distance between the scatterers which can also be written as

$$d = \left(\frac{v_o}{v_f} \right)^{\frac{1}{3}} \quad (2.4)$$

v_o and v_f are the volume of the scatterer and the volume fraction of the scatterers per unit volume respectively. The Stokes parameters of an elliptically polarized plane wave, $\bar{E} = (E_v \hat{v} + E_h \hat{h})e^{-j\bar{k}\bar{r}}$ can be expressed as four components of the Stokes vector.

$$\begin{aligned} I_v d\Omega &= \frac{\langle |E_v|^2 \rangle}{\eta} \\ I_h d\Omega &= \frac{\langle |E_h|^2 \rangle}{\eta} \\ U d\Omega &= \frac{2}{\eta} \text{Re}\langle E_v E_h^* \rangle \\ V d\Omega &= \frac{2}{\eta} \text{Im}\langle E_v E_h^* \rangle \end{aligned} \quad (2.5)$$

where I_v and I_h are specific intensity of vertical and horizontal polarization, U and V are the relationships between the two polarizations respectively. $d\Omega$ and η are the differential solid angle where the wave travels through and intrinsic impedance of the medium respectively.

From equation 2.1, the extinction coefficient, \bar{K}_e can be described as the addition of the scattering coefficient, \bar{K}_s and absorption coefficient, \bar{K}_a . Thus, the mentioned formula can be described as the volume extinction coefficient which is written as shown in Equation 2.6.

$$\bar{K}_e = \bar{K}_s + \bar{K}_a \quad (2.6)$$

The absorption coefficient, \bar{K}_a for p polarization, is also described as the absorption loss in an inhomogeneous medium where it can be described as in Equation 2.7 (Fung, 1994).

$$\bar{K}_{ap} = 2k_o |Im\sqrt{\varepsilon_{ap}}| \quad (2.7)$$

where ε_{ap} and k_o are average relative permittivity of the medium and free-space wavenumber respectively.

The scattering coefficient, \bar{K}_s is the multiplication of the total scattered power of the scatterer with the number of the scatterers per unit volume, n_o .

$$\bar{K}_{sp}(\theta_i, \phi_i) = n_o \int_0^{2\pi} \int_0^\pi (S_{vp} + S_{hp}) \sin \theta_s d\theta_s d\phi_s \quad (2.8)$$

Where p and S are the polarization and the component of the Stokes matrix respectively. For spherical scatterers, the scattered EM fields are computed analytically using the Mie scattering formulation. Consider a sphere with relative permittivity $\varepsilon_r = \varepsilon' - j\varepsilon''$ where the incidence wave travelling in $+\hat{z}$ direction toward the sphere with radius a . The permeabilities of the sphere and background medium are set to μ .

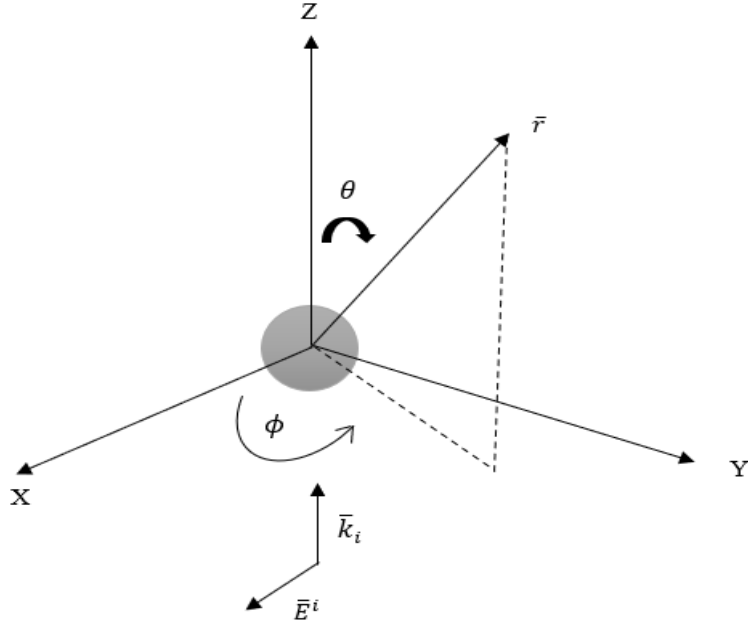


Figure 2.2 Incident wave for the geometry of a single spherical scatterer

As shown in Figure 2.2 the electric and magnetic fields are given by

$$\bar{E}^i = \hat{x}E_o e^{-jkz} \quad (2.9)$$

$$\bar{H}^i = \hat{y} \frac{E_o}{\eta} e^{-jkz} \quad (2.10)$$

where $k = \omega\sqrt{\mu\varepsilon}$ and $\eta = \sqrt{\mu/\varepsilon}$. The time dependence term, $e^{j\omega t}$ was used for the electric and magnetic field equations.

The electric and magnetic fields from the sphere are described in Equations 2.11 and 2.12. (Hulst, 1981)

$$\bar{E}^s = E_o \sum_{n=1}^{\infty} (-j)^n \frac{(2n+1)}{n(n+1)} \left\{ -b_n \bar{m}_{oln}^{(3)} - ja_n \bar{n}_{eln}^{(3)} \right\} \quad (2.11)$$

$$\bar{H}^s = \frac{E_o}{\eta} \sum_{n=1}^{\infty} (-j)^n \frac{(2n+1)}{n(n+1)} \left\{ a_n \bar{m}_{eln}^{(3)} - jb_n \bar{n}_{oln}^{(3)} \right\} \quad (2.12)$$

where a_n and b_n are the Mie coefficient that corresponds to the amplitudes that are produced by oscillations due to the excitation of the incident wave in the sphere (Fung, 1994; Hulst, 1981).

$$a_n = \frac{\sqrt{\varepsilon_r} \hat{J}'_n(u) \hat{J}_n(v) - \hat{J}_n(u) \hat{J}'_n(v)}{\sqrt{\varepsilon_r} [\hat{H}_n^{(2)}(u)]' \hat{J}_n(v) - \hat{H}_n^{(2)}(u) \hat{J}'_n(v)} \quad (2.13)$$

$$b_n = \frac{\sqrt{\varepsilon_r} \hat{J}_n(u) \hat{J}'_n(v) - \hat{J}_n(u) \hat{J}_n(v)}{\sqrt{\varepsilon_r} [\hat{H}_n^{(2)}(u)] \hat{J}'_n(v) - [\hat{H}_n^{(2)}(u)] \hat{J}_n(v)} \quad (2.14)$$

Where $u = ka$, $v = k\sqrt{\varepsilon_r}a = k_s a$. $J_n(\varphi)$ and $\hat{H}_n^{(2)}(\varphi)$ are the Ricatti-Bessel function and Ricatti-Hankel function of the second kind respectively. Prime symbol represents the differentiation to the argument. The o and e of the spherical vector wave function $\bar{m}_{eln}^{(3)}$ and $\bar{n}_{oln}^{(3)}$ represent the even and odd and can be stated as the Hankel function of sphere of the second kind $h_n^{(2)}(kr)$ and Legendre polynomials $P_n^l(\cos \theta)$. This is further expressed as (Fung, 1994):

$$\bar{m}_{o\ e ln}^{(3)} = \pm \hat{\theta} \frac{1}{\sin \theta} h_n^{(2)}(kr) P_n^l(\cos \theta)_{\sin \phi}^{\cos \phi} - \hat{\phi} h_n^{(2)}(kr) \frac{\partial}{\partial \theta} \{P_n^l(\cos \theta)\}_{\cos \phi}^{\sin \phi} \quad (2.15)$$

$$\begin{aligned} \bar{n}_{o\ e ln}^{(3)} &= \hat{r} \frac{n(n+1)}{kr} h_n^{(2)}(kr) P_n^l(\cos \theta) \sin \phi \\ &\hat{\theta} \frac{1}{kr} \frac{dy}{d(kr)} \{kr h_n^{(2)}(kr)\} \frac{\partial}{\partial \theta} \{P_n^l(\cos \theta)\}_{\cos \phi}^{\sin \phi} \\ &\hat{\phi} \frac{1}{kr \sin \theta} \frac{d}{d(kr)} \{kr h_n^{(2)}(kr)\} P_n^l(\cos \theta)_{\sin \phi}^{\cos \phi} \end{aligned} \quad (2.16)$$

Where r is the range of the scattered fields are determined.

The detailed transformation of the coordinate system of the scattered field components can be found in (Fung and Eom, 1985) and (Fung, 1994).

The integrodifferential of Equation 2.1 is derived iteratively up to second order, where various sources of scattering are obtained. The bistatic scattering which correlates the scattering intensities to the incident intensities is shown in Equation 2.17.

$$\sigma_{pq}(\theta_s, \phi_s, \theta_i, \phi_i) = \sigma_{pq}(0) + \sigma_{pq}(1) + \sigma_{pq}(2) \quad (2.17)$$

Where p and q represent the scattered and incident field polarizations respectively. As shown in Equation 2.17, the right-hand side bistatic scattering are arranged according to zeroth, first and second-order solutions where they are labelled by the number in the bracket. (θ_i, ϕ_i) and (θ_s, ϕ_s) represent the incident and scattered directions respectively.

The contribution of each term is given as (Fung, 1994):

$$\sigma_{pq}(0) = \sigma_{pq}^s = \sigma_{pq}^{s1} + \sigma_{pq}^{s2} \quad (2.18)$$

$$\sigma_{pq}(1) = \sigma_{pq}^{vs}(m \rightarrow s2) + \sigma_{pq}^{vs}(s2 \rightarrow m) + \sigma_{pq}^v(up, down) \quad (2.19)$$

$$\sigma_{pq}(2) = \sigma_{pq}^v(up, up, down) + \sigma_{pq}^v(up, down, down) \quad (2.20)$$

Equation 2.18 represents the surface scattering terms, where s , $s1$ and $s2$ represent the total scattering term, scattering from top surfaces and bottom surfaces respectively. Equation 2.19 is the 1st order scattering term where vs and v represent the volume-surface and volume scattering terms respectively.

($m \rightarrow s2$) implies the volume to bottom surface scattering term whereas surface to bottom scattering term. ($up, down$) represents the single volume scattering terms. Equation 2.20 represents the double volume scattering terms where ($up, up, down$) and ($up, down, down$) represent the scattering direction of the incident wave.

2.2.1 Surface Scattering

As explained in Equation 2.18, there are two contributions of scattering which represent the top and bottom surfaces.

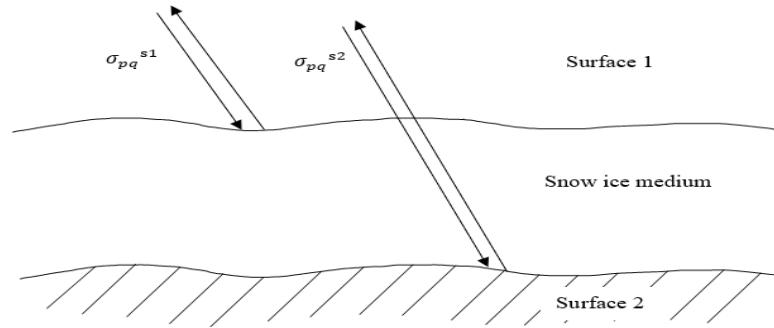


Figure 2.3 From left to right: Top and ground surface scattering

Bistatic single-scattering coefficient for top and ground surfaces which are the zeroth-order solution is given as:

$$\sigma_{pq}^{s1}(\theta_s, \phi_s, \theta_i, \phi_i) = \sigma_{pq}^{o1}(\theta_s, \phi_s, \theta_i, \phi_i) \quad (2.21)$$

$$\sigma_{pq}^{s2}(\theta_s, \phi_s, \theta_i, \phi_i) = \cos \theta_s T_{1tp}(\theta_s, \theta_{ts}) T_{t1q}(\theta_{ti}, \theta_i) \sec \theta_{ts} L_p(\theta_{ts}) L_q(\theta_{ti}) \sigma_{pq}^{o2}(\theta_{ts}, \phi_{ts}, \theta_{ti}, \phi_{ti}) \quad (2.22)$$

Where σ_{pq}^{o1} and σ_{pq}^{o2} are the top and bottom surfaces' bistatic scattering coefficient, which is based on the integral equation method (IEM) rough surface model (Ewe, Chuah and Fung, 1998). For a randomly rough surface model, many surface parameters such as root mean square (RMS) surface slope, wave spectrum and other parameters need to be considered to compute the boundary scattering. The advantage of IEM over the Kirchhoff model (KM) and Small Perturbation Model (SPM) is that IEM can be used for the wavelength irrespective of any surface geometric scale (Liu, Li and Weng, 1999). In contrast, SPM restricts the wavelength of the incident wave to be way much longer than the RMS height whereas the KM requires the incident wavelength to be shorter than the surface curvature radius (Liu and Li, 2002).

θ_s and θ_i are the scattered and incident polar angle in the air. θ_{ts} and θ_{ti} are scattered and incident polar angles in the random layer through Snell's law. The T and L terms are labelled as the transmissivity and attenuation through the layer respectively. The attenuation through the random layer can be further elaborated as shown in Equation 2.23.

$$L_u(\theta) = \exp[-K_{eu}(\theta)d_l \sec \theta] \quad (2.23)$$

where K_{eu} and d_l are the volume extinction coefficient and layer thickness respectively.

2.2.2 Surface-Volume Scattering

Figure 2.4 illustrates the surface-volume scattering which comprises of the scattering from volume to the ground surface (Surface 2) and the scattering from the bottom surface (Surface 2) towards the volume.

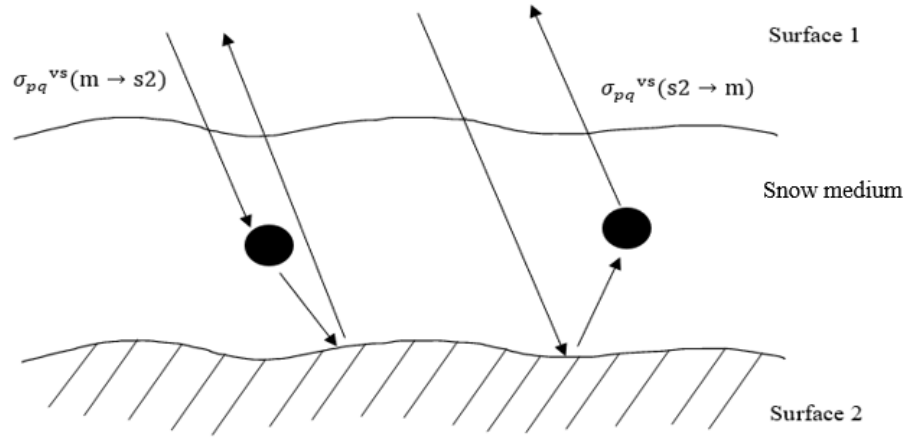


Figure 2.4 From left to right: Volume to surface 2 scattering and surface 2 to volume scattering

The surface-volume scattering equations which consist first-order solution are further derived as shown in Equation 2.24 and 2.25:

$$\begin{aligned}
 & \sigma_{pq}^{vs}(m \rightarrow s2) = \\
 & \cos \theta_s T_{1tp}(\theta_s, \theta_{ts}) T_{t1q}(\theta_{ti}, \theta_i) L_p(\theta_{ts}) \sec \theta_{ts} \\
 & \int_0^{2\pi} d\phi \int_0^{\frac{\pi}{2}} \sin \theta \sec \theta d\theta \\
 & \sum_{u=v,h} \sigma_{pu}^{s2}(\theta_{ts}, \phi_{ts}; \pi - \theta, \phi) P_{uq}(\pi - \theta, \phi; \pi - \theta_{ti}, \phi_{ti}) \\
 & \frac{L_u(\theta) - L_q(\theta_{ti})}{K_{eq}(\theta_{ti}) \sec \theta_{ti} - K_{eu}(\theta) \sec \theta}
 \end{aligned} \tag{2.24}$$

$$\begin{aligned}
& \sigma_{pq}^{vs}(s2 \rightarrow m) = \\
& \cos \theta_s T_{Itp}(\theta_s, \theta_{ts}) T_{tlq}(\theta_{ti}, \theta_i) L_q(\theta_{ti}) \sec \theta_{ts} \\
& \int_0^{2\pi} d\phi \int_0^{\frac{\pi}{2}} \sin \theta \sec \theta d\theta \\
& \sum_{u=v,h} P_{pu}(\theta_{ts}, \phi_{ts}; \theta, \phi) \sigma_{uq}^{s2}(\theta, \phi; \pi - \theta_{ti}, \phi_{ti}) \\
& \frac{L_p(\theta_{ts}) - L_u(\theta)}{K_{eu}(\theta) \sec \theta - K_{ep}(\theta_{ts}) \sec \theta_{ts}}
\end{aligned} \tag{2.25}$$

P_{uq} and σ_{pu}^{s2} are the phase matrix of the ice scatterers of the snow medium and the scattering from the bottom surface respectively.

2.2.3 Volume Scattering

As shown in Figure 2.5, there are two order solutions in this volume scattering mechanism. The *up, down, down*, and *up, up, down* scattering are classified as second-order solutions whereas the direct volume scattering is classified as first-order solutions.

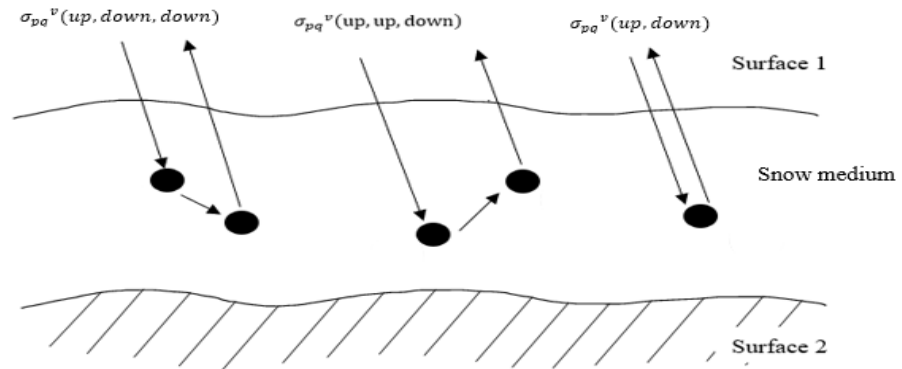


Figure 2.5 From left to right: (Up, down down), (up, up, down) and direct volume scattering

The volume scattering mechanism is further derived as shown in Equation 2.26 up to 2.28.

$$\begin{aligned} \sigma_{pq}^v(up, down) = & \\ & 4\pi \cos \theta_s T_{ltp}(\theta_s, \theta_{ts}) T_{t1q}(\theta_{ti}, \theta_i) \sec \theta_{ts} \\ & \frac{P_{pq}(\theta_{ts}, \phi_{ts}; \pi - \theta_{ti}, \phi_{ti})}{1 - L_p(\theta_{ts}) L_q(\theta_{ti})} \\ & \frac{1}{K_{ep}(\theta_{ts}) \sec \theta_{ts} + K_{eq}(\theta_{ti}) \sec \theta_{ti}} \end{aligned} \quad (2.26)$$

$$\begin{aligned} \sigma_{pq}^v(up, up, down) = & \\ & 4\pi \cos \theta_s T_{ltp}(\theta_s, \theta_{ts}) T_{tlq}(\theta_{ti}, \theta_i) \sec \theta_{ts} \\ & \int_0^{2\pi} d\phi \int_0^{\frac{\pi}{2}} \sin \theta \sec \theta d\theta \\ & \sum_{u=v,h} \left\{ \frac{P_{pu}(\theta_{ts}, \phi_{ts}; \theta, \phi) P_{uq}(\theta, \phi; \pi - \theta_{ti}, \phi_{ti})}{K_{eq}(\theta_{ti}) \sec \theta_{ti} + K_{eu}(\theta) \sec \theta} \right\} \\ & \left[\frac{1 - L_p(\theta_{ts}) L_q(\theta_{ti})}{K_{ep}(\theta_{ts}) \sec \theta_{ts} + K_{eq}(\theta_{ti}) \sec \theta_{ti}} + \frac{L_q(\theta_{ti}) [L_u(\theta) - L_p(\theta_{ts})]}{K_{eu}(\theta) \sec \theta - K_{ep}(\theta_{ts}) \sec \theta_{ts}} \right] \end{aligned} \quad (2.27)$$

$$\begin{aligned} \sigma_{pq}^v(up, down, down) = & \\ & 4\pi \cos \theta_s T_{ltp}(\theta_s, \theta_{ts}) T_{t1q}(\theta_{ti}, \theta_i) \sec \theta_{ts} \\ & \int_0^{2\pi} d\phi \int_0^{\frac{\pi}{2}} \sin \theta \sec \theta d\theta \\ & \sum_{u=v,h} \left\{ \frac{P_{pu}(\theta_{ts}, \phi_{ts}; \pi - \theta, \phi) P_{uq}(\pi - \theta, \phi; \pi - \theta_{ti}, \phi_{ti})}{K_{ep}(\theta_{ts}) \sec \theta_{ts} + K_{eu}(\theta) \sec \theta} \right\} \\ & \left[\frac{1 - L_p(\theta_{ts}) L_q(\theta_{ti})}{K_{ep}(\theta_{ts}) \sec \theta_{ts} + K_{eq}(\theta_{ti}) \sec \theta_{ti}} + \frac{L_p(\theta_{ts}) [L_u(\theta) - L_q(\theta_{ti})]}{K_{eu}(\theta) \sec \theta - K_{eq}(\theta_{ti}) \sec \theta_{ti}} \right] \end{aligned} \quad (2.28)$$

The *(up, down, down)* mechanism is where the incident wave is scattered towards the first scatterer and the transmitted wave of the first scatterer will be scattered downward to the second scatterer before being scattered to the Surface 1. Whereas, the *(up, up, down)* mechanism is where the incident wave is scattered towards the first scatterer and the transmitted wave of the first scatterer will be scattered upward to the second scatterer before being scattered to the Surface 1. Lastly, the *(up, down)* mechanism is the single

volume scattering term that involves only one scatterer where the incident ray is scattered upward on the way to the Surface 1 by the scatterer.

2.3 Application of CEM Technique in RT Equation of Microwave Remote Sensing

Initially, the second-order radiative transfer equation with the incorporation of DM-PACT and IEM were only done on spherical scatterers in the dense snow and sea ice medium. Using the spherical shaped ice scatterers to replace the non-spherical scatterers in snow medium was to reduce the computational time and complex equations (Grenfell and Warren, 1999). Still, the shapes of the ice scatterers affect the result of the backscattering coefficient of the snow medium. The scattering property of the ice scatterer of the snow medium is the major factor to compute the snow albedo. There is a need to investigate the scattering properties of non-spherical ice scatterers in order to obtain accurate results of snow albedo to calculate the backscattering coefficient of snow medium (Tanikawa et al., 2006).

Non-spherical scatterers are needed to be used to compute the second-order radiative transfer equation for snow medium as they undergo complicated morphologies such as polycrystals and aggregates (Xie et al., 2006). Due to temperature change, snow on the ground confronts continuous condensation, sublimation and structural changes that lead to metamorphism (Pinzer and Schneebeli, 2009). However, it is difficult to derive equations for

the arbitrary shapes of these theoretical models to compute the backscattering coefficient as they involve lots of computational time.

There have been some research works done on the non-spherical scatterers to compute second-order radiative transfer equations for snow medium with multiple CEM. Therefore, CEM techniques are important to compute the backscattering coefficient and retrieve other parameters for the arbitrary shapes of the theoretical model of the earth terrain especially the snow and sea ice medium. Maxwell's equation of the complex shapes of the theoretical models can be computed using various numerical approaches generated by the CEM techniques (Tsang, Ding, Huang and Xu, 2013). In previous research, there are various numerical approaches that were applied in the analysis of the backscattering coefficient of snow and sea ice medium.

Discrete Ordinates Radiative Transfer (DISORT) was used to compute the snow reflectance properties for five shapes of ice scatterers which are the hexagonal solids, hollow columns and plate, bullet rosettes and aggregates. In this mentioned investigation, the wavelength affects the bidirectional reflectance of the snow (Xie et al., 2006).

Xu implemented the FEM in the computation of the Total and Scattered-Field Decomposition (TSFD) for layered sea ice (Xu, Brekke, Douleris and Melandsø, 2018). A two-dimensional surface of the sea ice was constructed, and the total and scattered fields are formulated using the FEM technique. FEM is a numerical approach that is based on the partial

differential equation. TSFD is a method where the incident wave is imprinted to the connecting boundary which is located between the total and scattered field (Liu et al., 2010). This mentioned FEM theoretical model was investigated to study the scattering effect from the subsurface of the sea ice with the roughness of the ice-water interface and penetration depth. These results were compared with MoM and Small Perturbation Model (SPM). The accuracy of the FEM model is influenced by the mesh size of the subdomains. The mesh size needed to be smaller than $\lambda/5$ to produce accurate data compared to other numerical approaches.

Besides, FDTD method was used to compute the scattering effect of the complex shapes of ice scatterer of cloud by another researcher. The shapes under investigation were hexagonal column and plate and also the stellar crystal. FDTD is capable to compute the scattering effect of the arbitrarily shaped particle and high frequencies were used to compute the polarimetric and extinction cross-section of the scatterers in the cloud (Tang and Aydin, 1995).

In addition, there were several numerical approaches that were applied to compute the scattering effect of the snow and sea ice medium for the forward model of microwave remote sensings such as Discrete Dipole Approximation (DDA) (Draine and Flatau, 1994), conjugate gradient-fast Fourier Transform (CG-FFT) (Liao and Sassen, 1994) and Generalized Multiparticle Mie (GMM) (Xu, 1995). However, these CEM techniques involve high computational time and are limited to the small size of scatterers

and small frequencies. Therefore, more research works need to be done to resolve these issues and obtain high accuracy in the results generation.

2.4 Model Development on Second-Order RT Equation using CEM Techniques

In this study, six shapes of ice scatterers of snow medium which are sphere, peanut, ellipsoid, cylinder, hexagonal column and droxtal will be used to compute the second-order RT equation to calculate the backscattering coefficient of the snow medium.

Mie scattering formulation is used to compute the phase matrix of spherical shaped single scatterer where the electrical and magnetic field of the scatterer can be calculated as shown in Eq 2.9 to 2.16. The calculated EM field is further used in a single scatterer's Stokes matrix computation, as shown in Eq 2.3.

Once the horizontal and vertical components of the Stokes matrix for the single scatterer are calculated, the phase matrix for the dense snow medium is calculated by multiplying the effective number density with the Stokes matrix of the single scatterer as presented in Eq 2.2. The size of the scatterers in the snow medium is fixed to the same volume to reduce the computational memory. Through this mentioned computation, the backscattering coefficient of the snow medium is obtained, and the backscattering coefficient results are analyzed through graphical data to study

the scattering mechanism of the snow medium. The scattering mechanism from each contribution, such as surface, surface-volume and volume scattering, can be studied through graphical data analysis. Hence, the backscattering coefficient results are analyzed with various snow parameters such as different layer thickness, incident angles, frequencies and volume fraction of snow medium.

The model development of the second-order RT equation for arbitrarily shaped scatterers is different from that of the spherical scatterers that were computed using the Mie formulation. Coupled FEM/MoM from FEKO software and RHESA play a significant role in calculating the Stokes matrix of arbitrary shaped single scatterer by generating the horizontal and vertical components of EM far fields.

The orientation of non-spherical scatterers in snow medium is set to the z-axis to reduce the 16 nonzero elements of the scattering matrix to 4 nonzero elements. It can be explained through the derivations of equations (Chan Fai, 2018).

The vertical and horizontal scattered electric field components can be computed by multiplying the scattering amplitude, S_{pq} with the vertical and horizontal incident field components respectively, E_v^i and E_h^i shown in Eq 2.29.

$$\begin{bmatrix} E_v^s \\ E_h^s \end{bmatrix} = \frac{e^{jkR}}{R} \begin{bmatrix} S_{vv} & S_{vh} \\ S_{hv} & S_{hh} \end{bmatrix} \begin{bmatrix} E_v^i \\ E_h^i \end{bmatrix} \quad (2.29)$$

R is the distance between the centre of the of the focused area to the observation point and is the wave number.

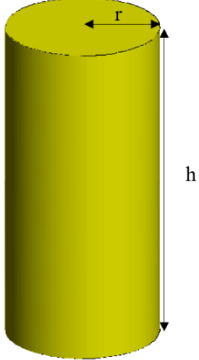
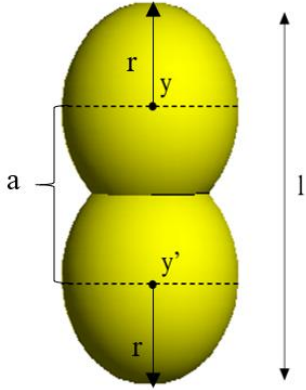
Through the relation of Eq 2.29 with Eq 2.5, the stokes matrix, \mathbf{M} can be obtained as shown in Appendix A.

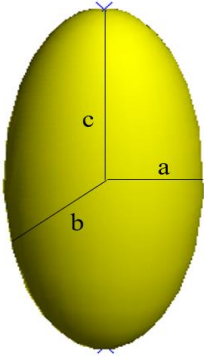
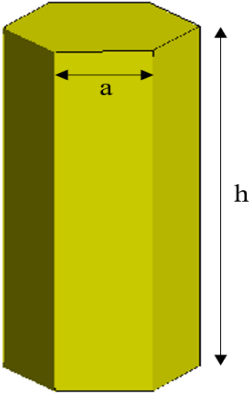
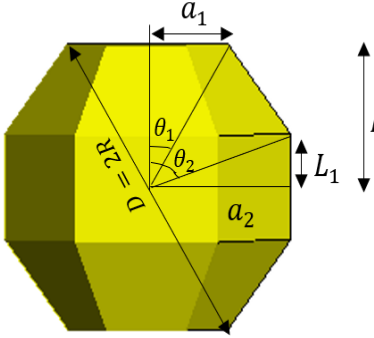
As the non-spherical shaped scatterers in this investigation are having rotational symmetry, the scattering matrix, \mathbf{M} is further reduced to eight nonzero elements. It is because the angular scattering is not considered in the computation as they are fixed to z-axis.

$$\begin{bmatrix} S_{11} & S_{12} & 0 & 0 \\ S_{21} & S_{22} & 0 & 0 \\ 0 & 0 & S_{33} & S_{34} \\ 0 & 0 & S_{43} & S_{44} \end{bmatrix} \quad (2.30)$$

In the backscattering computation of snow medium, the scatterers are assumed to be isotropic where in each set of computation, the ice scatterers in the snow medium are considered to have the same shapes. Therefore, the phase matrix in Eq 4 is further reduced to 2×2 matrix to resembles the computation of the spherical scatterers in the snow medium.

Table 2.1: List of shapes of ice scatterers and the dimension of the geometries

Shapes	The geometry of the shapes	Dimension of the geometries
Cylinder	 <p>A 3D diagram of a yellow cylinder. A horizontal arrow from the center of the top circular face to the edge is labeled 'r'. A vertical arrow along the right side of the cylinder, from the top to the bottom, is labeled 'h'.</p>	$V = \pi r^2 h$
Peanut	 <p>A 3D diagram of a yellow peanut shape, which is two spheres of radius 'r' joined together. The distance between the centers of the two spheres is labeled 'a'. The total length of the shape is labeled 'l'. The vertical coordinate of the upper sphere's center is labeled 'y', and the vertical coordinate of the lower sphere's center is labeled 'y''.</p>	$a = l - 2r$ $y = a$ $y' = -a$ <p>Note: y and y' represent the coordinate of the upper and lower spheres of the peanut shape. The volume of the peanut shape will be computed using the CAD software after the geometric modelling.</p>

Ellipsoid		$V = \frac{4}{3} a \cdot b \cdot c$
Hexagonal column		$V = \frac{3\sqrt{3}}{2} a^2 h$
Droxtal		$D = 2R$ $a_1 = R \sin \theta_1 \quad a_2 = R \sin \theta_2$ $L_1 = R \cos \theta_1 \quad L_2 = R \cos \theta_2$ $\theta_1 = 32.35^\circ \quad \theta_2 = 71.81^\circ$ $V = [(L_1 + 2L_2 + h)a_2^2 - ha_1^2]\sqrt{3}$ $h = \frac{a_1(L_1 - L_2)}{a_2 - a_1}$

As shown in Table 2.1, these non-spherical shapes of the ice-scatterers are categorized as rotationally symmetric particles. The surface of the cylinder

is not as smooth as the spherical scatterers as they have rectangular edges where they may affect the scattering property (Mishchenko, Travis and Macke, 1996) and thus affect the backscattering return of the snow medium. Furthermore, Lum designed a peanut-shaped ice scatterer which may result from the sintering and metamorphism process (Lum, Fu, Ewe and Jiang, 2017). Besides, the aspect ratio of the ellipsoid may affect the backscattering coefficient results of the snow medium. Thus, it is important to set the aspect ratio of the ellipsoid by equating its volume with the volume of the spherical scatterer (Du, Shi and Rott, 2010).

For the hexagonal shape of the ice scatterer of snow medium, there are two types of ice crystals; hollow and solid columns. Hollow columns of hexagonal-shaped ice scatterer are produced in a substantially supersaturated condition. Whereas, the solid column is formed in an equilibrium state (Magono, 1962). In this investigation, a solid column is chosen as it matches the volume of the spherical scatterer. On the other hand, droxtal shapes can be found in the arctic ice fog where the edge of these scatterers was initially smoothed where the scatterers were considered to be nearly spherical. However, as many similar images are being captured in the cirrus microphysical investigation, it is later called a *quasi-sphere* and this shape was used in the RT equations for snow medium. Various faces and the sharpness of the droxtal's edge makes the geometry of the droxtal more complex than the hexagonal column, thus affecting the backscattering coefficient of the snow medium (Yang et al., 2003). However, this shape is utilized for the investigation of the backscattering coefficient of the snow medium.

Therefore, these shapes are being used in this investigation to calculate the backscattering coefficient of snow medium and compare their results to validate the theoretical model of the snow ice scatterers by using the two different CEM techniques.

Far electric fields for single scatterer are calculated using FEKO software and RHESA computation separately and the array correction factor is incorporated into the far electric field to produce the coherent EM field of Stokes matrix as shown in Equations 2.2 and 2.3 in Chapter 2. The number of incident and scattered angles are set based on the contribution terms. For example, phase matrix computation for single scatterer, the number of scattered far electric field is set to 16 Gaussian quadrature, where the total number of far field is 256.

Although FEKO and RHESA approaches are different where the FEKO software focuses on FEM computation and RHESA focuses on MoM and EPA solution, both CEM techniques emphasise reducing the number of unknowns, thus reducing the computational memory and increasing the speed of the calculation of the backscattering coefficient for snow medium. The numerical approach of both CEM techniques will be further discussed in the next chapters.

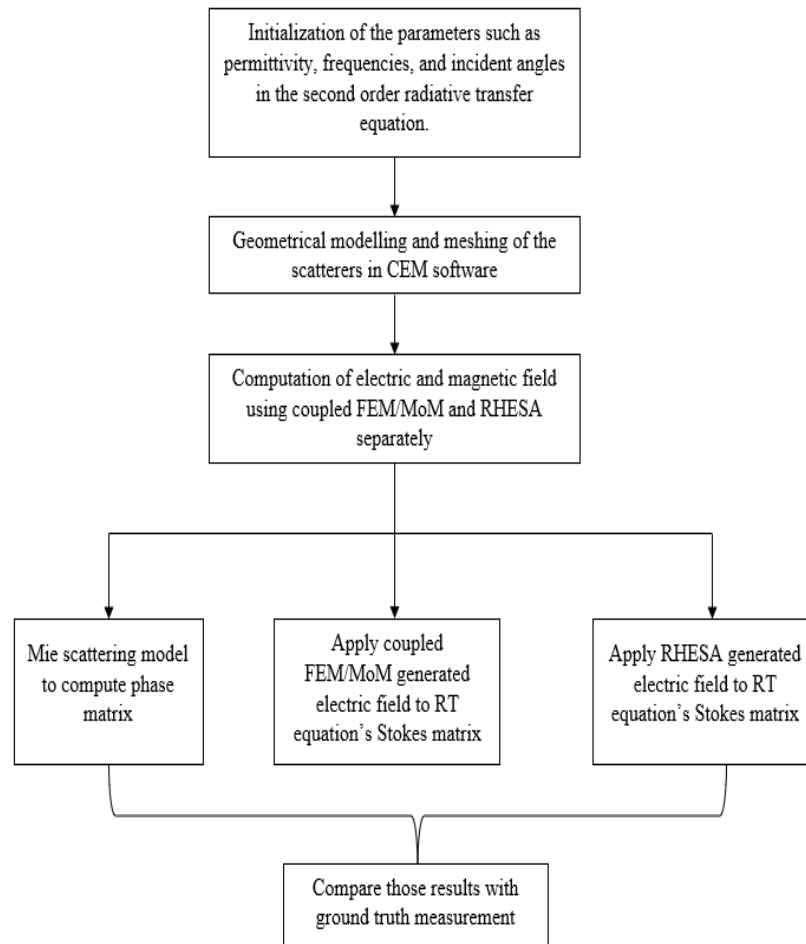


Figure 3.1 The flow chart of theoretical modelling of the scattering from snow medium

2.5 Summary

A general literature review and an introduction to the RT equation are included in this chapter. The second-order RT-PACT model for spherical and non-spherical ice scatterers for snow medium is presented. The equations for zeroth, first and second-order and the application of IEM and PAC on the RT

equations are discussed. The model development of the CEM techniques on RT equations is also explained in this chapter.

The equations and geometrical representations of the five non-spherical scatterers are also introduced. In addition, recent research efforts in applying CEM in RT equations for microwave remote sensing are also described. Chapter Five discusses the numerical approach of coupled FEM/MoM in detail.

CHAPTER 3

DEVELOPMENT OF RT MODEL WITH COUPLED FEM/MOM

3.1 FEM

FEM is a differential equation solver, and it is being utilized in various fields such as electromagnetics, acoustics, fluid dynamics, structural mechanics and the list goes on (Rylander, Ingelström and Bondeson, 2013). FEM can be derived from two perspectives which are the variational analysis and the CHR(PDE) of Maxwell's equations (Davidson, 2011). The role of FEM is to fragmentize the large region into simple geometries. Thus, the larger domain is discretized into small elements and the problem can be easily solved. (Baltzis, 2009)

Augustyniak listed several advantages of FEM in the application of electromagnetic problems (Augustyniak and Usarek, 2016). For example, FEM simulation permits the generation of the results for various types of variables and criteria. Furthermore, FEM can easily measure and retrieve various electromagnetic parameters in solid geometry. Besides, it is timesaving to utilize FEM to measure the electric and magnetic field of the experimental specimen and it is also able to generate the contour plot of the field which is readily available in many commercial software. FEM is also

able to handle complex geometries such as the unstructured mesh. Commonly, the meshes consist of triangles and tetrahedra shapes. For three dimensional geometries, tetrahedral meshes are used for the curved objects. (Rylander, Ingelström and Bondeson, 2013).

T.H Kwon (Tai, 2005) proposed the basic steps of the FEM as shown in the list below:

1. The governing mathematical equation is initialized which is commonly dealt with in the form of a differential equation.
2. A weak form of the integral equation is introduced which can be the variational approach or the weighted residual approach.
3. The object under the experiment is discretised into the elements.
4. An approximation of the field variable is presented over the segmented element.

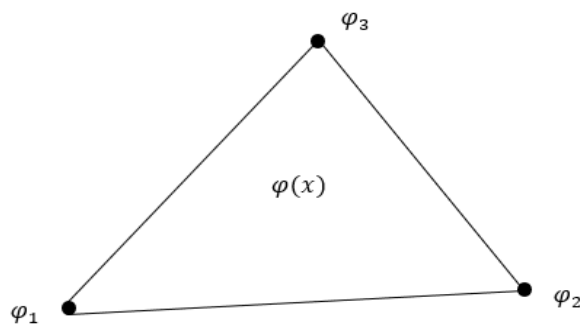


Figure 3.1 The nodal value and the interpolation function of the field variable

The equation is written as:

$$\varphi(\mathbf{x}) = N_1(\mathbf{x})\varphi_1 + N_2(\mathbf{x})\varphi_2 + N_3(\mathbf{x})\varphi_3 \quad (3.1)$$

where φ_i and N_i are the nodal values and the interpolation function respectively.

5. The integral form of each element is computed, and the global matrix equation is gathered.
6. The matrix equation is solved to obtain the unknowns and the final values are computed from the approximate solution.

Briefly, FEM can be mathematically written as:

$$f = \sum_{i=1}^N a_n h_n \quad (3.2)$$

where f is an unknown functional that needs to be calculated and h_n and a_n are the basis functions and unknown coefficients respectively.

The weighting function is written as:

$$W = \sum_{m=1}^M w_m \quad (3.3)$$

where w_m is known weight function.

An inner product for the two-dimensional problem can be defined as

$$\langle a, b \rangle = \iint_S ab \, dS \quad (3.4)$$

A linear system will be produced after an inner product of equation (3.1) is formed with equation (3.2).

$$\langle w_m, La_n h_n \rangle \quad (3.5)$$

where L is known as the differential operator.

The main benefit of the FEM method compared to other numerical approach is that it creates a sparse matrix with N_{FEM} unknowns which needs lesser computational memory (George, 1976) and can generate a high amount of mesh.

3.2 MoM

MoM is an electromagnetic solver that handles surface and volume integral equations based on frequency domain. Unlike other numerical approaches, MoM discretizes the surface and volume of the scatterer, thus this mentioned numerical approach is utilised in the scattering and radiation problems (Gibson, 2015). Therefore, the MoM numerical approach replaces the radiating structure with the equivalent currents, hence it is referred to as the surface currents (Davidson, 2011).

There are two types of numerical approaches in solving MoM in electromagnetic problems. They are referred to as the eigenvalue and deterministic problems. The former approach is a linear functional equation where the computation of the electromagnetic quantity is a direct method. The deterministic approach is the computation of the Eigen solution where the

nontrivial solution parameter is calculated first before determining the Eigen solutions (Ney, 1985).

The determinist equation of Method of Moment (MoM) can be written as: (Harrington, 1987)

$$L\{f(x)\} = g(x) \quad (3.6)$$

where L is a linear operator, $g(x)$ is a known operator and $f(x)$ is the operator that needs to be determined.

$f(x)$ can be further calculated as the expansion the summation of N weighted basis functions' series which can be described as

$$f = \sum_{n=1}^N a_n f_n \quad (3.7)$$

Where a_n is an unknown weighting function that needs to be calculated and f_n are the basis functions.

The substitution of the equation (3.7) and weighting functions, w_m lead to the equation:

$$\sum_{n=1}^N a_n \langle w_m, L(f_n) \rangle = \langle w_m, g \rangle \quad (3.8)$$

This finalized equation can be written in the matrix form

$$\bar{Z} \cdot I = V \quad (3.9)$$

where \bar{Z} , I and V are known as the impedance matrix, vector of unknown coefficient and excitation vector respectively. (Fu, Jiang and Ewe, 2016).

Equate equation (3.8) and (3.9) to become:

$$\bar{Z} = Z_{mn} = \langle w_m, L(f_n) \rangle \quad (3.10)$$

and

$$V = V_m = \langle w_m, g \rangle \quad (3.11)$$

In the eigenvalue approach, the MoM technique implements the matrix eigenvalue equation to solve problems in electromagnetics. Although the eigenvalue approach uses the same procedure as the deterministic equation, the former method is more complicated and various iterative schemes needed to be implemented. The derivation of the eigenvalue approach can be referred to in (Ney, 1985).

3.3 Comparison between FEM and MoM

Although FEM and MoM approaches look similar in the basic numerical analysis level, different algorithms are implemented in their approach. FEM method is based on the differential operator whereas the MoM method is based on the integral equation where the former has lots of zero in the matrix entries. Thus, FEM is called the sparse matrix whereas the MoM is referred to as the dense matrix (Davidson, 2011).

The steps for applying FEM and MoM on electromagnetic problems (Bhobe, Holloway and Picket-May, 2001) are listed in Table 3.1 where the differences of the steps are summarized.

Table 3.1: The steps of FEM and MoM applied in the electromagnetic problem.

No. of steps	Finite Element Method	Method of Moment
1	The domain of the scatterer is discretized into subdomains.	The integral equation of the system is derived.
2	The interpolation functions are selected.	The discretization of the integral equation is converted into the matrix equation.
3	The system of the equations is formulated.	The matrix elements are evaluated.
4	The solution of the equations is computed.	The matrix equation is solved, and the parameter of interest is gained.

3.4 Coupled FEM/MoM

Commercial software such as FEKO has many advantages such as geometrical modelling, user-friendly interface to initialize the direction of the multiple numbers of plane waves and the scattered electric and

magnetic fields. There are also options to choose the numerical solution to compute the electric and magnetic fields such as FEM, MoM, Physical Optics (PO) and the list goes on depending on the size of the geometrical structures (Altair Engineering Inc, 2015).

In this research, FEKO software is used to compute the electric field of the scatterers to compute the second-order backscattering coefficient of the snow ice medium for all spherical and non-spherical scatterers. In this software, coupled FEM/MoM numerical solution is chosen as the advantages of both FEM and MoM can be utilized in the computation of the scattered electric fields of the scatterers (Jakobus et al., 2008)

The novelty of this study is to incorporate the coupled FEM/MoM with DM-PACT and IEM to investigate the backscattering coefficient of snow medium through second-order RT computation. In previous research, different CEM techniques were utilized in the computation of the scattering properties of the scatterers in snow medium. For example, droxtal and hexagonal shaped scatterers were not used in the investigation of snow medium, especially when comes to this mentioned CEM technique.

The accuracy of the backscattering coefficients of snow medium using coupled FEM/MoM can be investigated and the suitability of this CEM technique can also be studied. In future, this investigation can aid for the scattering analysis of other earth terrains such as soil, vegetation and other terrains.

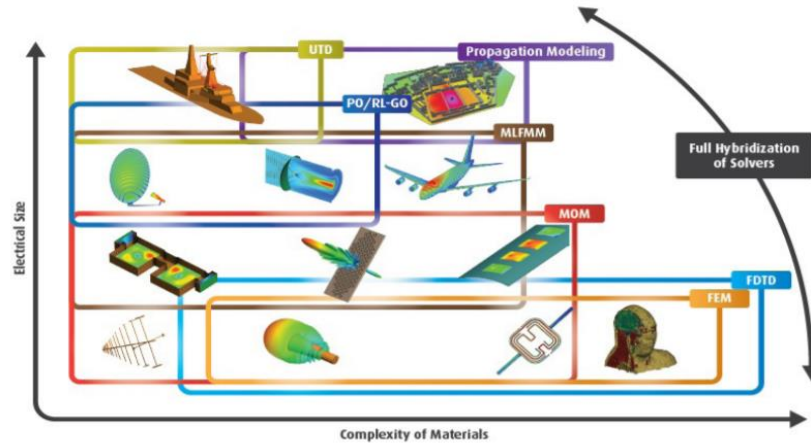


Figure 3.2 Various numerical approach applications based on the complexity and electrical size in FEKO software (Altair Engineering Inc, 2015).

PDE of FEM has a major drawback where it is unable to effectively produce an unrestrained radiating structure. It is crucial to create an absorbing outer surface boundary of the meshed area to create an unbounded geometry (Ali, Hubing and Dreniak, 1997). Thus, a boundary integral is needed to truncate the unbounded problem of the theoretical model of the scatterer (Ilic, Djordjevic, Ilic and Notaro, 2009).

In FEKO software, FEM numerical approach is integrated with the MoM technique to enhance the efficiency of the computation. This hybrid technique is implemented in FEKO software to prevent termination problems due to the radiation state application in the open area (Sumithra and Thiripurasundari, 2017).

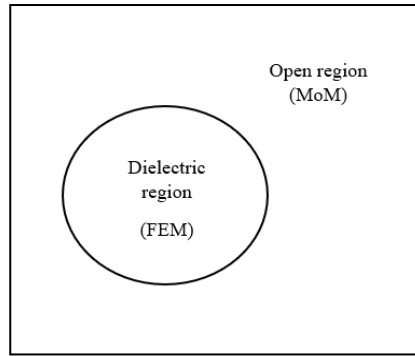


Figure 3.3 Illustration of the system that consists of the dielectric region and open region

As shown in Figure 3.3, the system is disintegrated into two parts; FEM is employed to the dielectric locality whereas the MoM is utilized to the outer locality (Ilic, Djordjevic, Ilic and Notaro, 2009). FEKO software implements an outward-looking method where the MoM part is solved in the beginning and serves as the FEM part's boundary condition (Jakobus et al., 2008). Therefore, this technique can decrease the requirement of computational memory per process and decrease the run time by employing several parallel processes to distribute the capacity of the computation (Jakobus, Bingle, van Tonder and Marais, 2008).

3.5 Formulation of Coupled FEM/MoM

According to Silvester (Silvester and Ferrari, 1996) and Davidson, (Davidson, 2011), the formulation of the coupled FEM/MoM starts with Maxwell's curl equation. The phasor form of Maxwell's curl equation is described as

$$\nabla \times \mathbf{E} = -j\omega\mu_0\mu_r\mathbf{H} - \mathbf{K}^{int} \quad (3.12)$$

$$\nabla \times \mathbf{H} = j\omega\epsilon_0\epsilon_r\mathbf{E} + \mathbf{J}^{int} \quad (3.13)$$

Where \mathbf{K}^{int} and \mathbf{J}^{int} represent the sources of electric and magnetic fields respectively. \mathbf{E} and \mathbf{H} the total resultant field. ϵ_r and μ_r represent the relative permittivity and permeability respectively.

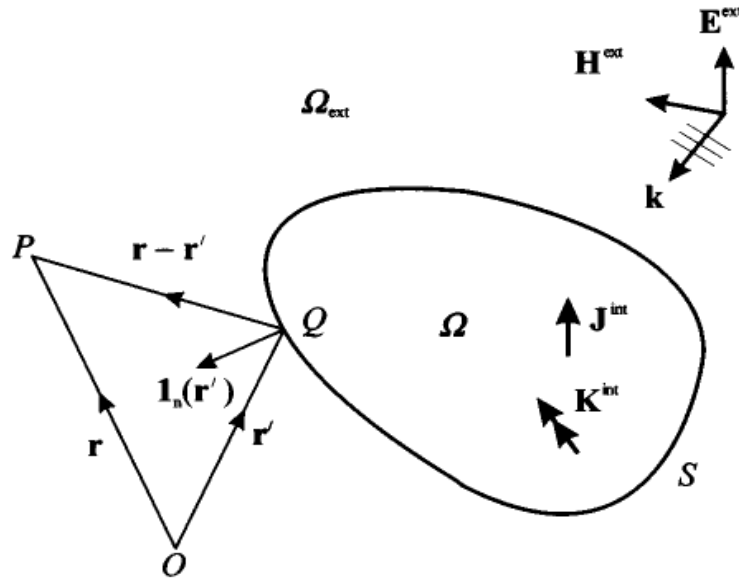


Figure 3.4 The configuration of the radiation and scattering mechanism (Silvester and Ferrari, 1996)

From Figure 3.4, consider the internal region as Ω whereas Ω^{ext} is the external region. The finite element discretization of the above equations will lead to the matrix equation of (Davidson, 2011):

$$[A]^E\{e\} + [B]^E\{h\}_S = \{c\}^E \quad (3.14)$$

The superscript E represents the electric field as the main variable, whereas the matrices $[A]$ and $[B]$ represent the FEM matrix that resulted from the volume's bilinear functional and surface's Neumann boundary condition

respectively. Vector $\{e\}$ and $\{h\}$ are the unknown coefficients of the volume's electric field and closure's magnetic field respectively. Lastly, the vector $\{c\}$ represents the current sources towards the volume.

This expression is further elaborated as:

$$A_{ij}^E = \int_{\Omega} \{\mu_r^{-1}(\nabla \times \vec{N}_i) \cdot (\nabla \times \vec{N}_j) - k^2 \epsilon_r \vec{N}_i \cdot \vec{N}_j\} d\Omega, \forall i \text{ and } j \quad (3.15)$$

$$= 1, \dots, N$$

$$B_{ij}^E = jk\eta \oint_S \vec{N}_i \cdot (\vec{N}_j \times \hat{n}) dS, \forall i = 1, \dots, N, j = 1, \dots, N_S \quad (3.16)$$

$$c^E = - \int_{\Omega} \vec{N}_i \cdot \{jk\eta \mathbf{J}^{\text{int}} + \nabla \times (\mu_r^{-1} \vec{K}^{\text{int}})\} d\Omega, \forall i = 1, \dots, N \quad (3.17)$$

where \vec{N}_i and \vec{N}_j represent the element shape functions where there are $N + N_S$ degrees of freedom. A supplementary control is needed to relate the surface magnetic fields with volumetric electric fields.

The derivation of electric field integral equation (EFIE) and Magnetic Field Integral Equation (MFIE) with the boundary S in the MoM representation is given as:

$$\vec{E}(\vec{r}) = \vec{E}^{\text{inc}}(\vec{r}) + \oint_S (\nabla \times \vec{G}(\vec{r}, \vec{r}') \cdot \{\hat{n}' \times E_S(\vec{r}')\} - jk\eta \vec{G}(\vec{r}, \vec{r}') \cdot \{\hat{n}' \times H_S(\vec{r}')\}) dS' \quad (3.18)$$

$$\vec{H}(\vec{r}) = \vec{H}^{\text{inc}}(\vec{r}) + \oint_S (\nabla \times \vec{G}(\vec{r}, \vec{r}') \cdot \{\hat{n}' \times H_S(\vec{r}')\} + \frac{jk}{\eta} \vec{G}(\vec{r}, \vec{r}') \cdot \{\hat{n}' \times E_S(\vec{r}')\}) dS' \quad (3.19)$$

\vec{G} and \hat{n}' represent the dyadic free space Green function and normal which is directed outward respectively. In a more compact equation, it can be written as:

$$-\vec{E} + L_{e1}^S(\vec{E}_s \times \hat{n}') + L_{e2}^S(\vec{H}_s \times \hat{n}') + \vec{E}^{\text{inc}}(\vec{r}) = 0 \quad (3.20)$$

The equation can be discretised in the form of the Galerkin procedure as shown in equation 3.21.

$$[B]^M \{e\}_S + [P]^E \{e\}_S + [Q]^E \{h\}_S + \{y\}^E = 0 \quad (3.21)$$

$[B]^M$ is the same as the $[B]^E$ in equation 3.16 except the notation $jk n$ is replaced with $-jk/n$. The other matrices are written as:

$$P_{ij}^E = j \frac{k}{\eta} \oint_S \vec{N}_i \cdot \{L_{e1}^S(\vec{N}_j \times \hat{n}) \times \hat{n}\} dS \quad (3.22)$$

$$Q_{ij}^E = j \frac{k}{\eta} \oint_S \vec{N}_i \cdot \{L_{e2}^S(\vec{N}_j \times \hat{n}) \times \hat{n}\} dS \quad (3.23)$$

$$y_i^E = j \frac{k}{\eta} \oint_S \vec{N}_i \cdot (\vec{E}^{\text{inc}} \times \hat{n}) dS \quad (3.24)$$

Thus, the equation can be discretised to produce:

$$[B]^E \{h\}_S + [P]^M \{h\}_S + [Q]^M \{e\}_S + \{y\}^M = 0 \quad (3.25)$$

Equations 3.21 and 3.22 are solved to eliminate $\{h\}_S$ in terms of $\{e\}_S$ and substituted into Equation 3.14.

3.6 Methodology of Coupled FEM/MoM in RT Equation

The far electric field is computed from the above approach using FEKO software and the array correction factor is incorporated into the far electric field to create the near field effect of the Stokes matrix. The phase matrix for FEKO is described as:

$$\bar{P} = \langle |\Psi|^2 \rangle_n \cdot \frac{1}{|E_0|^2} \cdot \begin{bmatrix} (E_V^S \times E_V^{*S})_{v-inc} & (E_V^S \times E_V^{*S})_{h-inc} \\ -(E_H^S \times E_H^{*S})_{v-inc} & -(E_H^S \times E_H^{*S})_{h-inc} \end{bmatrix} \quad (3.26)$$

E^S denotes the scattered electric respectively. H and V in the subscript of the electric field represent horizontal and vertical polarization respectively. E_0 is the incident electric field's amplitude. FEKO generated electric far-field's unit is Volt (V).

The FEKO simulation is utilized for the first and second-order scattering of snow medium. For zeroth-order surface scattering, the mechanism involves direct computation of the RT equation and does not require far-field scattering simulation from the FEKO software as there is no scatterer involved. 16 Gaussian quadrature points are used to calculate the phase matrix of the scattered angle.

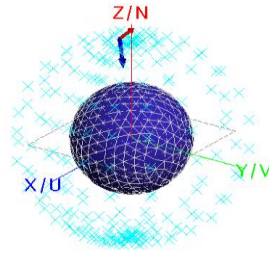


Figure 3.5: Example of the far field simulation for phase matrix of spherical scatterer from FEKO software.

In FEKO simulation, the geometries are constructed using CADFEKO and the far electric fields at various scattered angles are computed, compiled and applied in the Stokes matrix of RT equation for the calculation of the backscattering coefficient of snow medium as shown in Figure 3.5.

After all the far electric fields of the scatterer are generated in FEKO software, these data are collected and employed in Stokes matrix of Radiative Transfer equation for the calculation of the backscattering coefficient for various parameters and will be compared with Mie scattering model and satellite data. The flow chart of the methodology is simplified as shown in Figure 3.6.

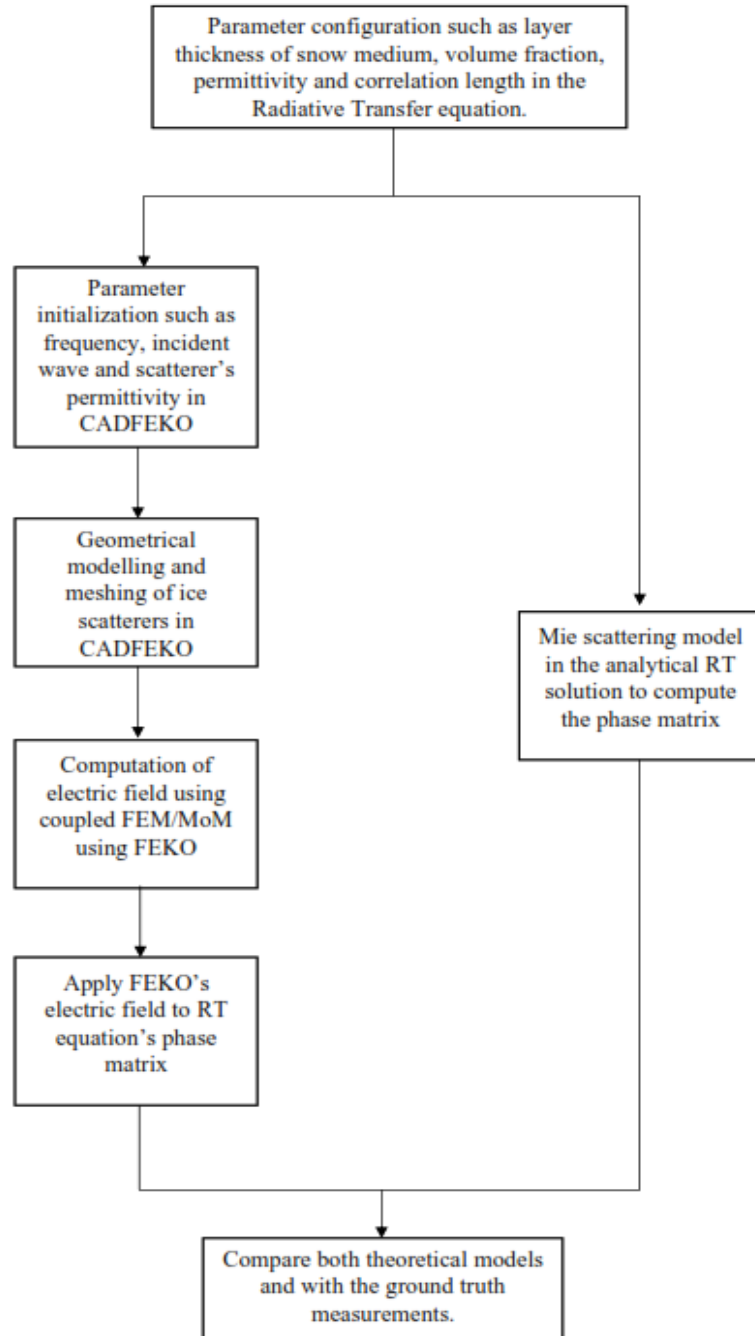


Figure 3.6 Flow chart of RT-Coupled FEM/MoM of the theoretical model of snow medium

3.7 Summary

The formulation of FEM and MoM and the application of coupled FEM/MoM in the RT equation is discussed in this chapter. In the next chapter, the formulation of RHESA is presented where the formulation of EPA and spherical equivalence surface are explained in detail.

CHAPTER 4

DEVELOPMENT OF RT MODEL WITH RHESA

Dielectric objects are preferred to be modelled with the volume integral equation (VIE) for electromagnetic computation (Li, Zhuang and Chen, 2018). Unfortunately, as the electrical size of the scatterer increases, this mentioned technique produces a huge number of unknowns due to the discretization of the volume of the scatterer (Fu, Jiang and Ewe, 2016). Furthermore, Method of Moment (MoM) is difficult to be applied in the radiation and scattering computation for a larger volume of scatterers as it requires high computational memory and time.

There are lots of development to compute the radiation for a larger size of scatterers and decrease the computational time such as Fast Multipole Algorithm (FMA) and Multilevel Fast Multipole Algorithm (MLFMA). For example, FMA is responsible for accelerating the matrix-vector computation in the integral equation of the EM problem. Unfortunately, the Green's function's convergence is high, particularly at low frequency. Thus, it undergoes a low-frequency breakdown as it could not obtain the evanescent waves (Xia et al., 2018).

4.1 Equivalent Principle Algorithm

The Equivalent Principle Algorithm (EPA) is introduced to solve the large electrical sized three-dimensional scatterers. EPA is focused on Domain Decomposition Method (DDM) where it disintegrates the main domain into several subdomains. Hence, the convergence of the iterative solver is faster. (Tiryaki, 2010) The DDM of the EPA technique transfers the unknowns of the elements to the unknowns on the equivalent surface that surrounds the scatterers (Li and Chew, 2007).

EPA is based on the Huygens' Principle where fields within or out of a closed surface are decided by tangential factor of the fields on the exterior.

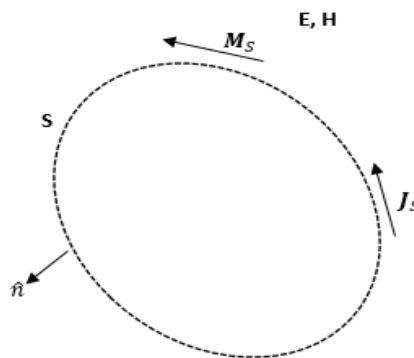


Figure 4.1 Huygens' principle: The tangential component of the field on the surface

EPA computes the EM problems by isolating a complex and huge problem into numerous basic components of the bodies with arbitrary shapes and each part is confined with the equivalent surface (Tiryaki, 2010). In this research, the EPA method will be used to calculate the phase matrix which is

shown in equation 4.1. The EPA method consists of three major steps, outside-in propagation, solving for the current on the object, and the inside-out propagation.

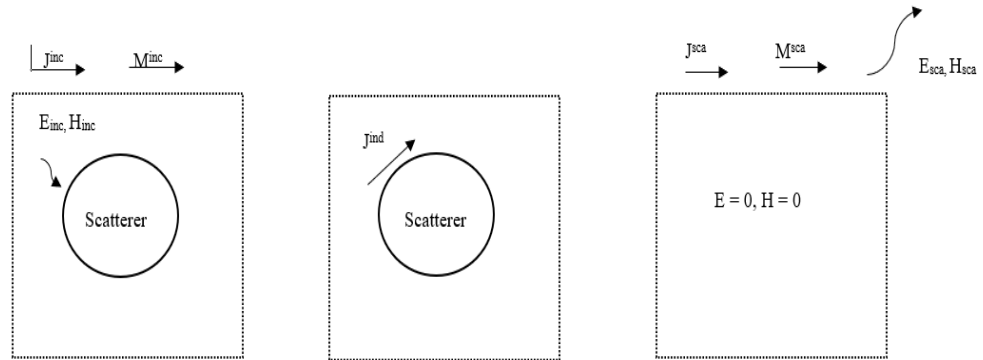


Figure 4.2 The major three steps in equivalence principle operator: From left to right: Outside-in propagation, current solver and inside-out propagation

In the first step which is known as the outside-in propagation, the equivalent sources on the equivalent surfaces will replace the original sources that produce incident electric and magnetic fields, \mathbf{E}^{inc} and \mathbf{H}^{inc} . In the second step, the electric current on the object will be calculated using MoM and this step is known as the current solver. Finally, a null field will be produced inside the equivalence surface and an original scattered field will be produced outside of the equivalence surface (Li, 2007). The formulation of the EPA is discussed in the next subsection.

4.1.1 Formulation of EPA

The formulation of the EPA (Li, 2007) starts from the electrical and magnetic field formulation as shown in Equation 4.1.

$$\begin{aligned}
\mathbf{E}(\mathbf{r}) &= \nabla \times \oint_S dS' g(\mathbf{r} - \mathbf{r}') \hat{\mathbf{n}}(\mathbf{r}') \times \mathbf{E}_S(\mathbf{r}') \\
&\quad - \frac{1}{i\omega\epsilon} \nabla \times \nabla \times \oint_S dS' g(\mathbf{r} - \mathbf{r}') \hat{\mathbf{n}}(\mathbf{r}') \times \mathbf{H}_S(\mathbf{r}') \\
&= -\nabla \times \oint_S dS' g(\mathbf{r} - \mathbf{r}') \mathbf{M}_S(\mathbf{r}') \\
&\quad - \frac{1}{i\omega\epsilon} \nabla \times \nabla \times \oint_S dS' g(\mathbf{r} - \mathbf{r}') \mathbf{J}_S(\mathbf{r}') \\
&= K_{EM}^S(\mathbf{r}, \mathbf{r}') \mathbf{M}_S(\mathbf{r}') + L_{EJ}^S(\mathbf{r}, \mathbf{r}') \mathbf{J}_S(\mathbf{r}')
\end{aligned} \tag{4.1}$$

The formula of the magnetic field is given as:

$$\mathbf{H}(\mathbf{r}) = -K_{HJ}^S(\mathbf{r}, \mathbf{r}') \mathbf{J}_S(\mathbf{r}') - L_{HM}^S(\mathbf{r}, \mathbf{r}') \mathbf{M}_S(\mathbf{r}') \tag{4.2}$$

From Equation 4.1 and 4.2, $\mathbf{M} = -\hat{\mathbf{n}} \times \mathbf{E}$, $\mathbf{J} = \hat{\mathbf{n}} \times \mathbf{H}$ and Green's function in the surrounding medium is given as $g(\mathbf{r} - \mathbf{r}')$.

The electric and magnetic field equations as shown in Equations 4.1 and 4.2 are decomposed from the whole domain into subdomains with the equivalence currents on the subdomains' surfaces. These Equations 4.1 and 4.2 are derived using the domain decomposition method. As mentioned in the previous section, there are three steps. These three steps can be described in Equation 4.3 (Chan Fai, 2018).

$$\begin{bmatrix} \mathbf{J}_S^{sca} \\ \frac{1}{\eta} \mathbf{M}_S^{sca} \end{bmatrix} = \begin{bmatrix} -\hat{\mathbf{n}}' \times K \\ -\frac{l}{\eta} \hat{\mathbf{n}}' \times L \end{bmatrix} \cdot [\bar{\mathbf{Z}}]^{-l} \cdot \begin{bmatrix} -L & -\eta K \end{bmatrix} \cdot \begin{bmatrix} \mathbf{J}_S^{inc} \\ \frac{1}{\eta} \mathbf{M}_S^{sca} \end{bmatrix} \tag{4.3}$$

$\begin{bmatrix} -\hat{\mathbf{n}}' \times K \\ -\frac{l}{\eta} \hat{\mathbf{n}}' \times L \end{bmatrix}$ is the inside-out operator, $[\bar{\mathbf{Z}}]^{-l}$ is the current solver and

$\begin{bmatrix} -L & -\eta K \end{bmatrix}$ is the outside-in operator.

Although EPA serves lots of advantages in the term of computational memory and run time, as the equivalent surface is too near (Tiryaki, 2010), the accuracy level is being reduced due to the representation of basis function and it causes difficulty in the numerical computation (Fu, Jiang and Ewe, 2016).

4.2 Relaxed Hierarchical Equivalent Source Algorithm (RHESA)

4.2.1 Spherical Equivalence Surface

As shown in Figure 4.2, the equivalence surface (ES) is constructed in the cubical form, and it can cause the current discontinuities where it will lead to the singular equivalence current and causes the current breakage (Li, 2007). There are methods to eliminate this issue such as increasing the number of meshes of the scatterers (Fu, Jiang and Ma, 2015), applying a tap basis scheme (Li, 2007), or introducing tangential-EPA (Tiryaki, 2010). However, they require higher computational power.

Therefore, a spherical form of equivalence surface is constructed as it is smooth and does not have any discontinuity, thus increasing the accuracy of the computation (Fu, Jiang and Ma, 2015). In this RHESA technique, the singularity of the integral operator is weakened by constructing spherical ES where they are constructed in the form of a hierarchical approach by introducing the parent and child group, where the ES does not have contact with the internal primary domain (Fu, Jiang and Ewe, 2016). It is demonstrated in Figure 4.3.

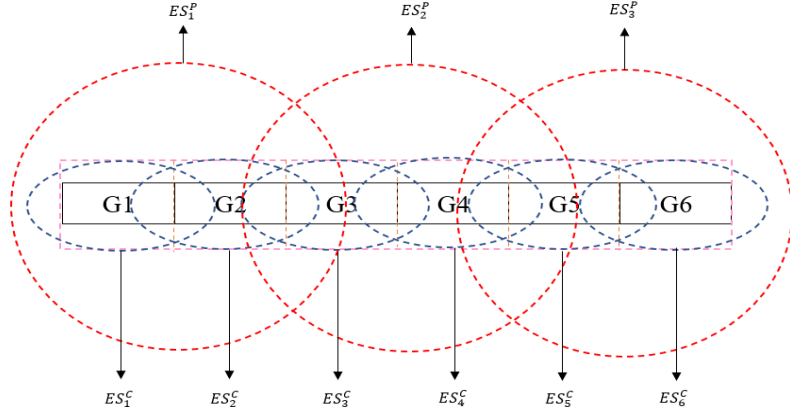


Figure 4.3 Demonstration of child and parent groups with spherical equivalence surfaces

The domain under investigation is first segregated in the cubical form to produce the lowest oct-tree level without any intersection. Each cube which is labelled with the alphabet G_i is surrounded by a child level (lower level) sphere which is labelled as ES_i^C and enclosed with parent level (high level) sphere which is categorized as ES_i^P . (Fu, Jiang and Ewe, 2016; Fu, Jiang and Ewe, 2016).

4.2.2 Formulation of RHESA

From Chapter 3, the finalized equation of Equation 3.9 is solved using MoM and this formulation cannot be utilized for the high number of unknowns. Thus, the EPA technique will be further improved using Relaxed Hierarchical Equivalent Source Algorithm (RHESA) which uses integral formulations. RHESA is used to reduce the total number of unknowns by further dividing the bodies into two forms of groups which are categorized into two fields'

interactions: near and far-field interactions (Fu, Jiang and Ewe, 2016). It can be illustrated as:

$$\bar{\mathbf{Z}} \cdot \mathbf{I} = \bar{\mathbf{Z}}_{near} \cdot \mathbf{I} + \bar{\mathbf{Z}}_{far} \cdot \mathbf{I} \quad (4.4)$$

From this equation, the near field is directly calculated using the Method of Moment. In contrast, the far-field can only be calculated using RHESA before using the Method of Moment. The RHESA method is a technique where the scatterers are divided into small classes to the smallest level of the oct-tree and an equivalent surface is used for the calculation of the scatterers.

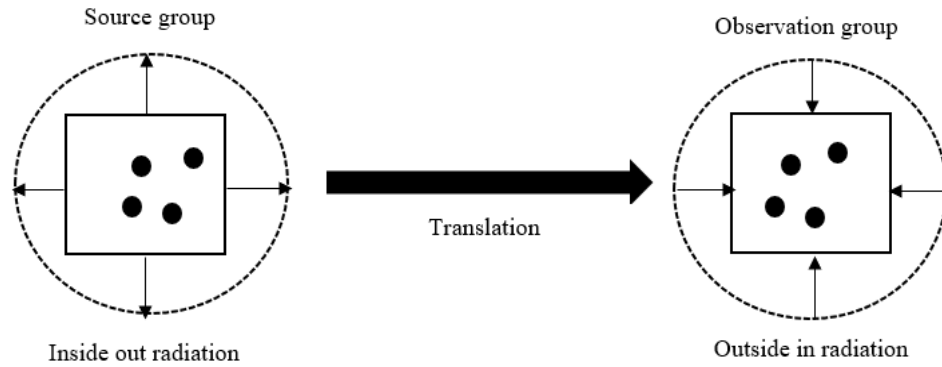


Figure 4.4 The three steps of RHESA's far-field computation

At the first step, the inside-out radiation is performed from the child level of the ESs to the parent level of the ESs at the source group. The incident EM fields are substituted with the equivalent sources of the source group based on the surface equivalent principle (Chan Fai, 2018). The inside-out radiation formulation (Fu, Jiang and Ewe, 2016) starts from the field equations on the ES which can be described in Equations 4.5 and 4.6.

$$\mathbf{E} = \mathcal{L}(\mathbf{J}_V) = \mathcal{L}(-i\omega\chi\mathbf{D}) \quad (4.5)$$

$$\mathbf{H} = \mathcal{K}(\mathbf{J}_V) = \mathcal{K}(-i\omega\chi\mathbf{D}) \quad (4.6)$$

The electric, \mathcal{L} and magnetic, \mathcal{K} fields integral operators are:

$$\mathcal{L}(\mathbf{X})(\mathbf{r}) = ik_0\eta \int_V \left[\mathcal{J} + \frac{\nabla\nabla}{k_0^2} \right] G_0(\mathbf{r}, \mathbf{r}') \cdot \mathbf{X}(\mathbf{r}') d\mathbf{r}' \quad (4.7)$$

$$\mathcal{K}(\mathbf{X})(\mathbf{r}) = \int_V \nabla G_0(\mathbf{r}, \mathbf{r}') \times \mathbf{X}(\mathbf{r}') d\mathbf{r}' \quad (4.8)$$

Where η and \mathcal{J} represent the background medium's intrinsic impedance and identity operator respectively.

The far-field that is radiated from the source group is computed by the ES of the source group for the observation group (Chan Fai, 2018). This process is called translation where it is computed using Stratton-Chu integral formulation (Stratton and Chu, 1939) which are described as:

$$\begin{aligned} \mathbf{E}(\mathbf{r}) &= \int_S \left[ik_0\eta_0 \mathbf{G}_0(\mathbf{r}, \mathbf{r}') \mathbf{J}_S^{eq}(\mathbf{r}') + \mathbf{M}_S^{eq}(\mathbf{r}') \times \nabla \mathbf{G}_0(\mathbf{r}, \mathbf{r}') \right. \\ &\quad \left. - \boldsymbol{\rho}_e^{eq}(\mathbf{r}') \nabla \mathbf{G}_0(\mathbf{r}, \mathbf{r}') \right] d\mathbf{r}' \\ &= \mathcal{C}_E(\mathbf{J}_S^{eq}, \mathbf{M}_S^{eq}, \boldsymbol{\rho}_e^{eq}) \end{aligned} \quad (4.9)$$

$$\begin{aligned} \mathbf{H}(\mathbf{r}) &= \int_S \left[ik_0/\eta_0 \mathbf{G}_0(\mathbf{r}, \mathbf{r}') \mathbf{M}_S^{eq}(\mathbf{r}') - \mathbf{J}_S^{eq}(\mathbf{r}') \times \nabla \mathbf{G}_0(\mathbf{r}, \mathbf{r}') \right. \\ &\quad \left. - \boldsymbol{\rho}_m^{eq}(\mathbf{r}') \nabla \mathbf{G}_0(\mathbf{r}, \mathbf{r}') \right] d\mathbf{r}' \\ &= \mathcal{C}_H(\mathbf{J}_S^{eq}, \mathbf{M}_S^{eq}, \boldsymbol{\rho}_m^{eq}) \end{aligned} \quad (4.10)$$

The current and charge integral operators for the EM field are represented by \mathcal{C}_E and \mathcal{C}_H respectively.

Finally, the outside-in radiation from the upper to the lower level is performed in the observation group. The radiated fields from the source group generate equivalent sources on the ES of the observation group, which generate electric and magnetic fields within the observation group (Fu, Jiang and Ewe, 2016). The electric field \mathbf{E}^F at the arbitrary position, \mathbf{r} can be described as:

$$\mathbf{E}^F(\mathbf{r}) = \sum_{G^S \in F(G^O)} \sum_{\mathbf{f}_n \in G^S} I_n \mathcal{C}_E^O \left\{ \begin{array}{l} \gamma_t^O \mathcal{C}_E^S[\mathbf{S}_E(\mathbf{f}_n)], -\gamma_t^O \mathcal{C}_H^S[\mathbf{S}_H(\mathbf{f}_n)], \\ \gamma_n^O \mathcal{C}_E^S[\mathbf{S}_E(\mathbf{f}_n)] \end{array} \right\} \quad (4.11)$$

\mathbf{S}_H and \mathbf{S}_E are the electric and magnetic field's equivalent sources respectively.

The whole process is aimed to avoid the current singularity and to increase the optimization of numerical integration. In this technique, the tap basis functions are not needed as the relaxed spherical equivalent surface is applied, hence the accuracy of the results can be increased.

4.2.3 Methodology of RHESA in RT Equation

The far electric field that is generated from the RHESA technique is implemented in second-order radiative transfer equation and the array and phase correction factor is integrated in the second-order RT equation in order to generate the near field effect of the Stokes matrix. The phase matrix for the RHESA is described as:

$$\bar{P} = \langle |\Psi|^2 \rangle_n \cdot \frac{d^2 \eta}{|E_0|^2} \cdot Re \left[\begin{array}{cc} (E_V^S \times H_H^{*S})_{v-inc} & (E_V^S \times H_H^{*S})_{h-inc} \\ -(E_H^S \times H_V^{*S})_{v-inc} & -(E_H^S \times H_V^{*S})_{h-inc} \end{array} \right] \quad (4.12)$$

E^s and H^s represent the scattered electric and magnetic far-fields respectively. V and H in the subscript of the EM field represent vertical and horizontal polarization correspondingly. E_0 is the incident electric field's amplitude. For RHESA simulation, the distance between the scatterer, d is included as the unit of RHESA simulated far-field is Volt per meter (V/m). η represents the intrinsic impedance.

The methodology of the RT-RHESA is similar to the RT-Coupled FEM/MoM technique. In this RHESA technique, Gaussian quadrature points are employed to compute the phase matrix of the scattered angle. The flow chart of the methodology for RT-RHESA is demonstrated in Figure 4.6.

The six shapes of ice scatterers of snow medium are structured using ANSYS APDL software and the mesh files are exported into RHESA simulation to compute the far EM field as shown in Figure 4.5.

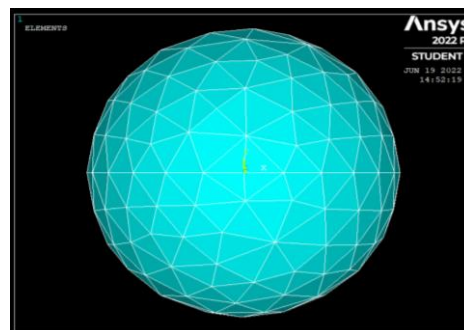


Figure 4.5: Mesh generation of the spherical scatterer from ANSYS APDL software for the generation of far electric and magnetic field from RHESA computation

The generated far EM fields are inserted into the second-order RT equation which were written in the form of FORTRAN code to calculate the backscattering coefficient of the snow medium. The obtained results are compared with Mie theoretical solution and ground truth data to validate the accuracy of the results.

In previous research, RHESA has only been tested for cylindrical and peanut ice scatterer shapes of snow medium. The research is further extended to utilize the RHESA for six shapes of ice scatterers of snow medium by implementing DM-PACT and IEM. Different CEM techniques and ice scatterer shapes have different effect on the backscattering coefficient of snow medium. The backscattering coefficient obtained from RHESA is compared with results generated from coupled FEM/MoM from FEKO software and Mie theoretical result to study the accuracy of the CEM techniques and to investigate the suitability of ice scatterers shapes of snow medium.

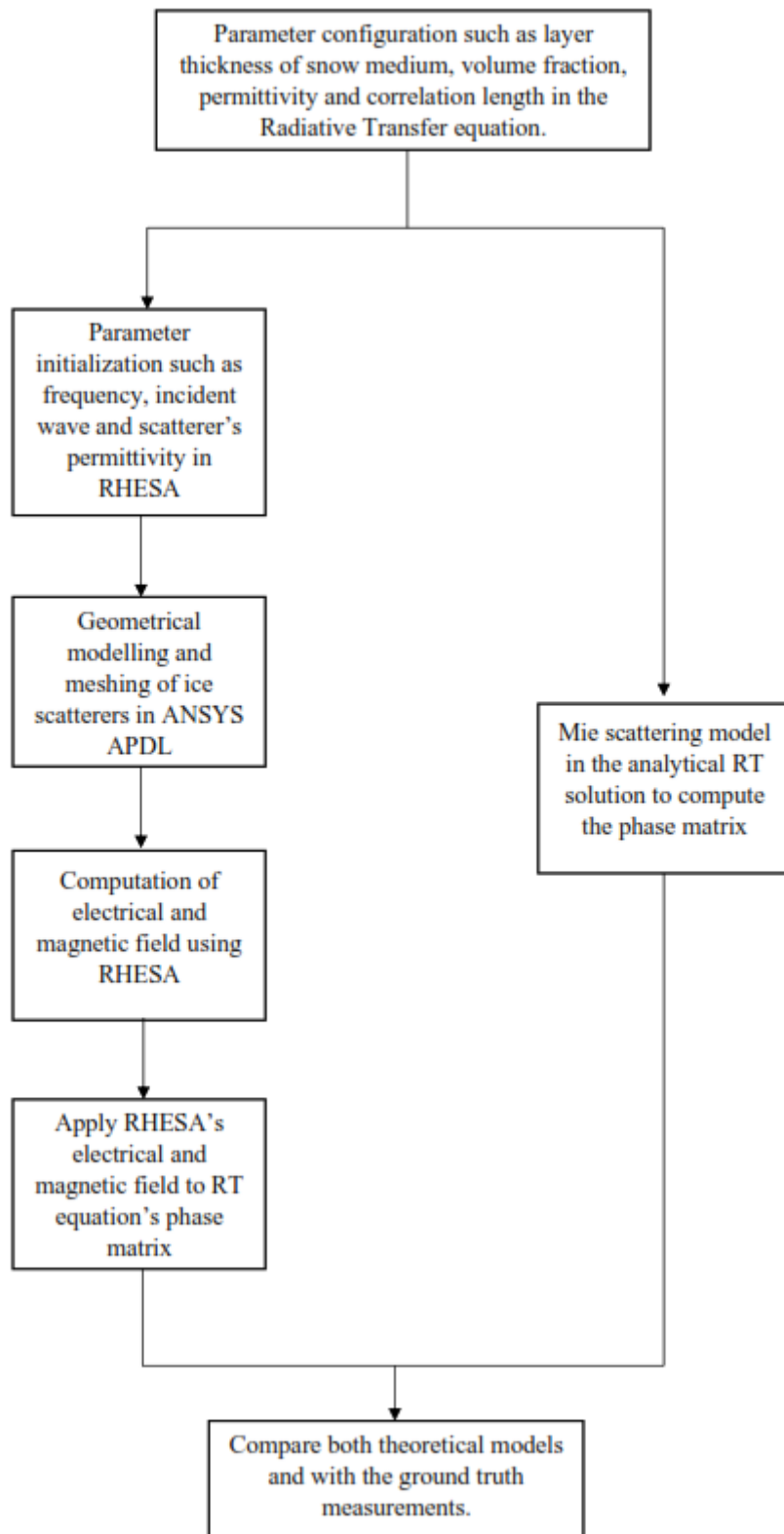


Figure 4.6 Flow chart of RT-RHESA theoretical model of snow medium

4.3 Summary

The formulation of EPA and RHESA and the application of the RHESA technique into the second-order RT equation is discussed in this chapter. In the next chapter, the backscattering coefficient of snow medium generated by the coupled FEM/MoM and RHESA will be investigated to study the accuracy of these numerical techniques and to study the theoretical model of six shapes of ice scatterers of snow medium.

CHAPTER 5

THEORETICAL ANALYSIS OF RT-COUPLED FEM/MOM AND RHESA

5.1 Introduction

In this chapter, the backscattering coefficient of spherical and non-spherical scatterers for various parameters are investigated to validate the accuracy of the theoretical model of non-spherical scatterers and identify the suitable ice scatterers' shapes as they experience metamorphism. This investigation is done by generating the far electric and magnetic fields of the ice scatterer of snow medium through CADFEKO and RHESA. The generated far fields are incorporated with DM-PACT to compute the complete backscattering returns of both co and cross-polarization of snow medium.

The backscattering returns of non-spherical scatterers are compared with the results of FEKO and RHESA generated spherical scatterers and Mie analytical results. The orientation of non-spherical scatterers is fixed to the z-axis as these scatterers are symmetrical to the z-axis. This is done to reduce the computational memory and thus increase the speed of the computation. Furthermore, the tetrahedron edge length for the mesh is set to be comparable to wavelength to increase the accuracy of the result.

The parameters under investigation are various incident angles, layer thickness, frequencies, and volume fractions. The other parameters needed to investigate the backscattering coefficient of the snow medium are listed in Table 5.1 (Chan Fai, 2018)

Table 5.1: Theoretical model parameter for snow medium

Parameters	Values used in the theoretical model
Scatterers' relative permittivity	(3.15, 0.001)
Top layer's relative permittivity	(1.0, 0.0)
Bottom layer's relative permittivity	(6.0, 0.0)
Background's relative permittivity	(1.0, 0.0)
Correlation length, RMS height of top surface (cm)	0.7, 0.12
Correlation length, RMS height of bottom surface (cm)	0.45, 0.06

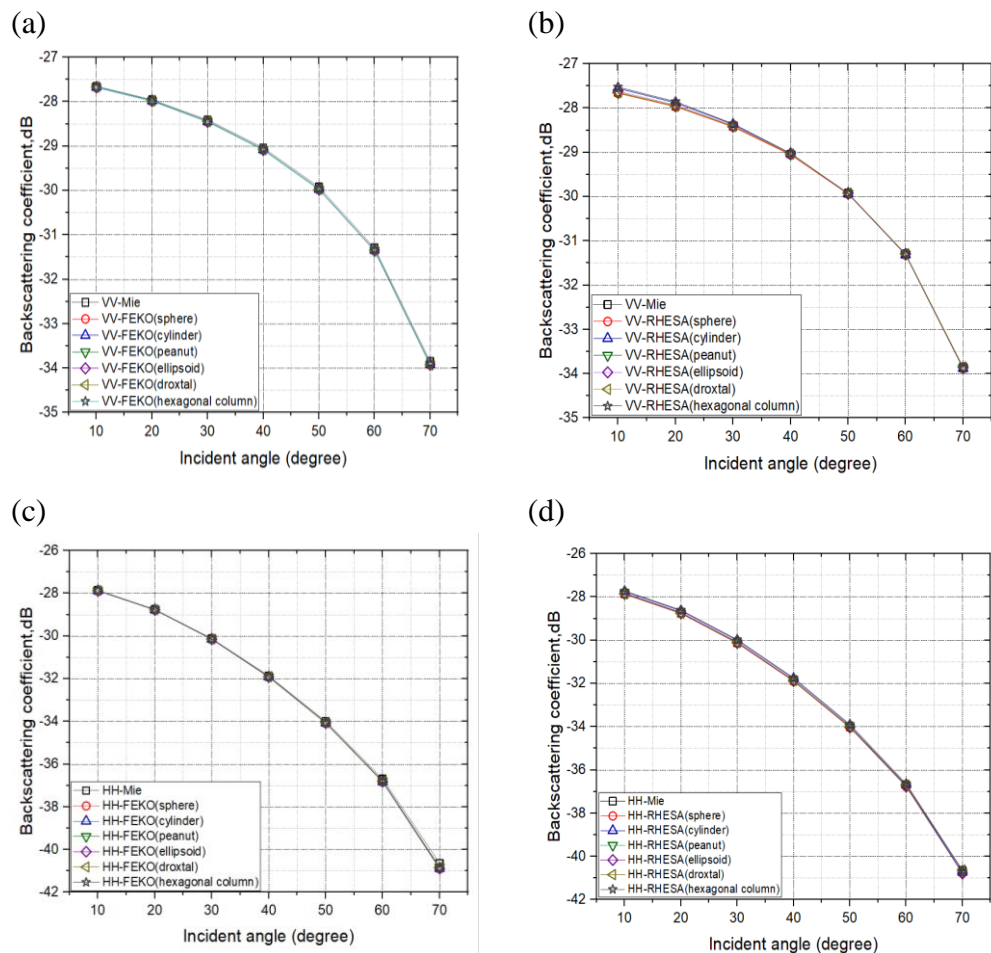
The radius of the spherical scatterer used in the FEKO and RHESA simulation is the same as the one used in the Mie scattering analysis which was 0.54mm. The volume of the non-spherical scatterers is set to be equivalent to the volume of the spherical scatterers.

5.2 Effect of Various Incident Angles on Backscattering Coefficient in FEKO and RHESA simulation

In Figure 5.1, the layer thickness of the snow medium is set to be 0.1m (Massom et al., 2001). and the volume fraction is set to be 20%. The volume fraction is computed based on the formula $d = \left(\frac{v_0}{v_f}\right)^{\frac{1}{3}}$ where d represents the average distance between the scatterers, v_0 and v_f represent the volume of

scatterer and volume fraction respectively. The frequency is set to be 5.0 GHz and the backscattering results generated from both CEM techniques are compared with each other together with the Mie analytical results.

As shown in Figures 5.1 (a), (b), (c) and (d), FEKO and RHESA simulated co-polarized backscattering coefficients for all shaped scatterers overlap with that of Mie analytical result. It is because at a long wavelength, the size of scatterers becomes smaller relatively, and they are treated almost the same as the Mie scatterer. In Figure 5.1 (e) and (f), VH polarized backscattering coefficient values for both Mie analytical results and both CEM simulated results are much lower compared with those of VV and HH as the multiple scattering effects are too small at this frequency.



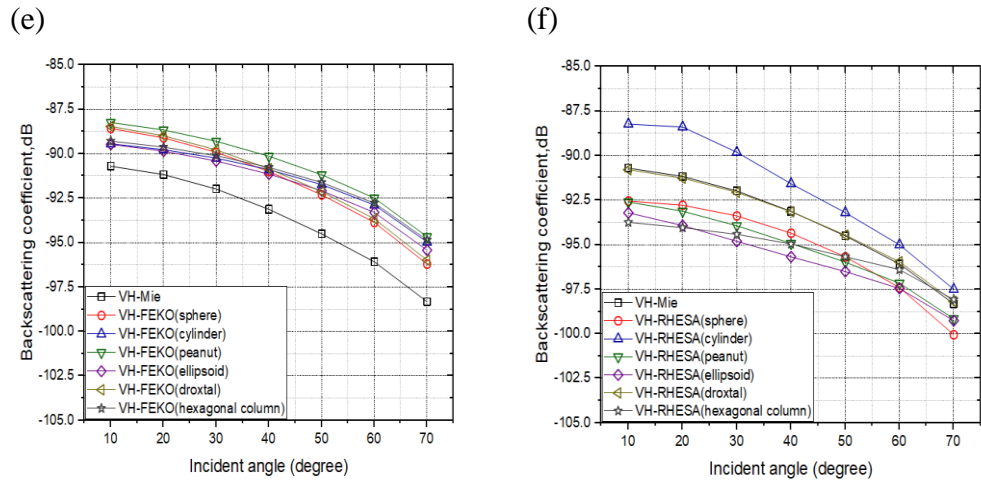


Figure 5.1 Comparison of Mie theoretical result with FEKO and RHESA simulated results of six shapes of scatterers of snow medium at 0.1m layer thickness and 5.0 GHz frequency for (a, b) VV polarization, (c, d) HH polarization and (e, f) VH polarization for various incident angles.

As shown in Figure 5.2, the layer thickness of the snow medium is further increased to 0.5m (Massom et al., 2001) to investigate the backscattering return for the layer with high thickness. The volume fraction remains the same which is 20%. For both VV and HH polarization, the results of six shapes of scatterers that are generated from both CEM techniques and Mie results are almost the same with some difference at high incident angles. For the VH backscattering coefficient, the values are still much lower than those of VV and HH.

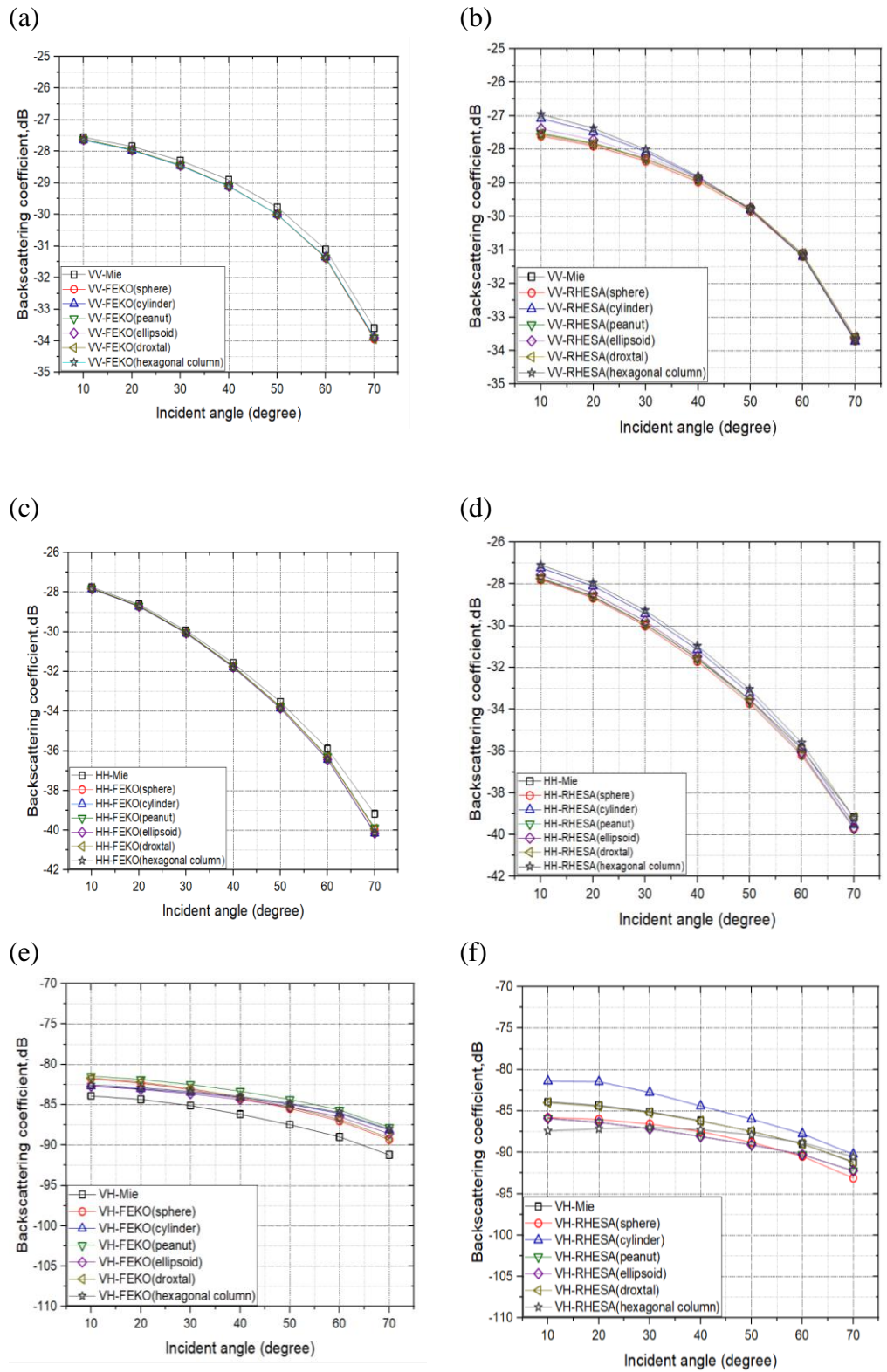


Figure 5.2 Comparison of Mie theoretical result with FEKO and RHESA simulated results of six shapes of scatterers of snow medium at 0.5 m layer

thickness and 5.0 GHz frequency for (a, b) VV polarization, (c, d) HH polarization and (e, f) VH polarization for various incident angles.

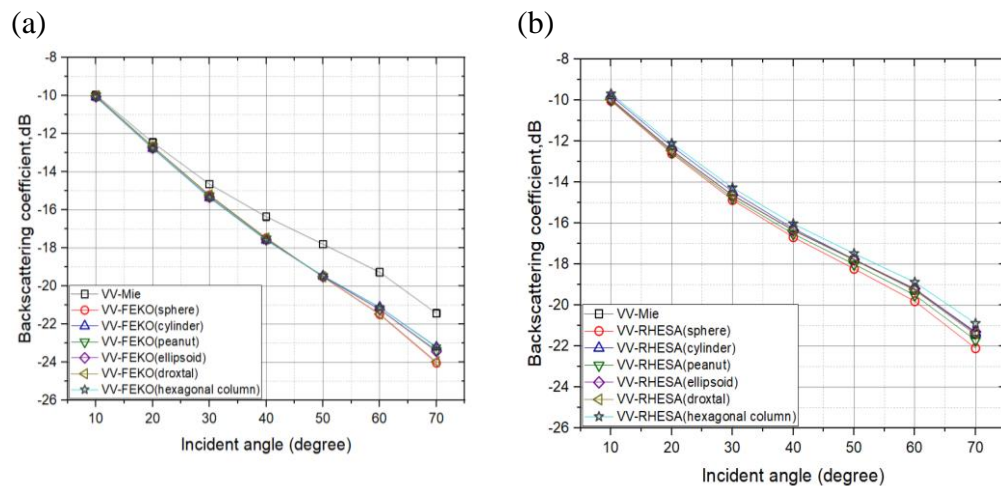
In the next two sets of results, the frequency is increased to 15.5GHz to investigate the effect of the frequency and layer thickness of the snow medium on the accuracy of the backscattering coefficient. The volume fraction remains the same which is 20%.

As shown in Figure 5.3, the layer thickness of the snow medium is set to 0.1m. For VV and HH polarization of FEKO simulation in Figure 5.3 (a) and (c), as the incident angle increases, the differences between Mie analytical data and FEKO simulated results become greater. At higher incident angles, the backscattering coefficient of five non-spherical scatterers is closer to the backscattering coefficient of the spherical scatterer of FEKO simulation. Droxtal shape shares a similar trend to the backscattering coefficient of FEKO simulated spherical scatterer because the geometry of droxtal has a similar resemblance to spherical scatterer. The highest difference between Mie theoretical result and FEKO generated results are droxtal and spherical shaped ice scatterers VV backscattering coefficients generated from FEKO software, where the difference is 2.5dB.

Unlike FEKO generated results, the RHESA generated backscattering coefficient for both spherical and non-spherical scatterer follow the trend of the Mie analytical result and the values are close to each other as presented in Figure 5.3 (b) and (d). The closest RHESA simulated backscattering

coefficient with Mie analytical result is droxtal for both co and cross-polarization. The highest difference between Mie theoretical result and RHESA generated result is spherical shaped ice scatterers generated VV backscattering return from RHESA, where the difference is 0.25dB. It can be concluded that the difference between RHESA and Mie theoretical result is smaller than that of FEKO.

In Figure 5.3 (e) and (f), FEKO and RHESA simulated data for spherical and non-spherical scatterers follow the trend of the Mie analytical result of VH polarization. However, FEKO generated results have a higher cross-polarized backscattering coefficient compared to Mie analytical result where cross-polarized backscattering returns are mainly caused by multiple surface scattering (Syahali et al., 2020).



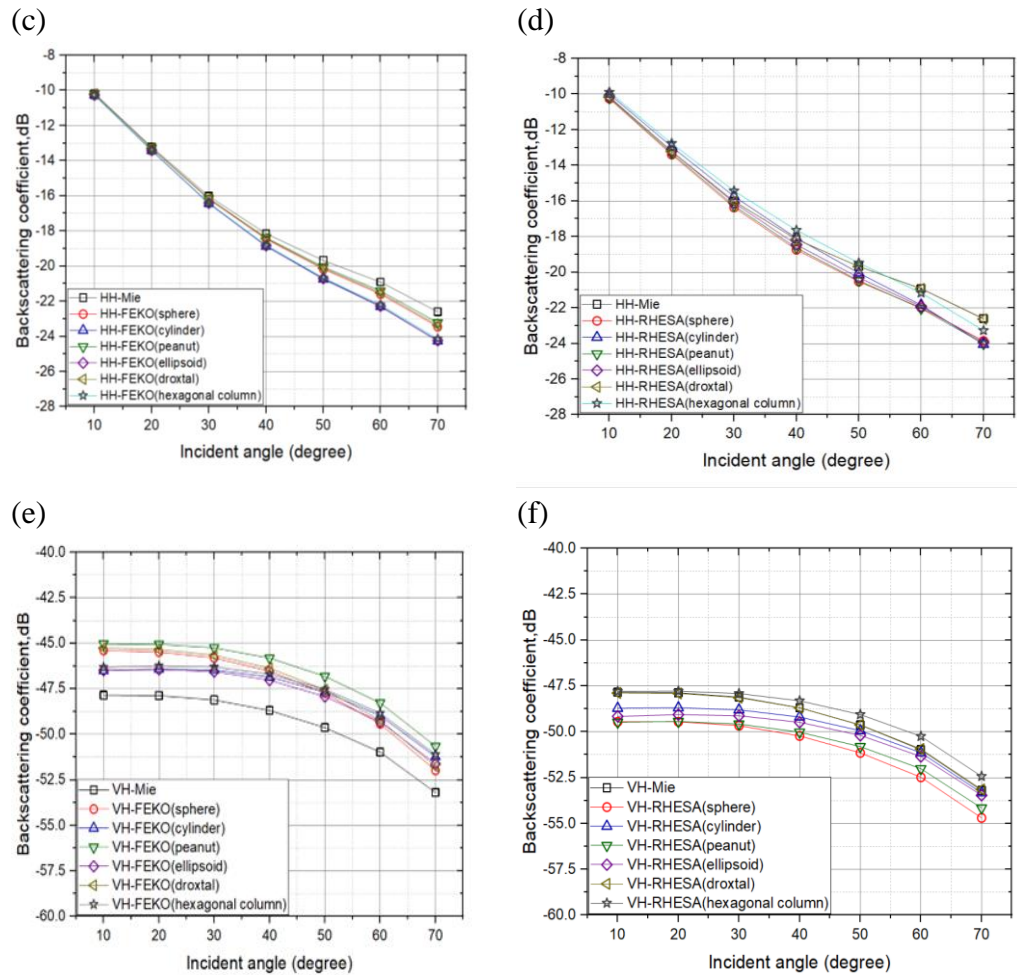


Figure 5.3 Comparison of Mie theoretical result with FEKO and RHESA simulated results of six shapes of scatterers of snow medium at 0.1 m layer thickness and 15.5 GHz frequency for (a, b) VV polarization, (c, d) HH polarization and (e, f) VH polarization for various incident angles.

In Figure 5.4, the layer thickness of the snow medium is increased to 0.5m and the frequency remains the same which is 15.5 GHz. Compared to the previous set of result in Figure 5.3, the difference between Mie analytical result and FEKO generated results become higher, especially for VV polarization in Figure 5.4 (a). The highest difference between Mie theoretical result and FEKO generated results are droxtal and spherical shaped ice

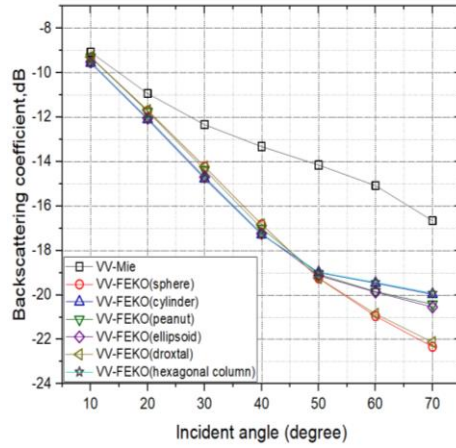
scatterers VV backscattering coefficient generated from FEKO software, where the difference is 5.3dB. Droxtal shape still shares a similar trend of the backscattering coefficient of FEKO simulated spherical scatterer due to the resemblance of its shape with spherical scatterer. The hexagonal column-shaped scatterer from the FEKO simulation has the biggest backscattering coefficient difference when compared with the spherical scatterer generated from the FEKO simulation. The difference is caused by the internal and external reflection of the various order of the polygon-shaped scatterer (Xie et al., 2006).

As shown in Figure 5.4 (b) and (d), the difference between RHESA generated results and the Mie theoretical results become slightly higher. However, the discrepancy between the theoretical result and RHESA generated results are lower than that comparison with FEKO generated results. The highest difference between Mie theoretical result and RHESA generated results is spherical shaped ice scatterers VV backscattering coefficient generated from RHESA, where the difference is 1.2 dB.

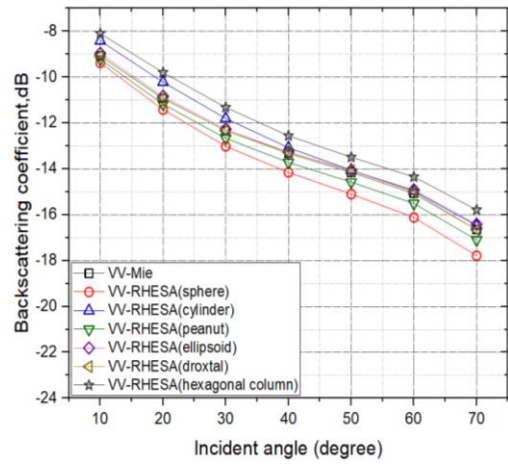
For VV polarization of RHESA simulation in Figure 5.4 (b), spherical and non-spherical scatterers share the same trend with Mie theoretical result. However, for HH polarization in Figure 5.4 (d), only RHESA generated droxtal-shaped scatterers follow the trend of the backscattering coefficient of the Mie theoretical results. For VH polarization in Figure 5.4 (f), there are slight differences between Mie theoretical results with RHESA generated results except for droxtal and hexagonal columns. Droxtal shape has the

closest backscattering coefficient with Mie theoretical results for both co and cross-polarization from both CEM techniques as it has the closest geometrical resemblance of spherical shape.

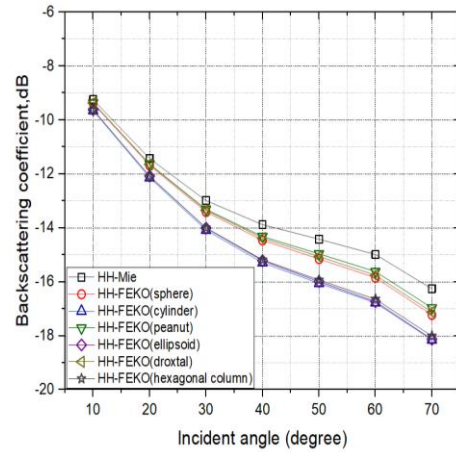
(a)



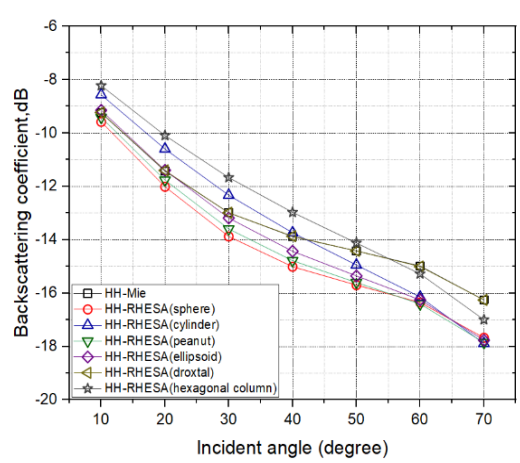
(b)



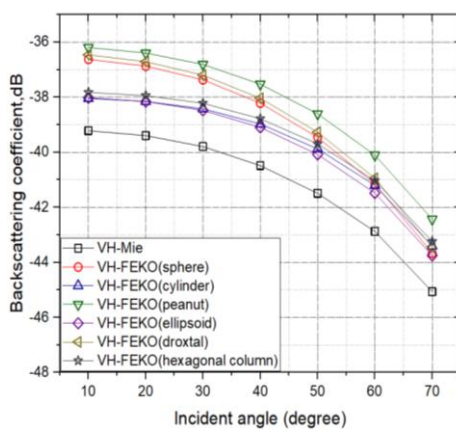
(c)



(d)



(e)



(f)

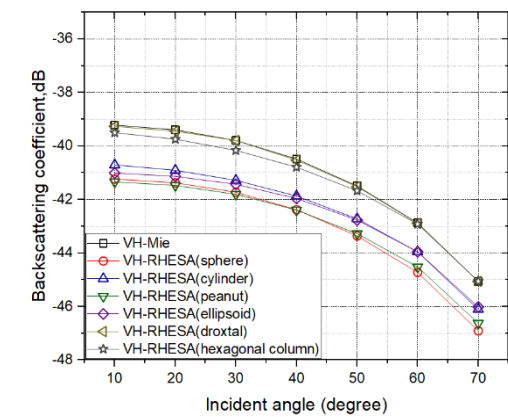


Figure 5.4 Comparison of Mie theoretical result with FEKO and RHESA simulated results of six shapes of scatterers of snow medium at 0.5 m layer thickness and 15.5 GHz frequency for (a, b) VV polarization, (c, d) HH polarization and (e, f) VH polarization for various incident angles.

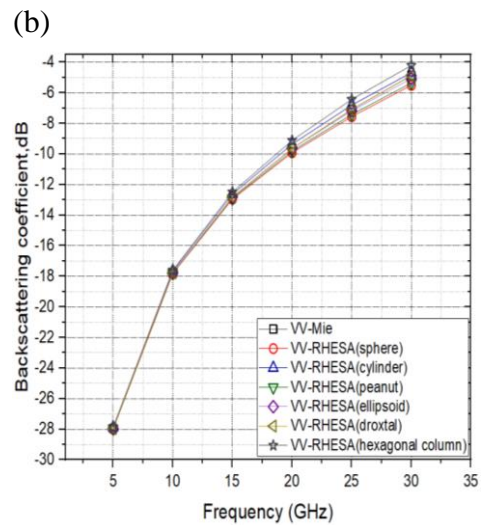
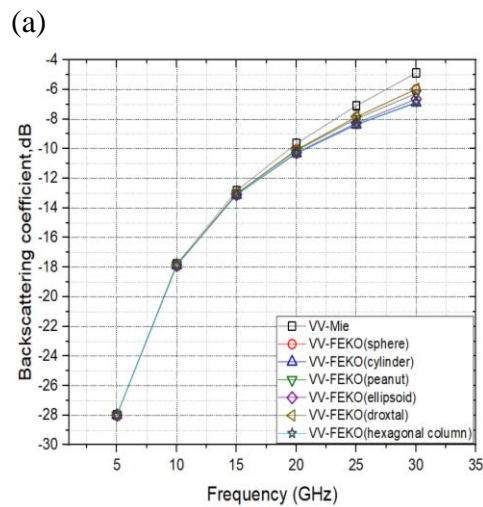
The cause of the difference in the result of FEKO generated backscattering coefficient and Mie analytical result may be caused by several factors. At high layer thickness, the number of scatterers in the snow medium is high as well. Thus, it causes higher volume and surface-volume interaction compared to the case with the thinner layer thickness as shown in Figure 5.3. Furthermore, as the incident angle increases, the Brewster angle effect is higher especially for VV polarization where it increases the effect of the multiple scattering. As shown in Figure 5.3 and 5.4 (a) and (b), the difference between FEKO and Mie generated results are higher for VV polarization compared to HH polarization. Besides, as the volume of the scatterers is low, the tapered incident wave cannot be applied to decrease the edge effect, especially at the higher incident angle and a higher incident angle which is closer to the glazing angle causes the deviation of the result for non-spherical scatterers (Xu, Brekke, Doulgeris and Melandsø, 2018).

Coupled FEM/MoM in FEKO focuses on the hybridization of two conventional methods which are the Finite Element Method and Method of Moment which are categorized as the low order basis functions. Thus, field and current computation are calculated based on the low-order basis function.

Hence, it will produce a high number of unknowns and reduce the convergence rate of the solution (Notaros, 2008).

5.3 Effect of Various Frequencies on Backscattering Coefficient in FEKO and RHESA simulation

In Figure 5.5, the backscattering coefficient for various frequencies is investigated at 0.1m layer thickness of snow medium and 20-degree incident angle. The volume fraction is set to be 20%. As the frequency increases, there is a slight difference in the backscattering coefficient between each result generated from FEKO and RHESA simulation. It is because as the frequency increases, the wavelength decreases, and the value is similar to the length of the tetrahedral edge of the scatterers' mesh. However, the discrepancies are too small, and they have the same increasing trend for both co and cross-polarized backscattering coefficients.



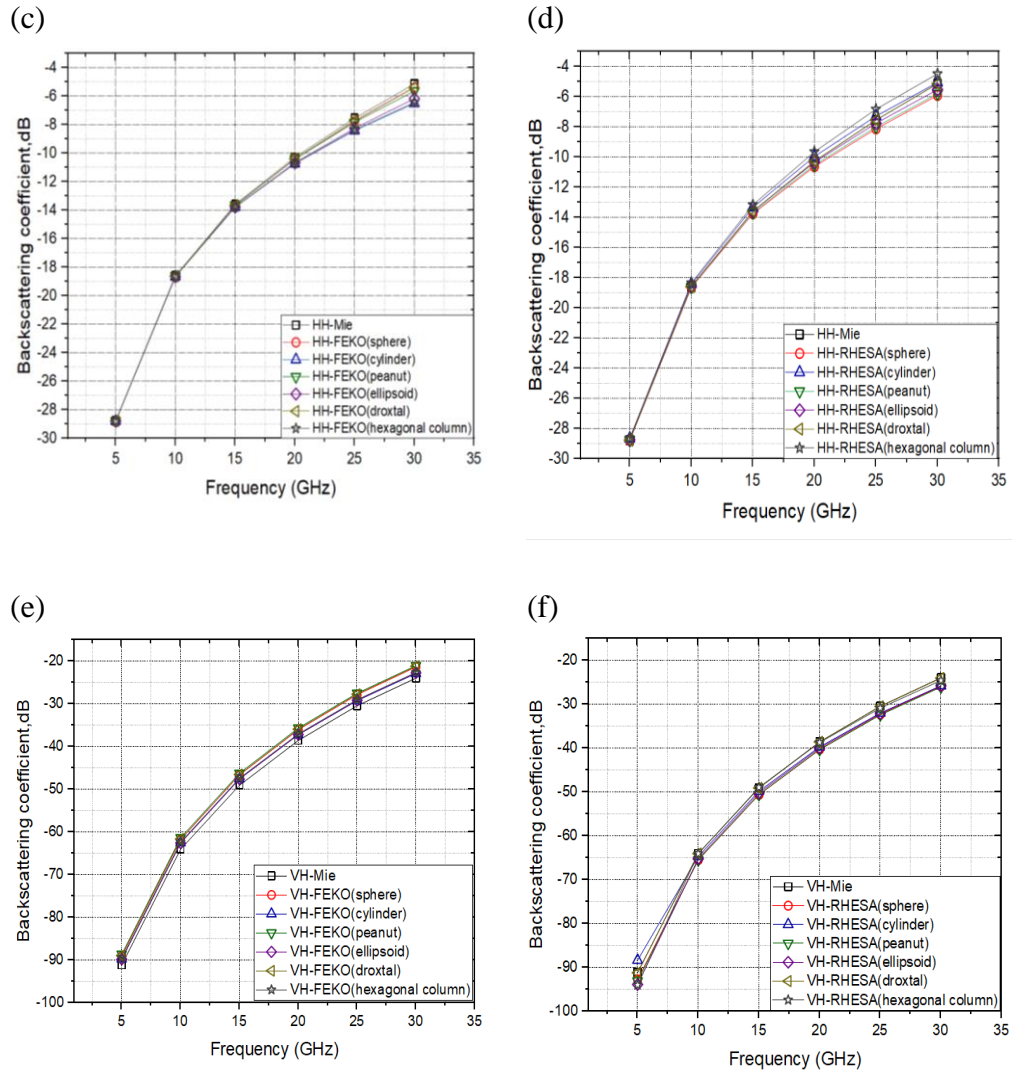


Figure 5.5 Comparison of Mie theoretical result with FEKO and RHESA simulated results of six shapes of scatterers of snow medium at 0.1 m layer thickness and 20-degree incident angle for (a, b) VV polarization, (c, d) HH polarization and (e, f) VH polarization for various frequencies.

5.4 Effect of Various Layer Thickness on Backscattering Coefficient in FEKO and RHESA simulation

Figure 5.6 describes the comparison of FEKO generated results of non-spherical scatterer for four values of the layer thickness of snow medium at 15.5 GHz frequency and 20-degree incident angle. The snow medium's layer

thicknesses that are used in this investigation are 0.1m, 0.5m, 2.15m and 12.5m and the volume fraction is set to be 20%.

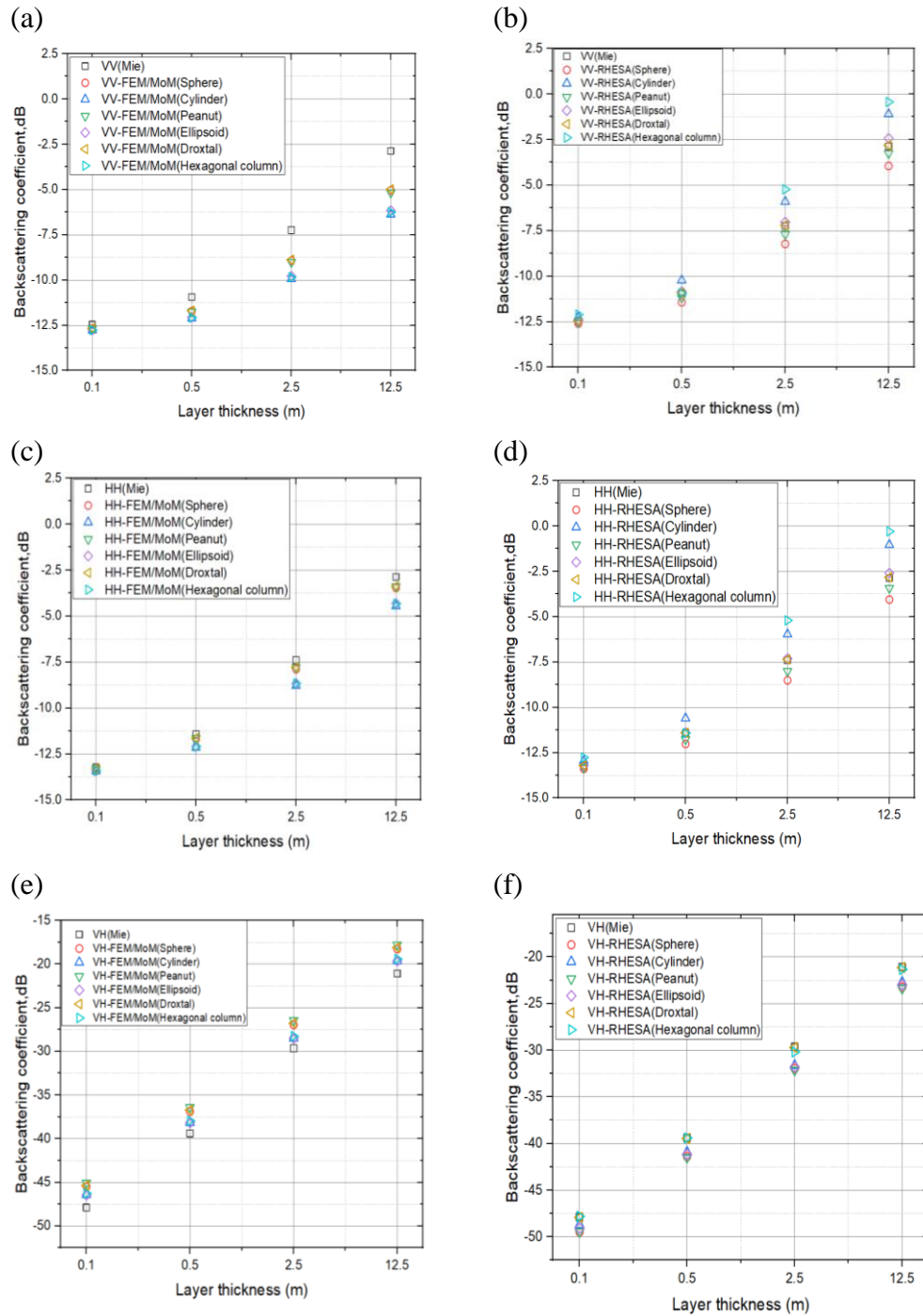


Figure 5.6 Comparison of Mie theoretical result with FEKO and RHESA simulated results of six shapes of scatterers of snow medium at 15.5GHz frequency and 20-degree incident angle for (a, b) VV polarization, (c, d) HH

polarization and (e, f) VH polarization for various layer thickness of snow medium.

As the layer thickness increases, the difference between FEKO generated spherical and non-spherical scatterers increases as well. The cylinder scatterer has the furthest difference in backscattering coefficient when compared with the spherical scatterer and Mie analytical solution followed by hexagonal column and ellipsoid at 12.5m layer thickness as shown in Figure 5.6 (a) and (c). However, peanut and droxtal shaped scatterers that are generated by FEKO software have the closest backscattering coefficient with the spherical scatterer and Mie analytical solution at 12.5m layer thickness of snow medium.

The difference between RHESA generated scatterers increases with Mie analytical solution, as the layer thickness increases. Hexagonal column scatterer followed by cylindrical scatterer has the furthest difference in the backscattering coefficient with both Mie analytical solution and RHESA generated spherical scatterer. Whereas the ice scatterer shape with backscattering coefficient closest to the Mie analytical solution and RHESA generated spherical scatterers are droxtal, peanut and ellipsoid as demonstrated in Figure 5.6 (b) and (d). The reason for the mentioned differences is due to the increase in the number of ice scatterers as the layer thickness increases, hence the scattering effect of these scatterers becomes more evident.

The differences in the cross-polarization backscattering return between spherical and non-spherical scatterers from both CEM techniques and Mie analytical results are too small.

5.5 Effect of Various Volume Fraction on Backscattering Coefficient in FEKO and RHESA simulation

Figure 5.7 describes the comparison of FEKO generated results of spherical and non-spherical scatterer for four values of volume fraction of snow medium at 15.5 GHz and 20-degree incident angle with Mie analytical solution. The volume fractions of snow medium that are used in this investigation are 10%, 20%, 30%, and 40% (K.Fung, 1994). The layer thickness is set to be 0.1m.

As shown in Figure 5.7(a), (c), and (e), for all types of polarization, the trend of difference between Mie analytical result and FEKO generated results are the same for all the volume fractions. The closest shapes with FEKO generated spherical shape and Mie theoretical results for both co and cross-polarization are droxtal and peanut.

As shown in Figure 5.7 (b) and (d), the hexagonal column and cylinder ice scatterers of snow medium have higher differences of co-polarized backscattering return with RHESA generated spherical scatterer of snow medium and Mie theoretical results as the volume fraction increases. However, peanut and droxtal shaped ice scatterers maintain the trend of co-polarized backscattering return with RHESA generated spherical scatterer and

Mie theoretical results whereas, for cases of scatterers of other shapes (such as hexagonal column and cylinder), the difference becomes more. For the cross-polarized backscattering coefficient as shown in Figure 5.7 (f), all of the ice scatterers follow the trend with the Mie theoretical results.

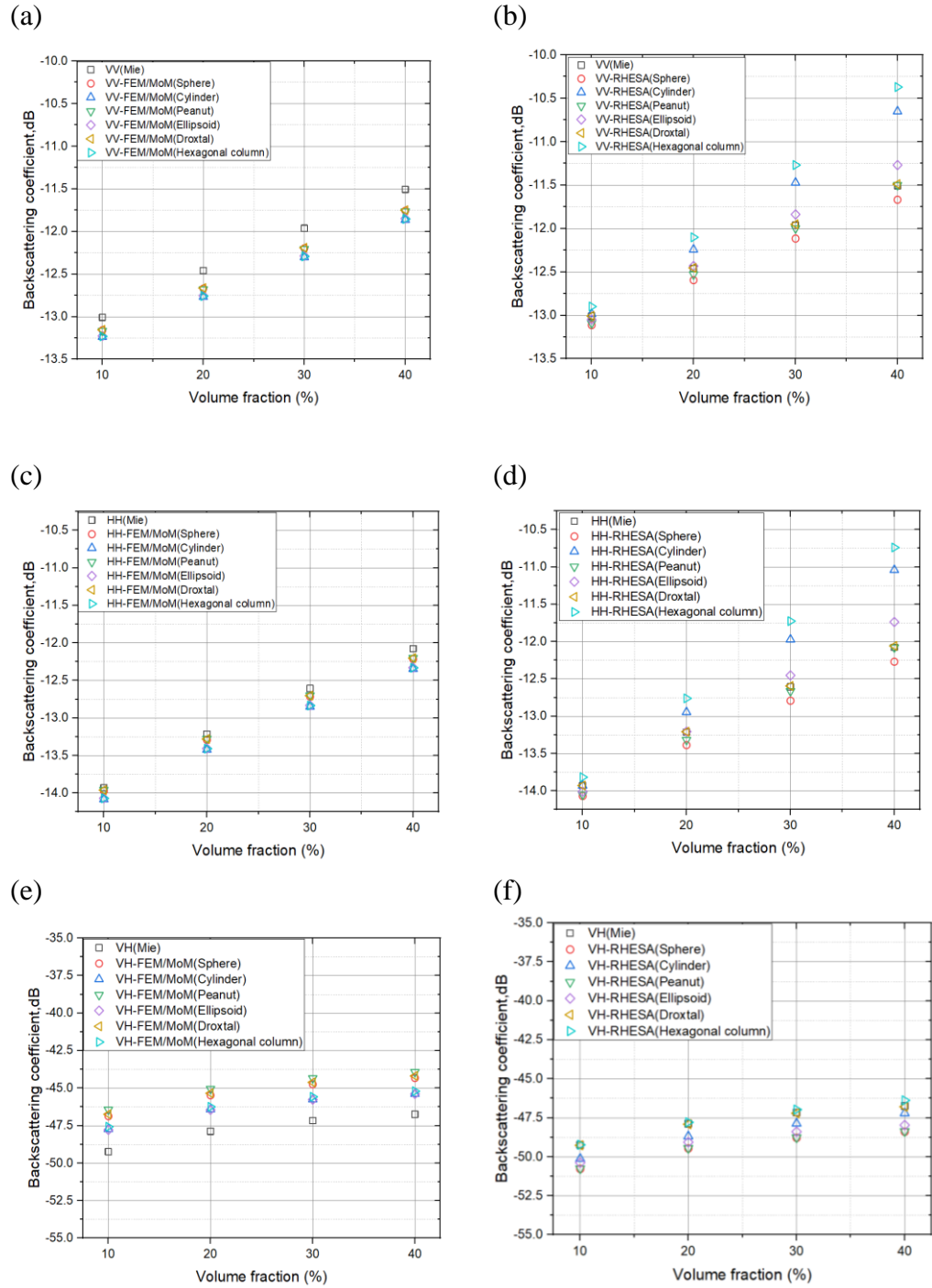


Figure 5.7 Comparison of Mie theoretical result with FEKO and RHESA simulated results of six shapes of scatterers of snow medium at 15.5GHz frequency and 20-degree incident angle for (a, b) VV polarization, (c, d) HH polarization and (e, f) VH polarization for various volume fraction of snow medium.

5.6 Summary

In this chapter, the investigation was done on the backscattering coefficient generated by six shapes of the ice scatterers of snow medium through coupled FEM/MoM and RHESA. The effect of layer thickness, incident angles, frequencies and volume fraction are studied using the second-order RT equation. As the frequency and layer thickness increase, the discrepancies between the Mie theoretical result and FEKO generated result are higher compared to RHESA generated result. It is because FEKO implements hybridization of two conventional CEM techniques, where they are based on the lower-order basis function. Thus, field and current computation are computed based on the low-order basis function. It will produce a high number of unknowns and reduce the convergence rate of the solution (Notaros, 2008). The discrepancies become more apparent when the layer thickness of the snow medium increases and the number of scatterers in the medium increases, thus increasing the interaction among the scatterers. Hence, the number of unknowns for the field computation increases.

On the other hand, RHESA computation is based on a high-order basis function, lowering the number of unknowns and preventing the current discontinuity due to the spherical equivalent surface, increasing the backscattering accuracy return. Due to these advantages, the discrepancy between RHESA generated results, and Mie theoretical results are low despite the increase of the layer thickness of snow medium and frequency.

In the next chapter, these CEM-generated results are further compared with the ground truth measurement to validate the accuracy of the CEM-generated results and compare the efficiency of the application of two CEM methods in the second-order RT equation for snow medium.

CHAPTER 6

COMPARISON OF CEM THEORETICAL MODEL WITH GROUND TRUTH MEASUREMENT

6.1 Introduction

In this section, the CEM generated backscattering coefficients of snow medium are compared and evaluated with the ground truth data to examine the accuracy of the CEM techniques and also to justify the shape of the geometrical models that can represent the ice scatterers of the snow medium. In this research, there are three sets of frequencies that are investigated to compare the CEM generated backscattering return with the ground truth measurement. The three sets of frequencies are L, C and Ku Band.

6.2 Comparison of CEM Techniques Generated Backscattering Coefficient of Snow Medium with CLPX Data at L-Band Frequency

The first set of the investigation is found from the NASA Cold-Land Processes Field Experiment (CLPX) and the experiment was performed by the University of Michigan (Sarabandi, 2003). In this set of investigations, the ground truth measurement data was obtained from the Intensive Observation Period 3 (IOP 3) at Local Scale Observation Site (LSOS) where the location of

LSOS is a small investigation site (0.8 ha) which is situated at Fraser MSA (-105.88 306 Lat, 39.90 172 Lon) (Marshall, Koh and Forster, 2004).

As shown in Figure 6.1, the data is based on the IOP 3 obtained on 21st February 2003. The list of parameters can be referred to in Appendix B. The frequency used in this investigation is L Band which is 1.25 GHz. The spherical scatterers' radius used was 0.54 mm (Chan Fai, 2018) where the volume of the arbitrary shapes of scatterers are set to be the same as the spherical scatterer's volume. All the shapes of the scatterers simulated by FEKO and RHESA overlap with the Mie analytical result. Therefore, all six shaped scatterers have the same traits as spherical scatterers at L Band. When the theoretical data are compared with the CLPX data, the difference is biggest at the lowest incident angle which is 20 degrees. At 35 degrees incident angle. All Mie, FEKO and RHESA simulated VV-polarized backscattering coefficients are nearest with CLPX data with a better fit. It can be concluded that in the low frequency, both CEM techniques are suitable to be used in the backscattering coefficient computation for the snow medium.

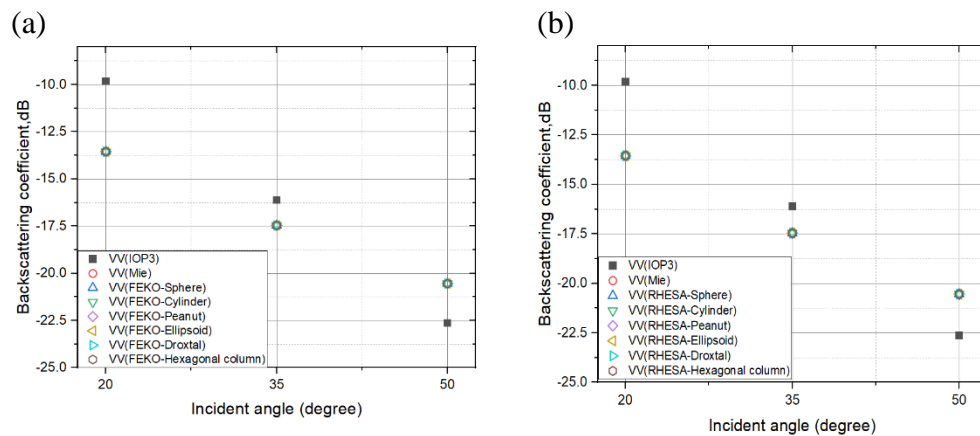


Figure 6.1 Comparison of VV backscattering coefficient of six shapes of ice scatterers produced by CEM methods (a) coupled FEM/MoM and (b) RHESA with CLPX data dated 21/2/2003 at L-Band frequency

6.3 Comparison of CEM Techniques Generated Backscattering Coefficient of Snow Medium with RADARSAT Data at C-Band Frequency

The second set of ground truth measurements focuses on the ground truth data which was taken from ice shelf of Antarctica in Scott Base, Ross Island using the RADARSAT satellite at 5.3 GHz frequency (C-Band). The radius of the spherical scatterers was approximated to be 1.1mm (Chan Fai, 2018) and the rest of the shapes of ice scatterers are set to be the equivalent as that of the spherical scatterer. The list of parameters can be obtained from Appendix B. The ice shelf thickness was approximated to be around 250 m (Albert, Lee, Ewe and Chuah, 2012).

Figure 6.2 demonstrates the comparison of CEM generated HH backscattering return with the RADARSAT DATA. As shown in Figure 6.2, at Site A, the closest CEM generated HH backscattering coefficient with the RADARSAT data is FEKO generated result for spherical scatterer. Except for FEKO generated result for the spherical scatterer, RHESA generated backscattering returns of non-spherical scatterers are nearer to the RADARSAT data compared to the FEKO generated results. At Site B and C, RHESA generated backscattering coefficients for all shapes of scatterers are closer to RADARSAT data compared to the FEKO generated results where

peanut is the closest followed by droxtal and ellipsoid. At Site I, the closest CEM generated result with the RADARSAT data is FEKO generated hexagonal column, cylinder and droxtal. However, at Site P, RHESA generated results are closer to the RADARSAT data compared to FEKO generated results where the RHESA generated peanut-shaped ice scatterer is the closest followed by the droxtal. Therefore, most of the arbitrarily shaped scatterers represent the ice scatterers. For FEKO generated backscattering coefficients, the spherical scatterer followed by hexagonal column mostly represents the ice scatterers for all the sites. For RHESA generated backscattering coefficients, spherical scatterers followed by peanut, droxtal and ellipsoid represent the ice scatterers for most of the sites.

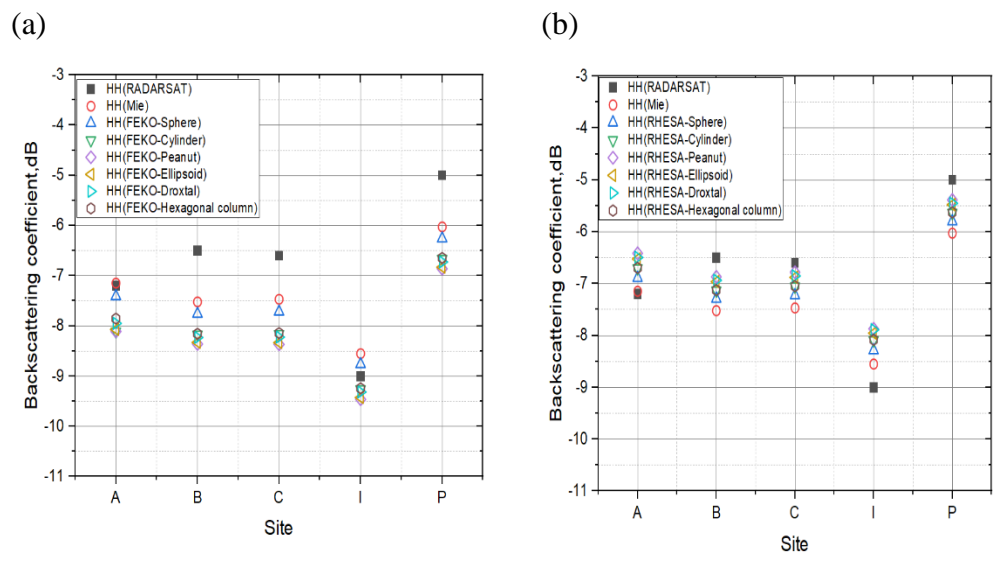


Figure 6.2 Comparison of HH backscattering coefficient of six shapes of ice scatterers produced by CEM methods (a) coupled FEM/MoM and (b) RHESA with RADARSAT data at C-Band frequency

6.4 Comparison of CEM Techniques Generated Backscattering Coefficient of Snow Medium with CLPX Data at Ku-Band Frequency

In this section, the comparison of FEKO and RHESA generated backscattering coefficients are compared with the CLPX data at Ku- Band frequency which is 15.5 GHz. The location is the same as explained in section 6.2. However, the CLPX data from three dates are used in this investigation to validate the accuracy of the CEM generated backscattering coefficients. The dates are 21/3/2003, 23/3/2003 and 24/3/2003. The list of parameters of the snow medium under investigation can be referred to in Appendix B.

Compared to the previous two sections, as the frequency increases, the differences between the FEKO created backscattering coefficient data for all shapes of scatterers and the CLPX data increases, especially for VV polarization. The HH backscattering coefficient of FEKO generated results are closer compared to the VV backscattering coefficient of FEKO generated results. However, the differences between the RHESA generated backscattering coefficient results for all shapes of scatterers and the CLPX data is lower compared to FEKO generated results. This statement can be referred from Figures 6.3, 6.4 and 6.5.

There are a few reasons for the discrepancy of the coupled FEM/MoM of FEKO generated results when compared with the CLPX data. Compared to the previous subsections where the ground truth measurement was conducted in L and C Band, the frequency in this investigation is the highest which is

15.5 GHz. As described in Chapter 5, as the frequency and the layer thickness of snow medium increases, the accuracy of the coupled FEM/MoM decreases. The theoretical study that was done in the previous chapter is important to investigate the discrepancy in the results that happens between CEM generated backscattering coefficient and ground truth measurement in this chapter. When the frequency increases, the wavelength decreases, and the value is similar with the tetrahedral edge length of the scatterers' mesh. Coupled FEM/MoM approach is based on hybridizing two conventional numerical methods. This numerical approach is based on a low-order basis function and causes an increment in the very high number of unknowns and the convergence rate of the solution will be low as well. (Notaros, 2008).

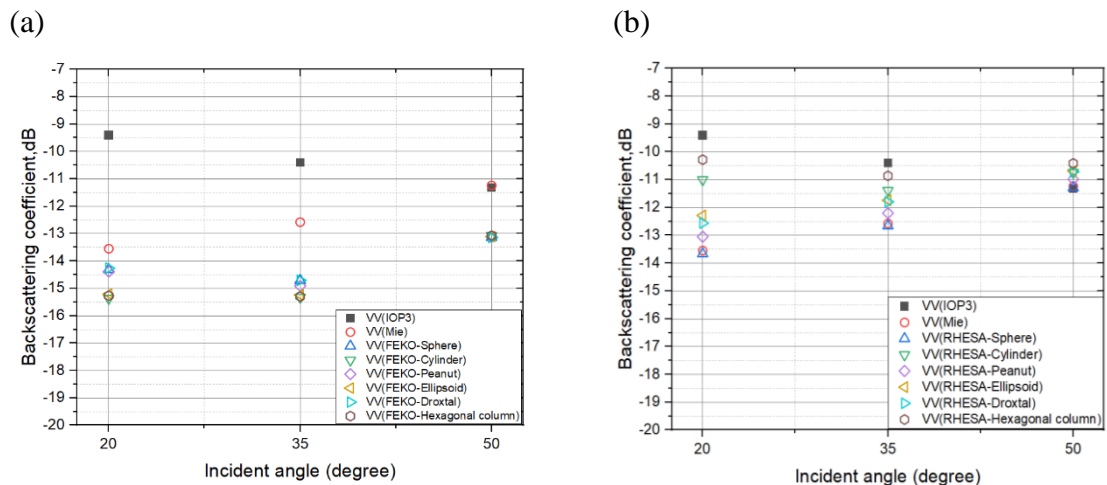
Additionally, the VV polarized backscattering coefficient is less accurate compared to the HH backscattering return as the Brewster angle effect is higher at VV polarization where it increases the effect of the multiple scattering.

Unlike coupled FEM/MoM which uses a low-order basis function, RHESA uses high order basis function where it enables sharper convergence of the solution (Notaros, 2008). As mentioned in Chapter 4, the spherical form of equivalence surface in RHESA does not cause any current singularity and increases the accuracy of the computation.

Therefore, the closest shapes of ice scatterer of CEM generated backscattering coefficient with the CLPX data are RHESA generated

hexagonal column followed by cylinder, ellipsoid, droxtal and peanut. Thus, all the shapes are the potential shapes of the ice scatterers of snow medium. The parameter of the snow medium affects the possible shapes of the ice scatterers of the snow medium. For Ku Band, the most suitable CEM technique that can be used for the computation of the backscattering coefficient is RHESA compared to the coupled FEM/MoM generated by FEKO.

Few conclusions can be drawn in Chapter 5 and 6. As the frequency and layer thickness of snow medium increases, RHESA is the most suitable method to be used in computation of backscattering coefficient. It is because as the frequency and layer thickness increases, the number of unknown increases in the coupled FEM/MoM, thus affecting the accuracy of the results. Besides, due to high accuracy of RHESA computation, this CEM techniques proved that all shapes of scatterers are suitable to be used as the ice scatterers of snow medium as shown in the comparison of the results with ground truth measurements. These shapes can be used in future researches for both forward and inverse model to retrieve the information on snow medium such as SWE, backscattering returns and other parameters.



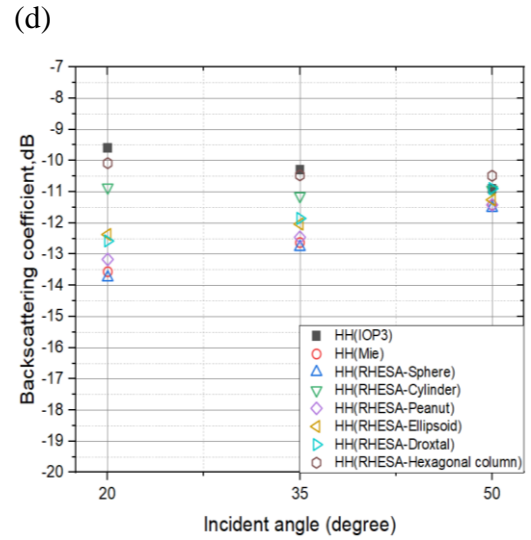
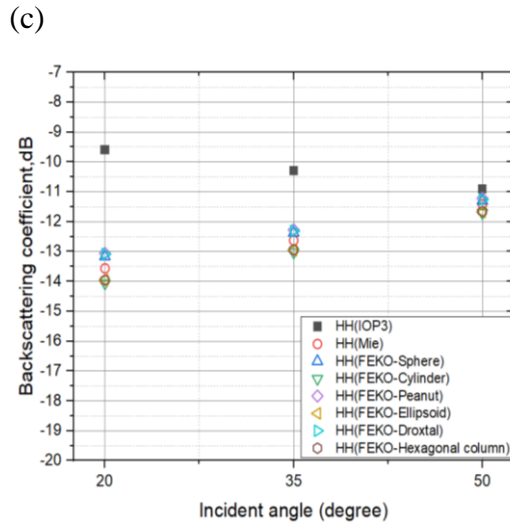
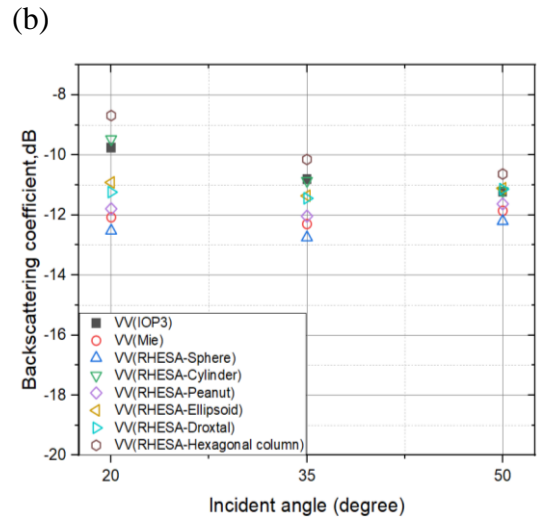
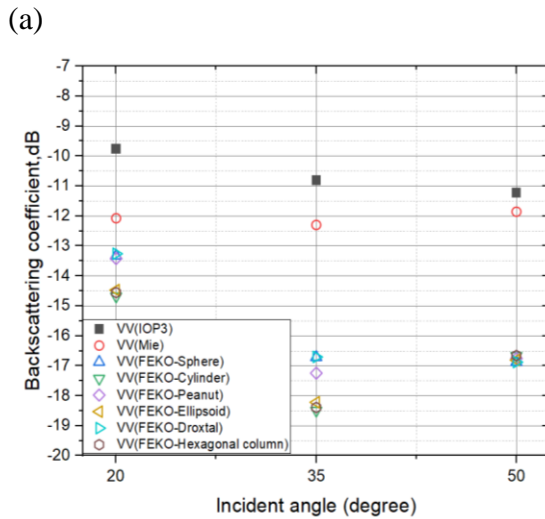


Figure 6.3 Comparison of VV backscattering coefficient of six shapes of ice scatterers produced by CEM methods (a) coupled FEM/MoM and (b) RHESA and HH backscattering coefficient (c) coupled FEM/MoM and (d) RHESA with CLPX data dated 21/2/2003 at Ku-Band frequency



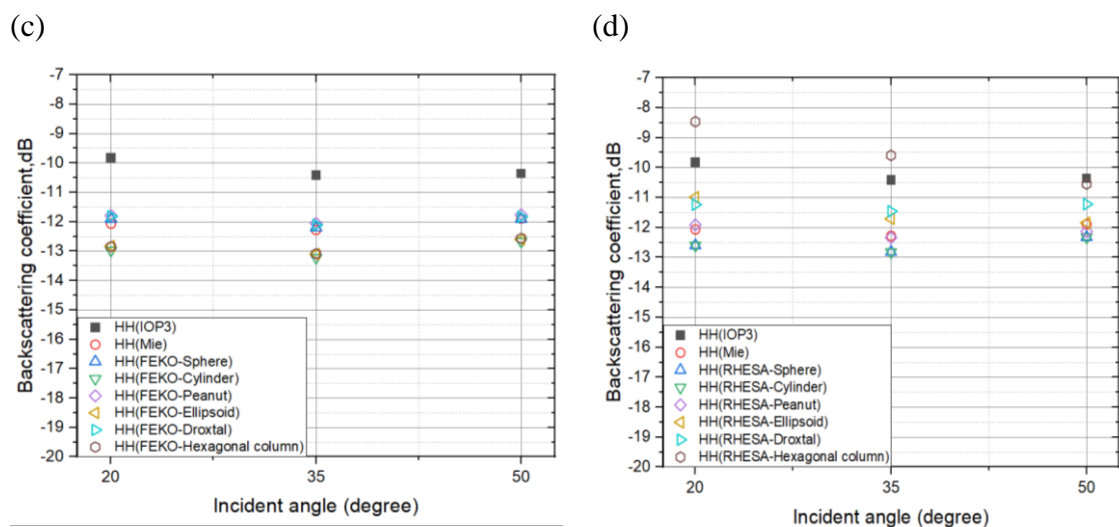
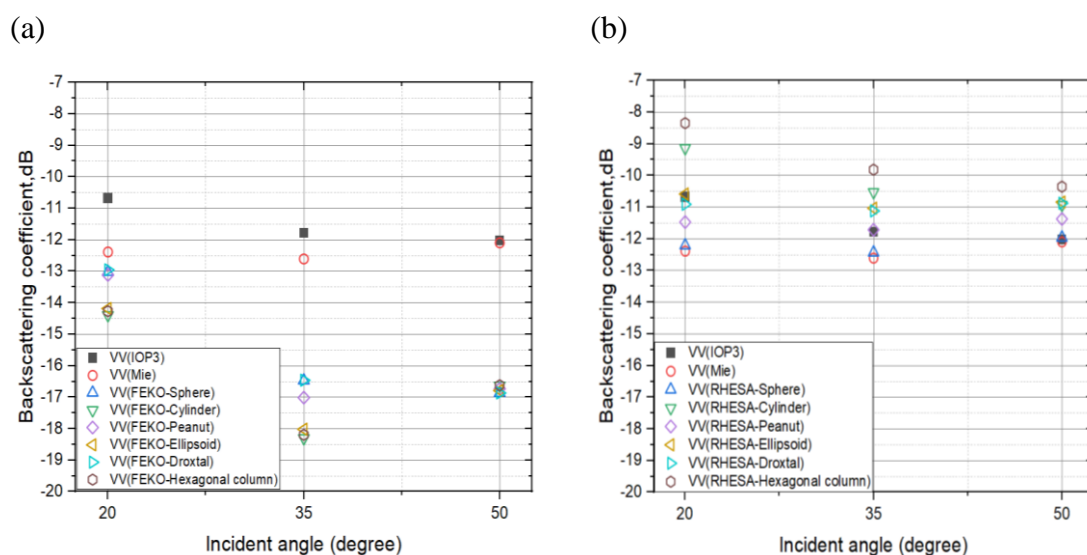


Figure 6.4 Comparison of VV backscattering coefficient of six shapes of ice scatterers produced by CEM methods (a) coupled FEM/MoM and (b) RHESA and HH backscattering coefficient (c) coupled FEM/MoM and (d) RHESA with CLPX data dated 23/2/2003 at Ku-Band frequency.



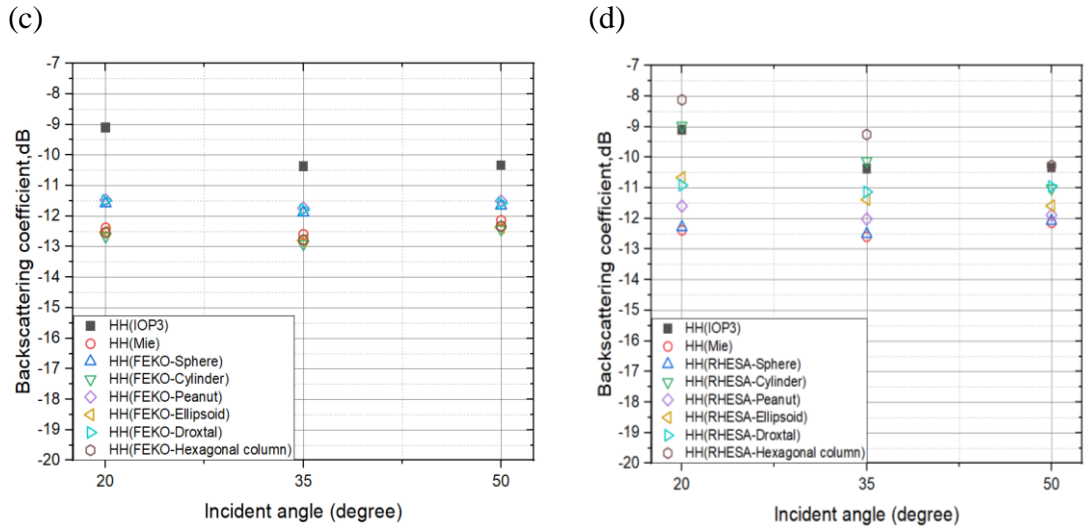


Figure 6.5 Comparison of VV backscattering coefficient of six shapes of ice scatterers produced by CEM methods (a) coupled FEM/MoM and (b) RHESA and HH backscattering coefficient (c) coupled FEM/MoM and (d) RHESA with CLPX data dated 24/2/2003 at Ku-Band frequency.

6.5 Summary

The second-order radiative transfer backscattering coefficients of snow medium produced by two CEM methods are compared with the ground truth data to examine the accuracy of the CEM techniques and to verify the possible shapes of the ice scatterers of the snow medium and ice shelf.

For L and C Bands, both CEM techniques are suitable to be used for the calculation of the backscattering coefficient of the snow medium. However, for the Ku band, RHESA is more suitable compared to the coupled FEM/MoM by FEKO software as the RHESA computation focuses more on high order basis function where the number of unknowns is being reduced, thus increasing the accuracy of the backscattering return. Furthermore, all the shapes are the potential shapes of the ice scatterers of snow medium and ice

shelf where hexagonal column, cylinder and peanut have the closest backscattering coefficient with most of the ground truth measurements.

As presented in Chapter 5, as the frequency and layer thickness of snow medium increase, the accuracy of FEKO generated backscattering coefficient decreases compared to that of RHESA. The discrepancies between FEKO generated backscattering coefficient with Mie theoretical result increase as the frequency and layer thickness of snow medium increase. These findings help to justify the discrepancies between the CEM generated results and ground truth measurements. It can be concluded that the best CEM technique that can be used for the investigation of backscattering coefficient for snow medium for all range of frequencies and layer thickness is RHESA. Coupled FEM/MoM is suitable to be used for smaller frequency and layer thickness of snow medium due to its high number of unknowns. Besides, from the analysis of the comparison between CEM generated results and ground truth measurement, all shapes of scatterers are suitable to be the ice scatterers of snow medium.

In the next chapter, the study done in this dissertation will be concluded and summarized.

CHAPTER 7

CONCLUSION

7.1 Conclusion of the Research

In this dissertation, a second-order radiative transfer equation was incorporated with two different computation methods which are the coupled FEM/MoM using FEKO software and RHESA to investigate the validation of the various shapes of scatterers' model by computing the backscattering coefficient of snow medium and the results are evaluated with Mie theoretical results and ground truth measurements.

The first and second chapter of the dissertation focus on the background of remote sensing and the application of the second-order radiative transfer equation on microwave remote sensing. As many shapes of the scatterers are being developed for various earth terrain, it is important to apply Computational Electromagnetics (CEM) in this radiative transfer equation to solve more complicated numerical computations of second-order RT equations. The problem statement and objective of the research are being highlighted in the first chapter of the dissertation. In the second chapter, the second-order RT equation for snow medium and the geometry of the non-spherical shapes of the ice scatterer and their equations are presented. The

model development of second order RT equation using two CEM techniques are also described in this chapter.

In Chapters 3 and 4 of the dissertation, the development of the RT-coupled FEM/MoM and RHESA are presented respectively. In Chapter 4, the mathematical formulations of the Finite Element Method (FEM) and Method of Moment (MoM) are presented. The comparison between the FEM and MoM is also done to study the difference between these numerical approaches. The advantages and the mathematical formulation of the coupled FEM/MoM are also discussed. The application of the coupled FEM/MoM in the RT equation is also displayed in the form of the equations and methodology to understand the concept of RT-coupled FEM/MoM better.

In Chapter 4, the formulation of the EPA is presented where the three major steps in the equivalence principle operator are focused in the form of an equation. Next, due to the high requirement of the computational memory, the EPA method is further developed in the form of RHESA where the spherical equivalence surface is introduced to prevent the current discontinuity and current singularity, thus increasing the accuracy of the results. The formulation and methodology of RT-RHESA are further demonstrated in this chapter.

In Chapter 5 of the dissertation, the theoretical analysis of the RT-coupled FEM/MoM and RT-RHESA are discussed where the backscattering coefficient of the spherical and non-spherical scatterers for various parameters are investigated to validate the accuracy of the theoretical model of the non-

spherical scatterers. In the investigation, as the layer thickness of the snow medium and incident angle increase, the differences between the FEKO generated VV backscattering coefficient of all shapes of scatterers and Mie theoretical results become higher compared to that of RHESA. It is coupled FEM/MoM is a low basis function where it has higher number of unknowns compared to RHESA, thus reduces the accuracy of the results especially at higher incident angles. It is because, as the incident angle rises, the penetration depth rises as well, thus causing the wave attenuation.

In most of the analysis, RHESA and FEKO simulated droxtal shaped scatterer of snow medium has the closest result with Mie theoretical result and FEKO generated spherical scatterer respectively because droxtal shaped scatterer has the closest resemblance with the spherical shaped scatterer. The RHESA produced backscattering coefficients for all shapes of ice scatterer produce stable results and the differences between RHESA generated results and Mie theoretical results are not too high where the differences are less than 5 dB for all set of investigations.

In chapter 6, the comparison of both CEM generated backscattering coefficients are compared with three sets of ground truth measurements with different frequency ranges. In the first set, NASA's CLPX data of L-Band frequency is used to compare the ground truth measurement with the CEM generated backscattering coefficient. All the shapes of the scatterers simulated by FEKO and RHESA overlap with the Mie analytical results. In the second set, RADARSAT data of C-Band frequency is compared with the CEM

generated backscattering return. In some sites of investigation, FEKO generated results for all shapes of scatterers agree well with the ground truth measurement whereas, at other sites, RHESA generated backscattering return of non-spherical scatterers are closer to the RADARSAT data. In the final set of the investigation, the comparison was done with the CLPX data of Ku band frequency. As the frequency is the highest compared to the previous two sets, FEKO generated results have a higher discrepancy of the results compared to RHESA generated results. It is because the increase of the number of unknowns and low-order basis function numerical approach may cause the discrepancy of the results. However, RHESA generated backscattering coefficient for non-spherical ice scatterers agree well with the CLPX data where all five non-spherical scatterers can be the potential shapes of ice scatterers of the snow medium. Therefore, it can be concluded that RHESA computation is a more suitable CEM approach to be utilised for snow medium compared to coupled FEM/MoM of FEKO software especially for higher frequency and layer thickness of snow medium.

7.2 Advantages and Limitations of the CEM Approaches

Each computational method has a different way of numerical approach and a different number of unknowns. This results in different values of backscattering coefficient for each simulation and the closest non-spherical shape with spherical scatterer and Mie theoretical results also differ as well. For example, FEKO generated results show some discrepancies of the results with Mie analytical data when the layer thickness of snow medium and

frequency increase as well. There are a few factors that caused the mentioned discrepancies. As referred in the results in Chapter 6, the differences of FEKO generated backscattering coefficients with Mie theoretical results and ground truth measurements are higher than the differences of RHESA generated backscattering coefficients with Mie theoretical results and ground truth measurements especially when frequency increases. Different CEM technique has different way of the numerical approach.

Coupled FEM/MoM in FEKO is based on the hybridization of two conventional methods which are the Finite Element Method and Method of Moment where these two methods are known as the low order basis functions. Low order basis function is a computation where the domains are on the order of $\lambda/10$ in each segment where λ is the medium's wavelength, thus the volume of the geometries is electrically too small. Hence, the computation of the field and currents are computed according to the low-order basis function. Unfortunately, it will lead to a high number of unknowns and the convergence rate of the solution will be low as well (Notaros, 2008). Furthermore, it is less flexible to compute the current of the curved and arbitrary shapes of the geometries due to the low order basis function (Ilic, Djordjevic, Ilic and Notaro, 2009). The discretization of the Finite Element is based on the edge-based function whereas the MoM is based on the triangular elements related to the tetrahedron faces. (Ali, Hubing and Dreniak, 1997). An equivalent surface current is applied at the boundaries to reduce the serious computational error where the fictitious line can be eliminated. The main motive of this hybrid technique is to prevent the termination issue due to the radiation state

application in the open area by applying an outward-looking approach. (Sumithra and Thiripurasundari, 2017). Unfortunately, the equivalent surface that encloses the scatterer is constructed in the cubical form where this non-smooth surface may overlap with each other and can cause current singularity and it can cause difficulty in the numerical computation (Fu, Jiang and Ewe, 2016). High frequency slows down the decay of the Green's function and produces unwanted side lobes. In order to reduce the high-frequency noise, the magnitude of the side lobe needs to be reduced or the side lobes need to be moved to a further distance. In this case, a smooth equivalent surface is required to reduce the noise and thus increase the accuracy (Li, 2007). Furthermore, the outward-looking approach reverses two dense matrices and compute the high number of matrix multiplication which leads to an increase in the number of unknowns (Ji, Wang and Hubing, 2000).

On the other hand, RHESA is based on the oct tree approach where spherical equivalent surface is constructed and applied to the hierarchical approach of the parent and the child group without contact with the internal primary domain. The spherical form of equivalence surface is constructed as it is smooth and does not have any discontinuity, thus increasing the accuracy of the computation (Fu, Jiang and Ma, 2015).

As demonstrated in chapter 5, the FEKO results show a higher discrepancy with Mie analytical data compared to that of the RHESA generated results because FEKO uses a non-spherical equivalent surface where it can lead to current discontinuity at the edge of the mesh structure and

charge singularity. This issue becomes significant when the higher frequency is used where the wavelength becomes similar to the edge size of the scatterers' mesh.

The advantages and limitations of each CEM technique are summarized as shown in Tables 7.1 and 7.2.

Table 7.1: Summary of the advantages and limitations of coupled FEM/MoM computation in FEKO software

Advantages	Limitations
<p>A user-friendly interface where multiple incidents and scattered plane waves can be initialized in a single computation and reduce the run time. The geometrical modelling and result generation can be done in the CADFEKO itself.</p>	<p>At the high layer thickness of snow medium and high frequency, the number of unknowns is higher than the RHESA computation due to the lower basis function approach, thus producing less accurate results. It is because the CEM approach is based on the conventional FEM method hybridised with conventional MoM. Thus, it is limited to a low range of layer thickness and low frequency.</p>
<p>Produces accurate results at a lower layer thickness of snow medium and lower frequency due to the lower number of unknowns.</p>	

Table 7.2: Summary of the advantages and limitations of RHESA computation

Advantages	Limitations
<p>The oct tree approach that is used in the RHESA computation decreases the number of unknowns and increases the computational capacity, thus generating accurate results for the high layer thickness of snow medium as it is based on the high order basis function approach.</p>	<p>The geometry needs to be constructed in ANSYS APDL where the number of mesh being used is limited and later need to be exported in the RHESA computation, thus the process takes a long time for more complicated earth terrain.</p>
<p>The computation can be used for any range of frequencies without any frequency breakdown.</p>	

7.3 Future Improvement

To increase the accuracy of the backscattering coefficient for both CEM techniques, it is encouraged to use high Gaussian Quadrature points. However, more computational time and memory are required to simulate high Gaussian points for the incident and scattered waves. Besides, in order to reduce the number of unknowns in coupled FEM/MoM, other numerical approaches such as Multilevel Fast Multipole Method (MLFMM) can be hybridized in the

coupled FEM/MoM to reduce the number of unknowns and increase the accuracy of the results. However, it requires high computational processors and computational time. Furthermore, it is encouraged to study more complicated shapes such as aggregated shapes and non-symmetrical shapes of ice scatterers using these CEM methods to understand the metamorphism process of ice scatterers of snow medium. However, this requires more development in the RT equation and more computational memory to investigate this process.

REFERENCES

- Albert, M., Lee, Y., Ewe, H. and Chuah, H., 2012. Multilayer Model Formulation and Analysis of Radar Backscattering from Sea Ice. *Progress in Electromagnetics Research*, 128, pp.267-290.
- Ali, M., Hubing, T. and Dreniak, J., 1997. A hybrid FEM/MOM technique for electromagnetic scattering and radiation from dielectric objects with attached wires. *IEEE Transactions on Electromagnetic Compatibility*, 39(4), pp.304-314.
- Altair Engineering Inc, 2015. *Numerical Methods in FEKO*. USA: Altair Engineering, Inc, p.1.
- Augustyniak, M. and Usarek, Z., 2016. Finite Element Method Applied in Electromagnetic NDTE: A Review. *Journal of Nondestructive Evaluation*, 35(3).
- Baltzis, K., 2009. The finite element method magnetics (FEMM) freeware package: May it serve as an educational tool in teaching electromagnetics?. *Education and Information Technologies*, 15(1), pp.19-36.
- Bhobe, A., Holloway, C. and Picket-May, M., 2001. Meander delay line challenge problem: a comparison using FDTD, FEM and MoM. *2001 IEEE EMC International Symposium. Symposium Record. International Symposium on Electromagnetic Compatibility (Cat. No.01CH37161)*.

- Chan Fai, L., 2018. *A Study of Microwave Remote Sensing of Natural Medium using Radiative Transfer Theory and Relaxed Hierarchical Equivalent Source Algorithm*. Master of Engineering Science. Lee Kong Chian Faculty of Engineering and Science, Universiti Tunku Abdul Rahman.
- Chandrasekhar, S., 1989. *Radiative transfer and negative ion of hydrogen*. Chicago: The University of Chicago.
- Chew, W., Jin, J., Lu, C., Michielssen, E. and Song, J., 1997. Fast solution methods in electromagnetics. *IEEE Transactions on Antennas and Propagation*, 45(3), pp.533-543.
- Chuah, H., Tjuatja, S., Fung, A. and Bredow, J., 1996. A phase matrix for a dense discrete random medium: evaluation of volume scattering coefficient. *IEEE Transactions on Geoscience and Remote Sensing*, 34(5), pp.1137-1143.
- Davidson, D., 2011. *Computational electromagnetics for RF and microwave engineering*. Cambridge: Cambridge University Press.
- Draine, B. and Flatau, P., 1994. Discrete-Dipole Approximation for Scattering Calculations. *Journal of the Optical Society of America A*, 11(4), p.1491.
- Du, J., Shi, J. and Rott, H., 2010. Comparison between a multi-scattering and multi-layer snow scattering model and its parameterized snow backscattering model. *Remote Sensing of Environment*, 114(5), pp.1089-1098.
- Durand, M., Molotch, N. and Margulis, S., 2008. A Bayesian approach to snow water equivalent reconstruction. *Journal of Geophysical Research*, 113(D20).
- Ewe, H. and Chuah, H., 1998. An analysis of the scattering of discrete scatterers in an electrically dense medium. *IGARSS '98. Sensing and*

Managing the Environment. 1998 IEEE International Geoscience and Remote Sensing. Symposium Proceedings. (Cat. No.98CH36174)

Ewe, H. and Chuah, H., 2000. Electromagnetic scattering from an electrically dense vegetation medium. *IEEE Transactions on Geoscience and Remote Sensing*, 38(5), pp.2093-2105.

Ewe, H., Chuah, H. and Fung, A., 1998. A Backscatter Model for a Dense Discrete Medium. *Remote Sensing of Environment*, 65(2), pp.195-203.

Fu, X., Jiang, L. and Ewe, H., 2016. A novel relaxed hierarchical equivalent source algorithm (RHESA) for electromagnetic scattering analysis of dielectric objects. *Journal of Electromagnetic Waves and Applications*, 30(12), pp.1631-1642.

Fu, X., Jiang, L. and Ma, Z., 2015. Accuracy enhancement of the equivalence principle algorithm based on the meshless spherical surface. *2015 IEEE International Conference on Computational Electromagnetics*.

Fung, A. and Eom, H., 1985. A Study of Backscattering and Emission from Closely Packed Inhomogeneous Media. *IEEE Transactions on Geoscience and Remote Sensing*, GE-23(5), pp.761-767.

Fung, A., Tsuatja, S., Bredow, J. and Chuah, H., 1995. Dense medium phase and amplitude correction theory for spatially and electrically dense media. *1995 International Geoscience and Remote Sensing Symposium, IGARSS '95. Quantitative Remote Sensing for Science and Applications*.

Fung, A., 1994. *Microwave scattering and emission models and their applications*. Boston: Artech House.

George, A., 1976. Sparse Matrix Aspects of the Finite Element Method. *Lecture Notes in Economics and Mathematical Systems*, pp.3-22.

- Gibson, W., 2015. *Method of Moments in Electromagnetics*. 2nd ed. Boca Raton: CRC PRESS.
- Grenfell, T. and Warren, S., 1999. Representation of a nonspherical ice particle by a collection of independent spheres for scattering and absorption of radiation. *Journal of Geophysical Research: Atmospheres*, 104(D24), pp.31697-31709.
- Hara, M., Yoshikane, T., Kawase, H. and Kimura, F., 2008. Estimation of the Impact of Global Warming on Snow Depth in Japan by the Pseudo-Global-Warming Method. *Hydrological Research Letters*, 2, pp.61-64.
- Hara, M., Yoshikane, T., Kawase, H. and Kimura, F., 2008. Estimation of the Impact of Global Warming on Snow Depth in Japan by the Pseudo-Global-Warming Method. *Hydrological Research Letters*, 2, pp.61-64.
- Harrington, R., 1987. The Method of Moments in Electromagnetics. *Journal of Electromagnetic Waves and Applications*, 1(3), pp.181-200.
- Harrington, R., 2000. *Field Computation by Moment Methods*. New York: Wiley-IEEE Press.
- Hong, G., 2007. Parameterization of scattering and absorption properties of nonspherical ice crystals at microwave frequencies. *Journal of Geophysical Research*, 112(D11).
- Hulst, H., 1981. *Light Scattering by Small Particles*. Dover Publications.
- Ilic, M., Djordjevic, M., Ilic, A. and Notaro, B., 2009. Higher Order Hybrid FEM-MoM Technique for Analysis of Antennas and Scatterers. *IEEE Transactions on Antennas and Propagation*, 57(5), pp.1452-1460.
- Ishimaru, A., 1978. *Wave propagation and scattering in random media*. Academic Press, NY.

- Jakobus, U., Bingle, M., Schoeman, M., Van Tonder, J. and Illenseer, F., 2008. Tailoring FEKO for microwave problems. *IEEE Microwave Magazine*, 9(6), pp.76-85.
- Jakobus, U., Bingle, M., van Tonder, J. and Marais, J., 2008. Recent extensions in FEKO suite 5.4. *2008 8th International Symposium on Antennas, Propagation and EM Theory*,.
- Ji, Y., Wang, H. and Hubing, T., 2000. A Novel Preconditioning Technique and Comparison of Three Formulations for Hybrid FEM/MoM Methods. *Semantic Scholar*.
- K.Fung, A., 1994. *Microwave Scattering and Emission Models and Their Applications*. 1st ed. Norwood, MA: Artech House, Inc, pp.382-394.
- Li, M. and Chew, W., 2007. Wave-Field Interaction with Complex Structures Using Equivalence Principle Algorithm. *IEEE Transactions on Antennas and Propagation*, 55(1), pp.130-138.
- Li, M., 2007. *Studies on Applying The Equivalence Principle Algorithm on Multiscale Problems*. Doctor of Philosophy in Electrical and Computer Engineering. University of Illinois at Urbana-Champaign.
- Li, M., Zhuang, T. and Chen, R., 2018. Volume Integral Equation Equivalence Principle Algorithm Domain Decomposition with Body of Revolution Equivalence Surface. *IET Microwaves, Antennas & Propagation*, 12(3), pp.375-379.
- Liao, L. and Sassen, K., 1994. Investigation of relationships between Ka-band radar reflectivity and ice and liquid water contents. *Atmospheric Research*, 34(1-4), pp.231-248.

- Liu, N. and Li, Z., 2002. Bi-spectrum scattering model for conducting randomly rough surface. *Tsinghua Science and Technology*, 7(3), pp.309-316.
- Liu, N., Li, Z. and Weng, H., 1999. A spectrum domain Kirchhoff scattering model for randomly rough surface. *1999 International Conference on Computational Electromagnetics and its Applications. Proceedings (ICCEA'99) (IEEE Cat. No.99EX374)*.
- Liu, Z., Ping, L., Sun, B., Sun, G. and He, X., 2010. Scattering of 3-D objects with a new total-and scattered-field decomposition technique for FEM. *2010 Asia-Pacific International Symposium on Electromagnetic Compatibility*.
- Lum, C., Fu, X., Ewe, H. and Jiang, L., 2017. A Study of Scattering from Snow Embedded with Non-Spherical Shapes of Scatterers with Relaxed Hierarchical Equivalent Source Algorithm (RHESA). *Progress in Electromagnetics Research M*, 61, pp.51-60.
- Magono, C., 1962. Meteorological Classification of Snow Crystals. *Journal of the Japanese Society of Snow and Ice*, 24(2), pp.33-37.
- Marshall, H., Koh, G. and Forster, R., 2004. Ground-based frequency-modulated continuous wave radar measurements in wet and dry snowpacks, Colorado, USA: an analysis and summary of the 2002-03 NASA CLPX data. *Hydrological Processes*, 18(18), pp.3609-3622.
- Marzano, F., 2014. Radiative Transfer, Theory. *Encyclopedia of Remote Sensing*, pp.624-634.
- Massom, R., Eicken, H., Hass, C., Jeffries, M., Drinkwater, M., Sturm, M., Worby, A., Wu, X., Lytle, V., Ushio, S., Morris, K., Reid, P., Warren, S. and Allison, I., 2001. Snow on Antarctic Sea ice. *Reviews of Geophysics*, 39(3), pp.413-445.

- Mätzler, C., 2006. *Thermal Microwave Radiation*. London: Institution of Electrical Engineers.
- Mishchenko, M., Travis, L. and Macke, A., 1996. Scattering of light by polydisperse, randomly oriented, finite circular cylinders. *Applied Optics*, 35(24), p.4927.
- Ney, M., 1985. Method of Moments as Applied to Electromagnetic Problems. *IEEE Transactions on Microwave Theory and Techniques*, 33(10), pp.972-980.
- Niittynen, P. and Luoto, M., 2017. The importance of snow in species distribution models of arctic vegetation. *Ecography*, 41(6), pp.1024-1037.
- Notaros, B., 2008. Higher Order Frequency-Domain Computational Electromagnetics. *IEEE Transactions on Antennas and Propagation*, 56(8), pp.2251-2276.
- Piazza, R. and Degiorgio, V., 2005. Scattering, Rayleigh. *Encyclopedia of Condensed Matter Physics*, pp.234-242.
- Pinzer, B. and Schneebeli, M., 2009. Snow metamorphism under alternating temperature gradients: Morphology and recrystallization in surface snow. *Geophysical Research Letters*, 36(23).
- Platt, U., Pfeilsticker, K. and Vollmer, M., 2007. Radiation and Optics in the Atmosphere. *Springer Handbook of Lasers and Optics*, pp.1165-1203.
- Polycarpou, A., 2006. Introduction to the Finite Element Method in Electromagnetics. *Synthesis Lectures on Computational Electromagnetics*, 1(1), pp.1-126.
- Rylander, T., Ingelström, P. and Bondeson, A., 2013. *Computational Electromagnetics*. New York, NY: Springer.

Sarabandi, K., 2003. *CLPX-Ground: Ground-based L and Ku band polarimetric scatterometry, Version 1.* Boulder, Colorado, USA: NASA National Snow and Ice Data Center Distributed Active Archive Center.

Schuster, A., 1905. Radiation Through a Foggy Atmosphere. *The Astrophysical Journal*, 21, p.1.

Shin, R. and Kong, J., 1981. *Radiative transfer theory for active remote sensing of a homogenous layer containing spherical scatterers.*

Silvester, P. and Ferrari, R., 1996. *Finite elements for electrical engineers.* New York: Cambridge University Press.

Song, J., Lu, C. and Chew, W., 1997. Multilevel fast multipole algorithm for electromagnetic scattering by large complex objects. *IEEE Transactions on Antennas and Propagation*, 45(10), pp.1488-1493.

Stratton, J. and Chu, L., 1939. Diffraction Theory of Electromagnetic Waves. *Physical Review*, 56(1), pp.99-107.

Sumithra, P. and Thiripurasundari, D., 2017. Review on Computational Electromagnetics. *Advanced Electromagnetics*, 6(1), p.42.

Syahali, S., Hong Tat, E., Vetharatnam, G., Jiang, L. and A Kumaresan, H., 2020. Backscattering Analysis of Cylinder Shaped Scatterer in Vegetation Medium: Comparison Between Theories. *Journal of Engineering Technology and Applied Physics*, 2(1), pp.15-18.

Tai, H., 2005. *Introduction to Finite Element Method.* South Korea: Department of Mechanical Engineering, Pohang University of Science and Technology, pp.5,6.

Tang, C. and Aydin, K., 1995. Scattering from ice crystals at 94 and 220 GHz millimeter wave frequencies. *IEEE Transactions on Geoscience and Remote Sensing*, 33(1), pp.93-99.

Tanikawa, T., Aoki, T., Hori, M., Hachikubo, A., Abe, O. and Aniya, M., 2006. Monte Carlo simulations of spectral albedo for artificial snowpacks composed of spherical and nonspherical particles. *Applied Optics*, 45(21), p.5310.

Tiryaki, B., 2010. *Solution of Electromagnetics Problems with the Equivalence Principle Algorithm*. Master of Science. The Institute of Engineering and Science of Bilkent University.

Tsang, L. and Ishimaru, A., 1987. Radiative Wave Equations for Vector Electromagnetic Propagation in Dense Nontenuous Media. *Journal of Electromagnetic Waves and Applications*, 1(1), pp.59-72.

Tsang, L., Ding, K., Huang, S. and Xu, X., 2013. Electromagnetic Computation in Scattering of Electromagnetic Waves by Random Rough Surface and Dense Media in Microwave Remote Sensing of Land Surfaces. *Proceedings of the IEEE*, 101(2), pp.255-279.

Tsang, L., Pan, J., Liang, D., Li, Z. and Cline, D., 2006. Modeling Active Microwave Remote Sensing of Snow using Dense Media Radiative Transfer (DMRT) Theory with Multiple Scattering Effects. *2006 IEEE International Symposium on Geoscience and Remote Sensing*.

Tsang, L., Pan, J., Liang, D., Li, Z., Cline, D. and Tan, Y., 2007. Modeling Active Microwave Remote Sensing of Snow Using Dense Media Radiative Transfer (DMRT) Theory with Multiple-Scattering Effects. *IEEE Transactions on Geoscience and Remote Sensing*, 45(4), pp.990-1004.

- Van Atta, L. and Silver, S., 1962. Contributions to the Antenna Field during World War II. *Proceedings of the IRE*, 50(5), pp.692-697.
- Wen, B., Tsang, L., Winebrenner, D. and Ishimaru, A., 1990. Dense medium radiative transfer theory: comparison with experiment and application to microwave remote sensing and polarimetry. *IEEE Transactions on Geoscience and Remote Sensing*, 28(1), pp.46-59.
- West, R., Gibbs, D., Tsang, L. and Fung, A., 1994. Comparison of optical scattering experiments and the quasi-crystalline approximation for dense media. *Journal of the Optical Society of America A*, 11(6), p.1854.
- Woodhouse, I., 2017. *Introduction to Microwave Remote Sensing*. Boca Raton: Chapman and Hall/CRC.
- Xia, T., Meng, L., Liu, Q., Gan, H. and Chew, W., 2018. A Low-Frequency Stable Broadband Multilevel Fast Multipole Algorithm Using Plane Wave Multipole Hybridization. *IEEE Transactions on Antennas and Propagation*, 66(11), pp.6137-6145.
- Xie, Y., Yang, P., Gao, B., Kattawar, G. and Mishchenko, M., 2006. Effect of ice crystal shape and effective size on snow bidirectional reflectance. *Journal of Quantitative Spectroscopy and Radiative Transfer*, 100(1-3), pp.457-469.
- Xu, X., Brekke, C., Doulgeris, A. and Melandsø, F., 2018. Numerical Analysis of Microwave Scattering from Layered Sea Ice Based on the Finite Element Method. *Remote Sensing*, 10(9), p.1332.
- Xu, Y., 1995. Electromagnetic scattering by an aggregate of spheres. *Applied Optics*, 34(21), p.4573.

Yang, P., Baum, B., Heymsfield, A., Hu, Y., Huang, H., Tsay, S. and Ackerman, S., 2003. Single-scattering properties of droxtals. *Journal of Quantitative Spectroscopy and Radiative Transfer*, 79-80, pp.1159-1169.

Zhu, J., Tan, S., King, J., Derksen, C., Lemmetyinen, J. and Tsang, L., 2018. Forward and Inverse Radar Modeling of Terrestrial Snow Using SnowSAR Data. *IEEE Transactions on Geoscience and Remote Sensing*, 56(12), pp.7122-7132.

APPENDIX A

The complete 4×4 phase matrix, \bar{P} is

$$P = 4\pi \langle M \rangle / (A \cos \theta_s)$$

θ_s is the angle between the scattered path and the path normal to the radiated area A and Stokes matrix, M is derived as (Fung and Chen, 1994)

$$\begin{bmatrix} |S_{vv}|^2 & |S_{vh}|^2 & \text{Re}(S_{vv}S_{vh}^*) & -\text{Im}(S_{vv}S_{vh}^*) \\ |S_{hv}|^2 & |S_{hh}|^2 & \text{Re}(S_{hv}S_{hh}^*) & -\text{Im}(S_{hv}S_{hh}^*) \\ 2\text{Re}(S_{vv}S_{hv}^*) & 2\text{Re}(S_{vh}S_{hh}^*) & \text{Re}(S_{vv}S_{hh}^* + S_{vh}S_{hv}^*) & -\text{Im}(S_{vv}S_{hh}^* - S_{vh}S_{hv}^*) \\ 2\text{Im}(S_{vv}S_{hv}^*) & 2\text{Im}(S_{vh}S_{hh}^*) & \text{Im}(S_{vv}S_{hh}^* + S_{vh}S_{hv}^*) & \text{Re}(S_{vv}S_{hh}^* - S_{vh}S_{hv}^*) \end{bmatrix}$$

APPENDIX B

List of parameters for Section 8.2:

Parameters	Values
Layer thickness of snow medium (m)	0.62
Scatterer's volume fraction (%)	23
Scatterers' relative permittivity	(3.15, 0.001)
Top layer's relative permittivity	(1.0, 0.0)
Background's relative permittivity	(1.0, 0.0)
Bottom layer's relative permittivity	(6.0, 0.0)
Correlation length, RMS height of top surface (cm)	6.0, 0.8
Correlation length, RMS height of bottom surface (cm)	6.0, 0.68

List of parameters for Section 8.3:

Parameters	Site				
	A	B	C	I	P
Layer thickness of snow medium (m)	250	250	250	250	250
Scatterer's volume fraction (%)	32	32	32	32	32
Scatterer's relative permittivity	(1.58, 7.39E-05)	(1.50, 6.72E-05)	(1.53, 7.14E-05)	(1.42, 4.76E-05)	(1.57, 4.74E-05)

					05)
Top layer's relative permittivity	(1.0, 0.0)	(1.0, 0.0)	(1.0, 0.0)	(1.0, 0.0)	(1.0, 0.0)
Background's relative permittivity	(1.0, 0.0)	(1.0, 0.0)	(1.0, 0.0)	(1.0, 0.0)	(1.0, 0.0)
Bottom layer's relative permittivity	(59.0, 42.0)	(59.0, 42.0)	(59.0, 42.0)	(59.0, 42.0)	(59.0, 42.0)
Correlation length, RMS height of top surface (cm)	2.1, 0.39	3.17, 0.51	4.88, 0.13	34.00, 0.14	14.77, 0.30
Correlation length, RMS height of top surface (cm)	4.70, 0.58	4.70, 0.58	4.70, 0.58	4.70, 0.42	4.70, 0.58

List of parameters for Section 8.4:

Parameters	Dates		
	21/2/2003	23/2/2003	24/2/2003
Layer thickness of snow medium (m)	0.62	0.99	1.08
Scatterer's volume fraction (%)	23	23	23
Scatterer's relative permittivity	(3.15, 0.001)	(3.15, 0.001)	(3.15, 0.001)
Top layer's relative permittivity	(1.0, 0.0)	(1.0, 0.0)	(1.0, 0.0)
Background's relative permittivity	(1.0, 0.0)	(1.0, 0.0)	(1.0, 0.0)

Bottom layer's relative permittivity	(6.0, 0.0)	(6.0, 0.0)	(6.0, 0.0)
Correlation length, top surface RMS (cm)	6.0, 0.8	10.0, 0.6	10.0, 0.6
Correlation length, bottom surface RMS (cm)	6.0, 0.68	10.0, 0.75	10.0, 0.75

PUBLICATION

Kumaresan, H., Ewe, H., Vetharatnam, G. and Jiang, L., 2021. Model Computation with Second-Order Radiative Transfer Equation for Snow Medium Using Coupled Finite Element Method and Method of Moment and Relaxed Hierarchical Equivalent Source Algorithm. *2021 IEEE International Geoscience and Remote Sensing Symposium IGARSS*.